Optoelectronic Properties of Two-Dimensional Molybdenum Ditelluride

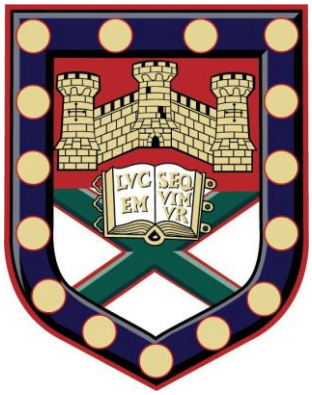

Tobias Jake Octon

College of Engineering, Mathematics and Physical Sciences

University of Exeter

A thesis submitted for the degree of Doctor of Philosophy in Engineering (CDT)

September 2018

Optoelectronic Properties of Two-Dimensional Molybdenum Ditelluride

Submitted by Tobias Jake Octon to the University of Exeter as a thesis for the degree of Doctor of Philosophy in Engineering, September 2018.

I certify that all material in this thesis which is not my own work has been identified and that no material has previously submitted and approved for the award of a degree by this or any other university.

Tobias Jake Octon

September 2018

Abstract

In this thesis the layered, two-dimensional material $MoTe_2$ is examined experimentally for its optoelectronic properties, using a field effect transistor device configuration. $MoTe_2$ experiences a strong light matter interaction, which is highly dependent on the conditions of the measurement, and the wavelength of light used. Light is able to: produce a photocurrent in $MoTe_2$, desorb adsorbates from the surface, and even controllably thin by a single layer at a time. A theoretical study on $MoTe_2$ also provides insights on the source of some of these interesting light matter interactions.

$MoTe_2$ is found to be a fast and responsive photodetector when illuminated with red laser light in ambient conditions, with increases in current stemming from the photovoltaic effect. Due to the generated charge carriers from the photovoltaic effect, conductivity can increase by increasing the Fermi energy of the material, or by a photogating effect where excited charges are trapped and behave as an artificial gate for the field effect transistor.

The mechanisms of charge trapping are experimentally investigated due to their prevalence in the photodetection mechanisms. A theoretical study points towards the existence of two types of trap states, in not just $MoTe_2$ but all transition metal dichalcogenides, with shallow traps closer to the valence band edge ($\tau \sim 500$ s) and deeper traps ($\tau \sim 1000$ s), further away from the valence band edge.

$MoTe_2$, under the effects of higher energy photons from blue and green lasers, showed different photocurrent mechanisms to red light. From the increased energy of the photons, photo-desorption of adsorbates on the surface of $MoTe_2$ occurred causing a decrease in the overall current, in a rarely seen photocurrent mechanism. Again, both shallow and deep traps are evident from the experimental measurements, with the shallow traps being removed when illuminated by higher energy photons.

Finally, a humidity assisted photochemical layer-by-layer etching process was developed with an in-situ Raman spectroscopy system, able to thin $MoTe_2$ by a single layer at a time with 200 nm spatial resolution. $MoTe_2$ FETs were created with thinned channels to examine the effect of the thinning technique on optoelectronic properties. Some improvement in optoelectronic performance (higher responsivity, higher mobility) was

seen for the thinned channel devices, with great improvement observed for monolayer $MoTe_2$.

Acknowledgements

I would like to thank my supervisors, Prof. David Wright and Prof. Monica Craciun, for without their advice and knowledge this PhD would not have been possible. Both of my supervisors have provided encouragement and support throughout my studies and have shown me the ropes of academia. They provided a very pleasant working environment, where everyone is encouraged to learn and contribute to projects in a collaborative manner.

I am very appreciative to the EPSRC and numerous companies which provided the funding for the Centre for Doctoral Training (CDT) in Metamaterials, and for the CDT in their efforts to provide a breadth of training to assist me going forward in my future career. I'd also like to express thanks to everyone in the CDT, especially those managing the day to day workings for their kindness and hard work.

From the Wright and Russo-Craciun research groups, I would like to thank all of you for your advice and expertise. Especially, I'd like to thank Karthik, Iddo, Jake, Adolfo, Gareth, Nicola, Matt, Mohsin and Arseny for teaching me everything from fabrication and measurement techniques to ideas for how to best study the properties of $MoTe_2$. I would like to show particular gratitude to Dr. Karthik Nagareddy, who taught me how to characterize $MoTe_2$, and who contributed greatly to the work on the layer-by-layer laser thinning technique. I am also especially grateful to Dr. Iddo Amit, who developed the theory for current transients in $MoTe_2$, upon which a great deal of the results in this thesis were made explainable through his efforts.

I would like to thank Dr. Alex Dickinson for showing me his research on hip joints, and working with Dr. Dario Carugo both at Southampton University on microfluidics, which gave me the passion to pursue a PhD in the first place.

Finally I would like to thank my friends and family for their support. Thanks to many who have had to suffer with me as their housemate, Ben Ash, Tom Graham, Ben Hogan, Chris Mowat, Robin Smith, Matt Parish, and Sam Shelley, thank you for all good times during my last eight years, I really appreciate it. To Alex Ausden, Barney Dobson, Joe Janaway, Sam Taylor and all my KES mates, I'm grateful for all the fond memories over the years. I would like to thank my family, especially my parents for their love and support

throughout my life. Special thanks go to my fiancée Lydia Burke, who has constantly reassured that everything will be alright in the end. My apologies and thanks to those not mentioned who should be, this was surprisingly difficult to write.

Contents

List of Publications and Presentations

1. **Tobias J. Octon**, V. Karthik Nagareddy, Saverio Russo, Monica F. Craciun and C. David Wright, "Fast High-Responsivity Few-Layer $MoTe_2$ Photodetectors", *Advanced Optical Materials,* vol. 4 p 1750-1754, (2016)

2. Iddo Amit, **Tobias J. Octon**, Nicola J. Townsend, Francesco Reale, C. David Wright, Cecilia Mattevi, Monica F. Craciun and Saverio Russo, "Role of Charge Traps in the Performance of Atomically Thin Transistors", *Advanced Materials*, vol. 29, 16055598, (2017)

3. V. Karthik Nagareddy, **Tobias J. Octon**, Nicola J. Townsend, Saverio Russo, Monica F. Craciun and C. David Wright, "Humidity-Controlled Ultra-Low Power Layer-by-Layer Photochemical Thinning, Nanopatterning and Band-Gap Engineering of $MoTe_2$" *Advanced Functional Materials*, In press. (2018)

4. **Tobias J. Octon**, Iddo Amit, V. Karthik Nagareddy, Gareth Jones, Saverio Russo, Monica F. Craciun and C. David Wright, "Photo-Desorption of Adsorbates on $MoTe_2$ using High Energy, Visible Light in Ambient Conditions" *Appl. Phys. Lett.* (in preparation).

5. **Tobias J. Octon**, V. Karthik Nagareddy, Monica F. Craciun and C. David Wright, "Two Dimensional $MoTe_2$ Optoelectronic Devices", *7th Windsor Summer School in Nanoscience and 2D Nanomaterials*, Winsor, United Kingdom, 27th July – 1st August 2015.

6. **Tobias J. Octon**, V. Karthik Nagareddy, Monica F. Craciun and C. David Wright, "Photoconductivity of $MoTe_2$", *META '16*, Malaga, Spain, 25th - 28th July 2016.

7. **Tobias J. Octon**, V. Karthik Nagareddy, Iddo Amit, Saverio Russo, Monica F. Craciun and C. David Wright, "Optoelectronic Properties of Pristine and Deterministically Thinned 2H-$MoTe_2$", *MRS Spring 2017*, Phoenix, Arizona, April 17th - 21st 2017.

8. **Tobias J. Octon**, V. Karthik Nagareddy, Saverio Russo, Monica, F. Craciun and C. David Wright, "Photoconductivity of $MoTe_2$", *Photonics and Optoelectronic Materials*, Exeter, United Kingdom, April 9th - 10th 2018.

List of Figures

List of Tables

Abbreviations

Notation	Definition
2D	Two Dimensional
ITO	Indium Tin Oxide
TMDC	Transition Metal Dichalcogenide
h-BN	Hexagonal Boron Nitride
BP	Black Phosphorus
FET	Field Effect Transistor
CVD	Chemical Vapour Deposition
PVD	Physical Vapour Deposition
MBE	Molecular Beam Epitaxy
PL	Photoluminescence
q	Elementary Charge
φ_m	Metal Work Function
φ_n	Semiconductor Work Function
χ	Electron Affinity
E_v	Valence Band Energy
E_c	Conductance band Energy
E_f	Fermi Energy
W_B	Schottky Barrier Width
ψ_{bi}	Built in Potential Field
NIR	Near Infra-Red
FLP	Fermi Level Pinning
SPCM	Scanning Photocurrent Microscopy
AFM	Atomic Force Microscopy
PDMS	Polydimethylsiloxane
IPA	Isopropyl Alcohol
PMMA	Polymethyl Methacrylate
MIBK	Methyl Isobutyl Ketone
MEK	Methyl Ethyl Ketone

RTP	Rapid Thermal Processing
LWD	Long Working Distance
NA	Numerical Aperture
CCD	Charge Coupled Device
PCB	Printed Circuit Board
μ_{FE}	Field Effect Mobility
I_{ds}	Source-Drain Current
V_{ds}	Source-Drain Bias Voltage
C_{ox}	Oxide Capacitance
W	Device Width
V_g	Gate Voltage
Dec	Decade
EQE	External Quantum Efficiency
V_T	Threshold Voltage
PTE	Photothermoelectric
PV	Photovoltaic
UV	Ultra Violet
φ_{MS}	Difference in Work Function Between Metal and Semiconductor
Q_i	Static Charge Density
Q_T	Trapped Charge Density
I_T	Transient Current
τ_1	Decay Constant of Shallow Traps
T_2	Decay Constant of Deep Traps
E_{T1}	Shallow Trap State Energy
E_{T2}	Deep Trap State Energy
R_{pc}	Hole Capture Rate from Valence Band
N_T	Total Density of Trapped States
p_T	Density of Holes in Occupied States
c_p	Capture Coefficient for Holes
R_{pe}	Hole Emission Rate from Trap States
e_p	Emission Coefficient for Holes
R_p	Total Rate Change of Trap States

A	Device Area
$\mathbf{V_{t,sat}}$	Time Independent Threshold Voltage
$\mathbf{I_{ds,sat}}$	Time Independent Source-Drain Current

1. Introduction

Over the past twenty years, electronics have provided us with devices which provide portable connectivity to the world around us without rest. As the demand for consumer electronics increases evermore, new materials will be required to keep up with demand for growing areas in technology, such as wearable and transparent electronics, and optoelectronics. While Silicon based semiconductors provide many uses in electronics, they lack the material properties to fulfil all of these new demands. Two-dimensional materials show promise in being able to bridge the gap for these growing industries, as they show good electrical properties, are highly flexible[1,2] and transparent[3] (while still showing strong light-matter interaction).[4–7]

Two-dimensional materials have become a highly researched field because of their useful properties, with the most famous of these being graphene, a single atomic layer of graphite, the discovery of which won the Nobel Prize for Physics in 2010.[8] It is possible to extract a single layer of graphite, as layers of graphite are separated by weak van de Waals forces. Graphene was first created by using Scotch tape to peel layers away from a bulk crystal of graphite and was found to have amazing material properties: showing high conductivity,[8] great strength[9] and transparency.[10] These properties make graphene suitable for uses in numerous applications, such as replacing Indium Tin Oxide (ITO) in devices such as touch screens in smartphones.[11] Graphene has even been used in applications outside of electronics, such as cancer research[12] and energy storage,[13] showing the great potential of two-dimensional materials. While graphene is an amazing material, it is not without its flaws. Graphene is a semi-metallic material and lacks a sizeable band gap without functionalisation,[14] making it unsuitable for logic operations and optoelectronic devices. The band structure of graphene and frequencies it is suitable for use in photonics are shown in Figure 1.1. While graphene continues to find great success by solving some problems in electronics, other two-dimensional materials can make up for graphene's shortcomings.

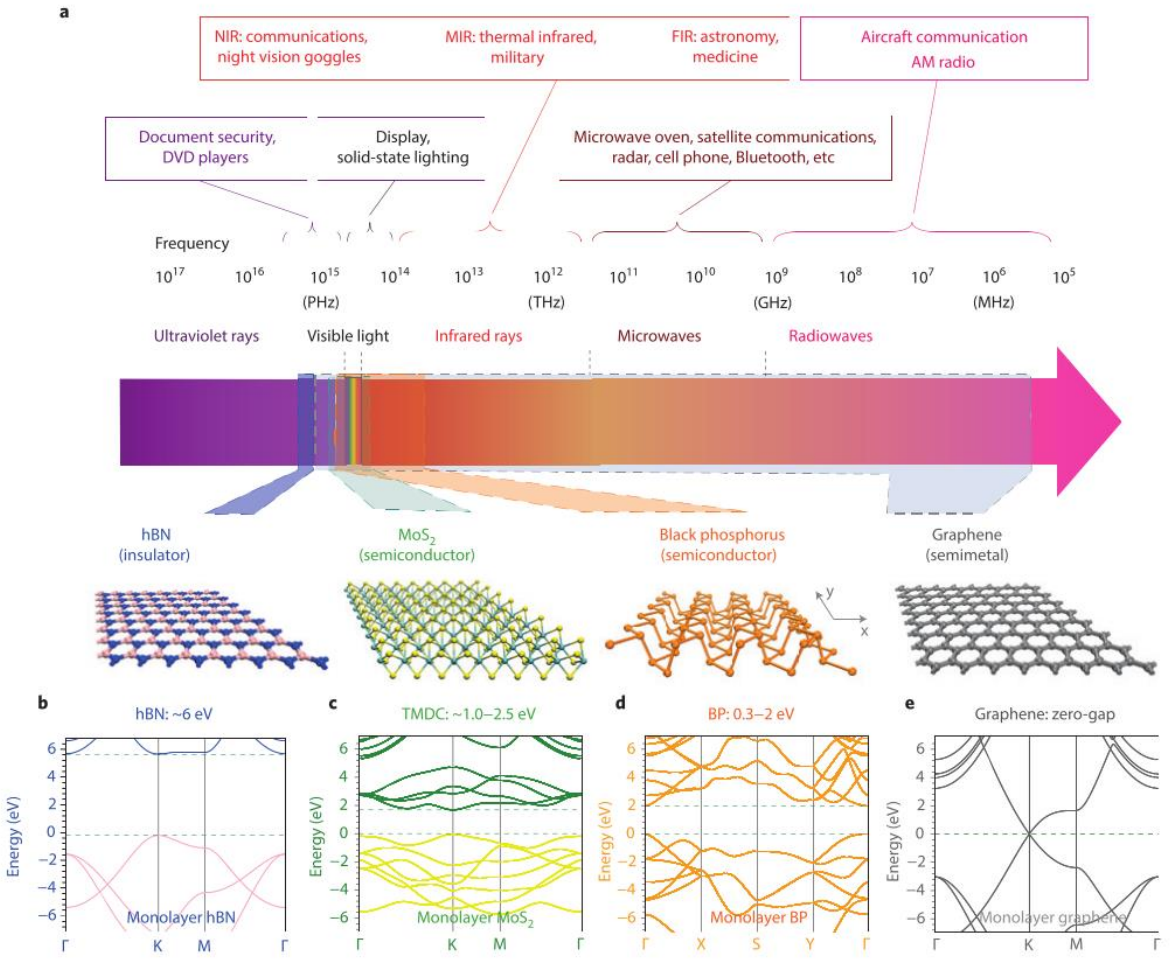

Figure 1.1: *(a) Applications across the electromagnetic spectrum are presented. The crystal structure of single layer hexagonal Boron Nitride (h-BN), Molybdenum Disulphide (MoS_2) which is a TMDC (transition metal dichalcogenide), Black Phosphorus (BP) and graphene are displayed. The region over which these materials can be used in the electromagnetic spectrum are shown by dashed areas. (b), (c), (d) & (e) The band structures of the monolayers of these materials are displayed and labelled on the diagram. Figure taken from Xia et al.*[15]

Transition Metal Dichalcogenides (TMDCs) are another family member of two-dimensional materials, but unlike graphene show semiconducting properties, making them a good prospect for flexible optoelectronics[4,5,16] and logic operations[17–19]. TMDCs, like all two-dimensional materials, have individual layers separated by Van de Waals forces. TMDCs however have a different crystal structure for an individual layer compared to graphene. Traditionally, due to those Van de Waals forces, TMDCs were used

as industrial lubricants[20] as the individual layers of TMDCs are held together weakly by that force. Each individual TMDC layer comprises a transition metal element layer, commonly molybdenum or tungsten, which is encapsulated by two covalently bonded chalcogenide layers, usually sulphur, selenium or tellurium. The band and crystal structure of monolayer MoS_2 are presented in Figure 1.1.

Because the TMDC crystal is a repeating structure of three layers, a difference in the stacking of the layers can even lead to different available phases for TMDCs,[17] whereas only one phase is available to graphene. The different phases of TMDCs consist of either a semiconducting or semi-metallic phase.[17] TMDCs can be grown into both of these crystal structures and even be changed between them by: applied strain,[21] temperature[22] or intercalation.[23]

The finite band-gap of TMDCs mean that they are well-suited, in their semiconducting phase, to the provision of field effect transistors (FETs) with high ON/OFF ratios and for applications in logic devices. Additionally, TMDCs have a strong light-matter interaction, allowing for FETs which are optically active.[24] A single layer of TMDC has a strong absorbance despite the strong interaction with light,[25] which comes from the change from indirect to direct band gap as TMDCs approach single-layer thickness due to quantum confinement.[26]

The semi-metallic phase of TMDCs is also of increasing interest, with applications ranging from: the increasing of carrier mobility (through changing the metal to semiconductor interface[27]), and the provision of Weyl semimetals,[28] (described as a three-dimensional analogue of graphene[29]).

Fortunately for 2D materials, black phosphorus (BP) fills the gaps left by TMDCs and graphene in the electromagnetic spectrum, with its band gap of 0.3 – 2.0 eV[30] being lower than the range for TMDCs at 1.0 – 2.5 eV.[15] Black phosphorus does have shortcomings, reacting very strongly to ambient conditions and must be encapsulated properly by another two-dimensional material, hexagonal boron nitride (h-BN) to prevent oxidation.[31] h-BN is often used for encapsulation, to protect other 2D materials from ambient conditions.[32] h-BN is an insulating material with a large band gap of ~6 eV[32] and can be used as an atomically thin gate dielectric.[3,33,34] Band and crystal structures for these materials are presented in Figure 1.1.

By using a selection of Van de Waals 2D materials such as graphene with its high conductivity, TMDCs for semiconductor channels and the insulating h-BN as a gate dielectric, creating electronics made entirely of 2D materials is a real possibility, allowing for fully flexible and atomically thin transistors.[2]

2D materials such as graphene and TMDCs were originally fabricated via mechanical exfoliation from bulk crystals. While mechanical exfoliation can be applied simply in a laboratory, large scale fabrication of 2D materials is now becoming possible through Chemical Vapour Deposition (CVD),[35–40] Physical Vapour Deposition (PVD)[41] and Molecular Beam Epitaxy (MBE)[42,43] techniques, allowing large area fabrication of any two-dimensional materials. Using these techniques it is even possible to grow 2D materials directly into heterostructures.[43,44] With a wide range of applications and large scale processing, TMDCs hold great promise in terms of having a big impact on the development of flexible electronics.

While some TMDC materials, such as MoS_2[45,46], have been extensively researched in recent years, other TMDCs are less well explored. Ideally, a full categorisation is required of all TMDCs in order to paint a picture of what is achievable for TMDCs in 2D optoelectronics. Different combinations of transition metal and chalcogen atoms lead to: changes in the band gap, electrical performance, reactivity in ambient conditions etc., which will impact the feasibility for device applications.

In this thesis, therefore, the material $MoTe_2$ provides the focus. $MoTe_2$ is considerably less well researched among the TMDCs but has a band gap of $\sim$1 eV which is similar to that of Si, one of the most widely used semiconductors. Thus, $MoTe_2$ is an exciting material but in general is overlooked in the literature to date. This may be because the Mo-Te bond is somewhat weaker than the equivalent bond in other TMDCs, meaning that $MoTe_2$ might be more strongly influenced by its environment (e.g. via detrimental oxidation). However, this relative weakness of the bonds means that $MoTe_2$ can also be influenced more readily by adsorbates, which can be used to enhance the performance of optoelectronic devices,[47] and be utilised in applications such as gas sensing.[48] The relatively weaker bonds also make $MoTe_2$ an excellent candidate as a 2D phase change material, with the smallest amount of energy per unit required to change phase.[49]

A comprehensive summary of electronic and optoelectronic devices using $MoTe_2$ is yet to appear in literature, despite some of the more unique applications available for this material. The device properties of $MoTe_2$ will therefore be examined in this chapter to provide a reference point for the work in this thesis, and as a reference for those studying this material.

1.1. $MoTe_2$ Research Highlights

The material $MoTe_2$ has gained popularity over the past 5 years, with a significant rise in research publications mentioning $MoTe_2$ from around 30 to 500 papers per year, as shown in Figure 1.2. This should be put into context though by comparison to the number of publications concentrating on other 2D materials, for example, MoS_2 had ~10,000 papers in 2017, with graphene at ~65,000. While $MoTe_2$ is not as widely researched as other 2D materials, the material is gaining in popularity due to the different opportunities $MoTe_2$ provides, with its smaller band gap similar to that of Si, possible phase change applications and newly emerging role as a Weyl semimetal.

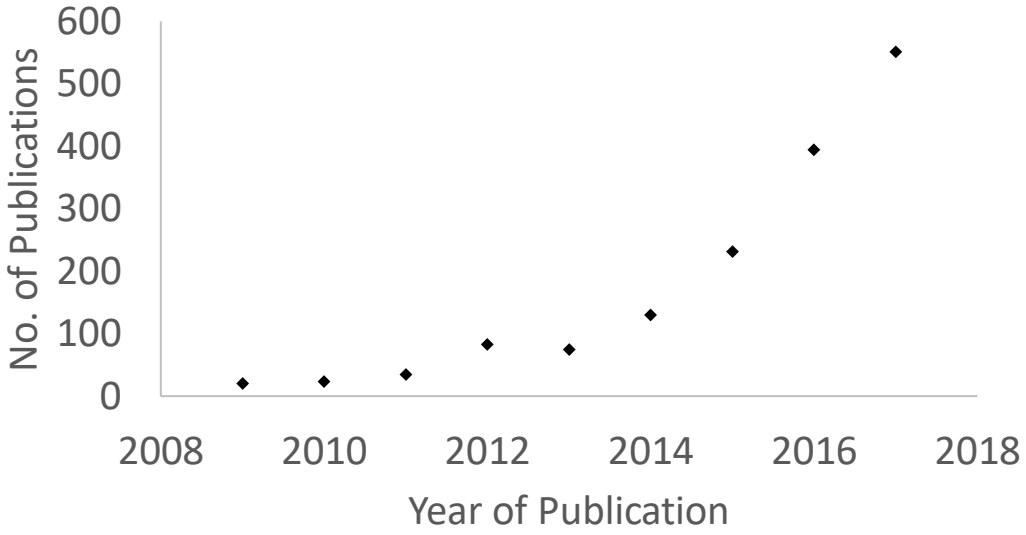

Figure 1.2: *Publications per year for the search term 'MoTe₂' on website 'dimensions.ai', climbing past 500 publications per year in 2017.*

MoS_2 is already well established as an excellent material for optoelectronics applications,[50] use as a memory[51] and can be readily created into monolayers through CVD growth.[52] $MoTe_2$ in the past few years is becoming a material which can perform a

different role due its weaker Mo-Te bonding energy of 0.3 eV,[53] which for example (and as already pointed out above) enables the possibility of structural phase changes induced by strain highlighted by Duerloo et al.[49] Indeed, changing the phase of $MoTe_2$ and using different phases to enhance the electrical properties is becoming more of a reality[27], with the semiconducting (2H) and semi-metallic (1T') phases used in a single device. In a paper from Cho et al.[27] the phase of $MoTe_2$ is irreversibly switched from the 2H to 1T' phase via laser irradiation. This is used to enhance the contact between the metal electrodes and the $MoTe_2$ semiconductor interface, increasing carrier mobility by modifying the Schottky Barrier. To achieve the same switching of phase in MoS_2, more drastic methods are required such as chemical functionalisation,[54] thus showing some of the potential advantages of using $MoTe_2$.

Growth methods such as Chemical Vapour Deposition (CVD)[36–38] are becoming widely used for $MoTe_2$, with growth in both semiconducting and metallic phases possible using different temperatures and pressures during the growth.[55–57] A recent discovery of a new topological state of matter is the Weyl semimetal, for which $MoTe_2$ is expected to be a candidate in its semi-metallic phase.[58] Different methods of growth for TMDCs are also now being utilized such as Molecular Beam Epitaxy (MBE)[42,43] and Physical Vapour Deposition (PVD)[41], with the ability to grow $MoTe_2$ on a wider variety of substrates[43] and different geometries.[42]

One major attraction for using $MoTe_2$ is its band gap – which is assessed in the following section from photoluminescence measurements (PL). $MoTe_2$ has a band gap of ~1.1 eV, which very similar to Si, which obviously has widespread use in optoelectronics. This smaller band gap (cf. other TMDCs[59,60]) of $MoTe_2$ provides coverage in the near infra-red (NIR) and visible wavelength regions for light-matter interaction, further expanding the spectral range of 2D materials. The evolution of the band gap with layer thickness, Raman results and growth techniques for $MoTe_2$ will be summarized in the following sections, before delving into the device physics of $MoTe_2$.

1.2. The Two Phases of $MoTe_2$

TMDCs have two main phases, the 2H (semiconducting) and 1T' (semi-metallic) phase. These two crystal structures are distinct, with 2H and 1T' having trigonal prismatic and

octahedral structures respectively, shown in Figure 1.3.[17] $MoTe_2$ in a study by Duerloo et al.[49] is shown to be the best candidate for a reversible phase change material,[49] however no reversible phase changes for $MoTe_2$ have been seen at present.

The phase change of $MoTe_2$ has been accomplished through irreversible means by Cho et al., where a laser was used to ablate the top layer of $MoTe_2$, but also induced a phase change to the top layer through the applied heat.[27] While a purely thermal phase change for $MoTe_2$ requires relatively high temperatures (880 ^{0}C), the laser used in Cho's work successfully induced a phase change at much lower temperatures (circa 400 ^{0}C), due it is thought to the creation of Te vacancies from the increased temperature. This reflects the fact that the $MoTe_2$ has a signature problem in the fact that the Mo-Te bond is relatively weak, which can cause issues with attracting adsorbates and becoming highly oxidised. However the weaker bonding also brings benefits: for example it allows for opportunities for $MoTe_2$ as a phase change material[49] and, as shown in this thesis, makes it possible to laser-thin $MoTe_2$ layer-by-layer, allowing the creation of samples to any desired thickness.

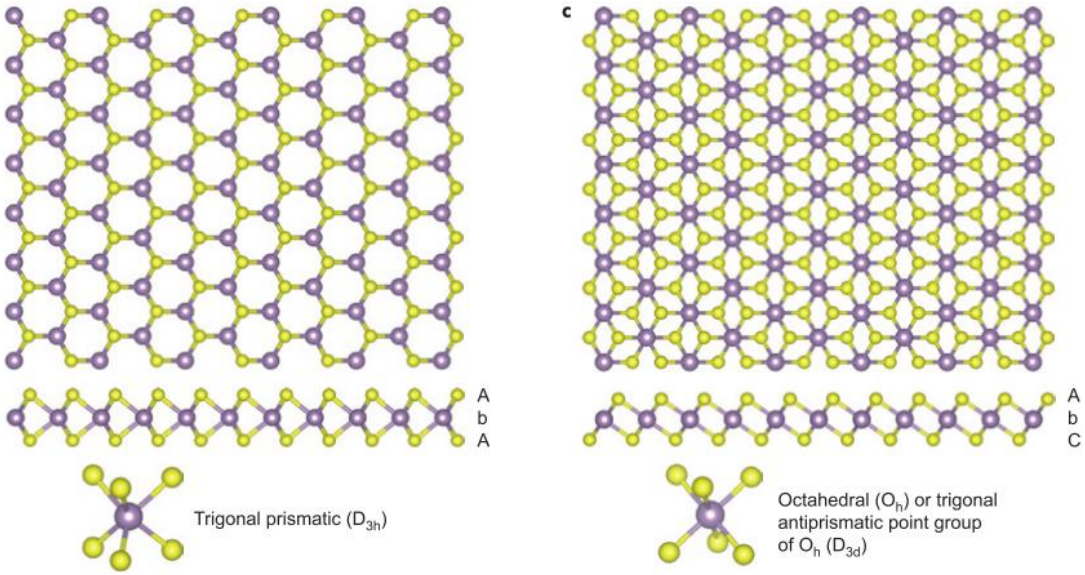

Figure 1.3: *Crystal structure of the 2H and 1T' phases of $MoTe_2$ from Chhowalla et al.*[17] *showing the difference in structure between the semiconducting and semi-metallic phases of TMDCs.*[17]

While already briefly explained in Section 1.1, the growth of TMDCs makes large scale operations and commercial viability possible. This thesis uses only mechanically exfoliated flakes for devices, whereas future studies should focus on CVD, MBE or PVD

grown $MoTe_2$ to produce work more relatable the greater scales used in industry. $MoTe_2$ can be grown into the 2H and 1T' phases, as shown by many research groups.[22,55,56] Using MBE, $MoTe_2$ can even be grown onto different geometries[42] and most excitingly directly onto other 2D materials like graphene,[43] which, if perfected could lead to the creation of large area heterostructures for flexible electronics and optoelectronics applications.

1.3. Electronic Structure of $MoTe_2$

The evolution of the band gap in TMDCs with decreasing thickness is a well-known phenomenon. Yoffe et al.[26], in a review paper published in 2002, summed up the results on TMDCs from working on bulk samples originally in the 1970s, including a simplified explanation for the evolution of the band gap.[26] The explanation relies on the classical example of particles in a box, where the available states due to quantum confinement decreases as the thickness of the semiconductor decreases. The fundamental difference between TMDCs and some other semiconductors is that the band gap becomes direct at the monolayer thickness, as reported by Mak et al. for MoS_2.[24]

A theoretical band structure for many TMDCs was created by Kumar et al.[61], where the reduction of the number of states due to the quantum confinement (by layer thickness reduction) is seen. A reproduction from Kumar et al. is shown in Figure 1.4.

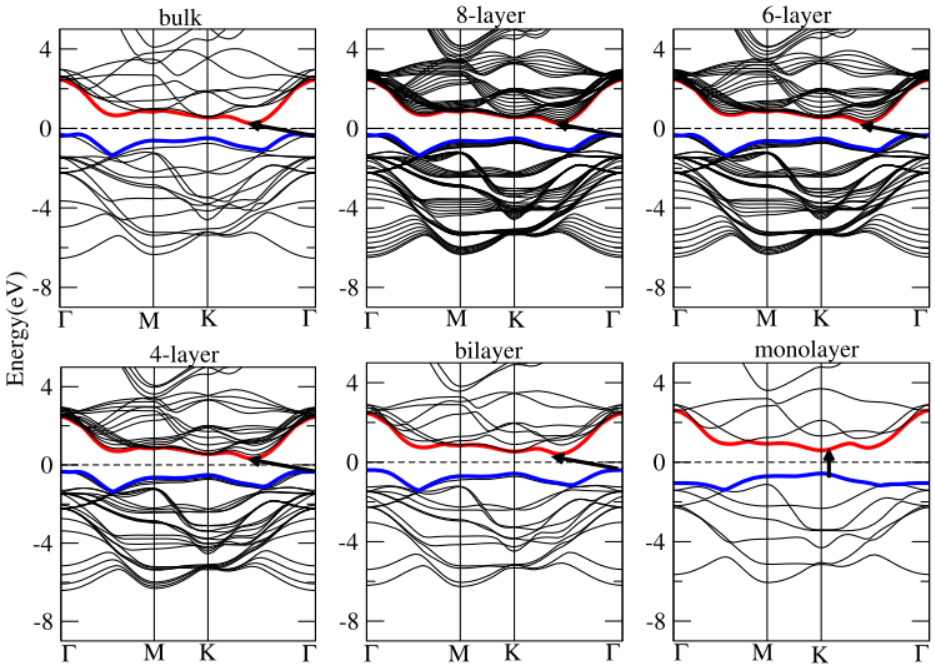

Figure 1.4: *Theoretical evolution of the band gap of $MoTe_2$ with decreasing layer thickness from Kumar et al.[61] The band gap crosses over from an indirect band gap to direct in the monolayer case (due to quantum confinement).*

In experimental studies of the band gap in $MoTe_2$, sizeable photoluminescence (PL) yields are observed for monolayer $MoTe_2$ because of the direct band gap. Some appreciable PL yields for up to four-layer thickness is seen by Ruppert et al.[62] and Lezama et al.,[63] showing that between one to four layers of thickness, $MoTe_2$ still shows strong light-matter interactions. The aforementioned authors PL results are shown in Figure 1.5.

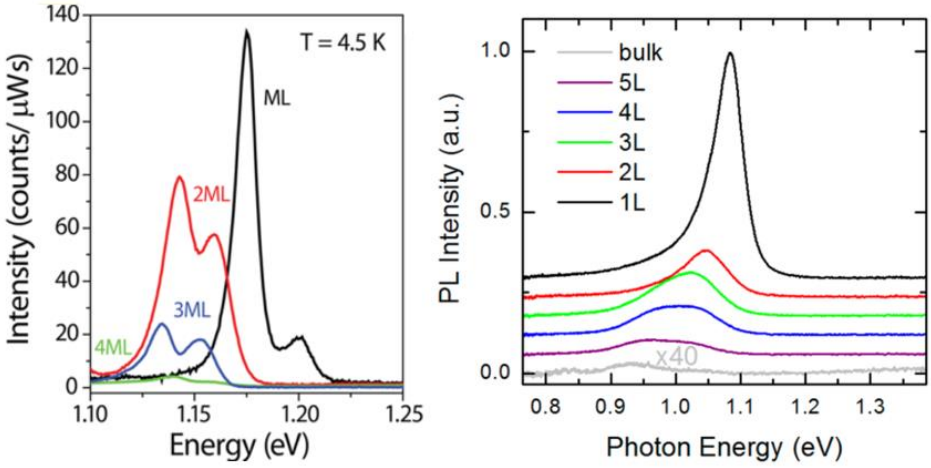

Figure 1.5: *PL results for $MoTe_2$ at cold temperatures (Lezama et al.[63]) and room temperature (Ruppert et al.[62]). Sizeable PL yields are obtained for samples up to 4 layers in thickness.*

In light of these PL results, flake thicknesses of four-layers are generally used for optoelectronic devices in this thesis, as they showed strong light-matter interaction along with good electrical properties. By comparison, MoS_2 does not show the same light-matter interaction for few-layered flakes, with noticeably lower PL yields at just two layers thick,[24] meaning MoS_2 is limited to use for optoelectronic devices at single-layer thickness.

1.4. Raman Spectroscopy

Raman Spectroscopy is an excellent tool for identifying the thickness of 2D materials, including graphene and TMDCs. Initial studies on the Raman spectra of $MoTe_2$ up to thirty layers in thickness were introduced by Yamamoto et al.[64] showing the evolution of the Raman peaks with a 532 nm laser (which is the same wavelength used in the Raman studies reported throughout this thesis). Three main peaks, the $\mathbf{A_{1g}}$, $\mathbf{E^1_{2g}}$ and $\mathbf{B^1_{2g}}$ situated between 150 and 300 cm^{-1}, at this 532 nm wavelength, vary greatly in their peak intensities between 1 to 5 layers in thickness, as shown in Figure 1.6.

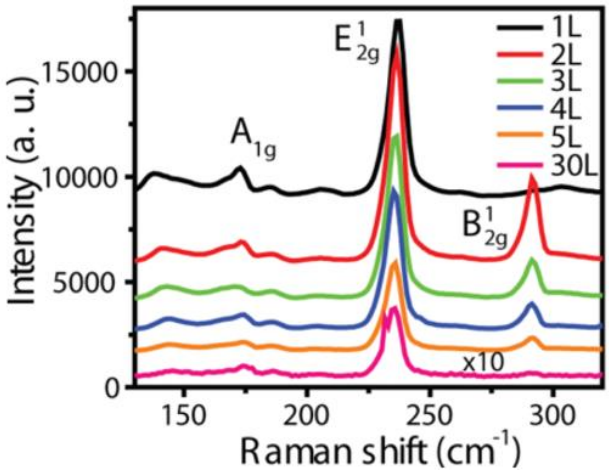

Figure 1.6: *Raman spectroscopy at 532 nm by Yamamoto et al.[64], showing the evolution of the Raman peaks as a function of number of $MoTe_2$ layers.[64]*

From Figure 1.6 it can be seen that the A_{1g} peak stays as the smallest in intensity overall, so the other two, $\mathbf{E^1_{2g}}$ and $\mathbf{B^1_{2g}}$, are used for distinguishing thickness. The $\mathbf{E^1_{2g}}$ peak position and intensity both change greatly with thickness, as does the $\mathbf{B^1_{2g}}$ peak. In particular, the $\mathbf{B^1_{2g}}$ is an inactive Raman mode for bulk phases and the monolayer and arises due to translation symmetry breaking.[64] This makes monolayer $MoTe_2$ easy to identify from the lack of this peak. The thickness of $MoTe_2$ flakes thus can be identified by examining the ratio of the height of these two peaks up to thicknesses of 5 layers. The phonon modes responsible for each of the peaks shown in Figure 1.6 and for bilayer $MoTe_2$ are shown from Yamamoto et al. in Figure 1.7.

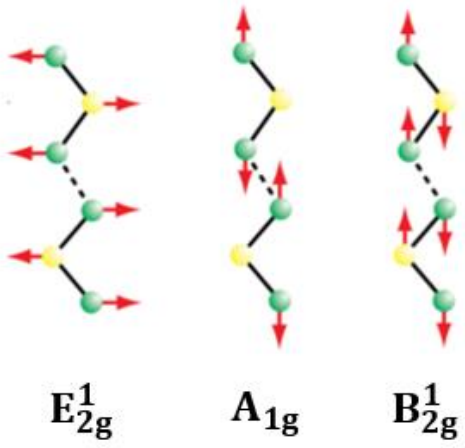

Figure 1.7: *Phonon modes of 2-layer $MoTe_2$ reproduced from Yamamoto et al.[64] from the three main Raman peaks seen between Raman shifts of 150 cm^{-1} to 300 cm^{-1}.*

1.5. Electronic Devices with $MoTe_2$

A considerable number of field effect transistors (FETs) using $MoTe_2$ have been seen in the literature, showing the remarkable properties of $MoTe_2$, such as high mobilities with Ohmic junctions,[27] controllable doping levels[65] and use in waveguides.[66] Typically, MoS_2 has shown n-type behaviour due to strong Fermi-level pinning[67], however $MoTe_2$ frequently shows a mix of doping with p-type[68,69], ambipolar[63,70,71] and n-type[27,72] devices all being reported. In light of this reported variation in device characteristics, an attempt to categorize and compare the range of mobilities and polarities for $MoTe_2$ FETs, with information on measuring conditions and metal contacts used, is therefore presented below. This list will be non-exhaustive, due to the size of the field, but provides a useful summary in terms of reported electrical properties of $MoTe_2$ – based devices.

Overall in Table 1.1 the mobilities range up to 45 cm^2/Vs, with 17 papers showing ambipolarity, 10 showing p-type conduction and 7 n-type. Overall there appears to be no correlation between the type of metal contact, flake thickness or polarity.

Based on the works reported in Table 1.1, the effects of the contact metals, measurement conditions, annealing parameters and use of encapsulation on the properties of $MoTe_2$ devices is discussed further in the following sections (along with some potential novel device applications). Before this, an overview of field effect transistors and the metal

contact/$MoTe_2$ interface will be provided to better understand the electrical results of $MoTe_2$ FETs.

Publication	Year	$MoTe_2$ Flake Thickness	μ_{FE} (cm^2/Vs) p-type	μ_{FE} (cm^2/Vs) n-type	Contact to $MoTe_2$	Conduction Polarity
Pradhan et al.[68], ACS Nano	2014	7	27	NA	Ti/Au	p-type
Lin et al.[70], Adv. Mater.	2014	3	0.3	0.03	Ti/Au	Ambipolar
Fathipour et al.[71], APL	2014	6	6	NA	Ti/Au	Ambipolar
Lezama et al.[73], 2D Mat.	2014	10	10	30	Ti/Au	Ambipolar
Cho et al.[27], Science	2015	5	NA	45	Cr/Au	n-type
Keum et al.[22], Nat. Phys.	2015	14	NA	40	Cr/Au	Ambipolar
Lin et al.[74], Adv. Mater.	2015	3	0.07	0.02	Ti/Au	Ambipolar
Xu et al.[75], ACS Nano	2015	8	26	7	Ti/Pd	Ambipolar
Nakaharai et al.[76], ACS Nano	2015	6	0.2	3.7	Ti/Au	Ambipolar
Heo et al.[77], Nano. Lett.	2016	4	27	20	Graphene	Ambipolar
Choi et al.[78], Adv. Func. Mat.	2016	16	35	11	Graphene	Ambipolar
Pezeshki et al.[69], ACS Nano	2016	5	20	NA	Pt	p-type
Yin et al.[79], APL	2016	16	25.2	0.06	Au	p-type
Yin et al.[79], APL	2016	10	0.4	0.5	Cr/Au	Ambipolar
Nakaharai et al.[80], ACS App. Mat. Int.	2016	4	NA	8	Ti	n-type
Nakaharai et al.[80], ACS	2016	4	12	NA	Pt	Ambipolar

App. Mat. Int.						
Ji et al.[81], ACS App. Mat. Int.	2016	11	22	NA	Ti/Au	Ambipolar
Wang et al.[82], Nanoscale	2016	8	4.3	7.6	Cr/Au	Ambipolar
Empante et al.[56], ACS Nano	2017	1	0.03	NA	Sc/Au	p-type
Larentis et al.[83], ACS Nano	2017	2	18	8	Pt	Ambipolar
Qi et al.[84], 2D Mat.	2017	8	15	NA	Au	p-type
Qu et al.[85], Adv. Mat.	2017	16	NA	5	Cr/Au	n-type
Amit et al.[86], Adv. Mat.	2017	4	0.13	NA	Ti/Au	p-type
Chen et al.[87], ACS App. Mat. Int.	2017	6	6.5	NA	Al/Au	n-type
Chen et al.[87], ACS App. Mat. Int.	2017	6	NA	1	Al/Au	p-type
Sung et al.[88], Nat. Nano.	2017	8	4	NA	Au	p-type
Kim et al.[67], ACS Nano	2017	1	NA	NA	Au	Ambipolar
Ji et al.[89], App. Phys. Lett.	2017	15	7	NA	Cr/Au	Ambipolar
Ji et al.[72], ACS App. Mat. Int.	2017	11	NA	8	Ti/Au	n-type
Feng et al.[90], 2D Mat.	2017	9	~0.1	NA	Ti/Au	n-type
Chang et al.[65], Adv. Mat.	2018	6	1.3	0.003	Ti/Au	n-type

Townsend et al.[91], 2D Mat.	2018	10	0.1	NA	Au	p-type
Shackery et al.[92], Mat. Chem. C	2018	12	14	NA	Pt/Au	p-type
Luo et al.[93], Adv. Func. Mat.	2018	9	NA	20	Ag/Au	Ambipolar

Table 1.1: *Overview of the properties of $MoTe_2$ channel transistors (FETs) reported in the literature, noting the year of publication, thickness of layer, mobility of p and n-type conduction where appropriate, metal contact used and polarity of conduction.*

To better understand these results from literature, the basic operation of a FET will be provided for context in the following section.

1.5.1. Field Effect Transistor Operation

FETs are devices used to control the flow of current in a three-terminal structure. In FETs, current flows from the source to the drain terminal through the semiconductor channel, and this current is controlled by the gate terminal. Assuming that the carriers in the channel region are electrons (n-type conduction), when a positive gate bias is applied, the channel will open increasing the flow of electrons. The positive gate bias allows for n-type conduction, as electrons form a conductive channel in between source and drain. A negative gate bias will turn off the channel as the field effect from the capacitive gate is the same polarity as the charge carriers. For p-type conduction, the opposite gate biases are used to open and close the FET. A schematic for a FET is shown in Figure 1.8.

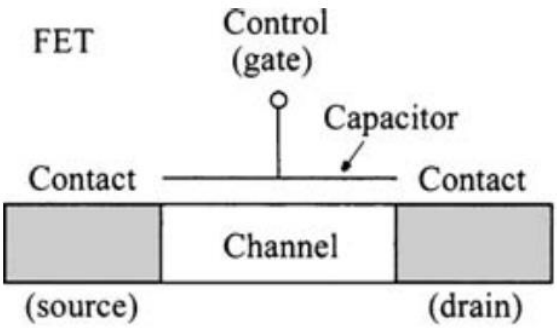

Figure 1.8: *Schematic of a FET from Physics of Semiconductors by Sze et al.*[94] *Current flows from the source to the drain terminal. Current is controlled capacitively by an electric field from the gate terminal.*

For devices with 2D materials, to test optoelectronic properties the FET configuration is commonly used, with the TMDC acting as the channel, deposited metals act as the source and drain terminals and an underlying gate of highly doped Si underneath a thermally grown insulating SiO_2 region is used as a gate electrode. A schematic for a typical $MoTe_2$ FET is provided in Figure 1.9.

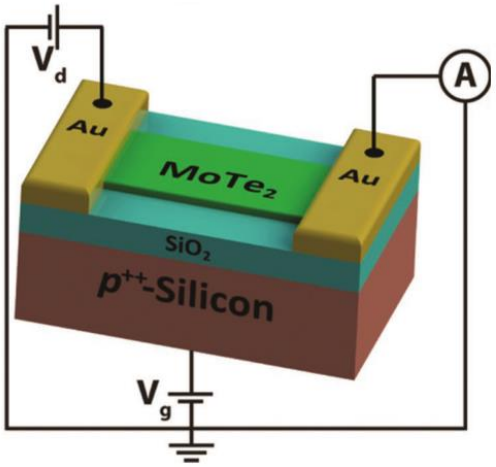

Figure 1.9*: Schematic for a typical $MoTe_2$ FET device. $MoTe_2$ is on top of a SiO_2 dielectric, with highly doped p^{++} Si underneath the SiO_2 used as a gate terminal to apply a field effect. Source and drain terminals are here created by depositing Gold on top of the $MoTe_2$ flake. The drain current, I_{ds} is measured in series with the applied bias. All the terminals are connected by a common ground to reduce electrical noise. Figure reproduced from Amit et al.*[86]

1.5.2. Schottky Barrier Formation at the Metal Contact/$MoTe_2$ Interface

The metal used in the metal/TMDC interface is very important for the electronic properties of the TMDC. A Schottky barrier forms at this interface, which determines how the device performs and can even affect the polarity of the FET, depending on the work function of the metal used for the contact.

Schottky barriers arise from the difference in work function between metals and semiconductors, and are the definition of the interface in the ideal case. Figure 1.10 shows the formation of a Schottky barrier as a metal and n-type semiconductor are brought together. In Figure 1.10(a), $\mathbf{q}$ is the charge of an electron, $\boldsymbol{\varphi_m}$ is the metal work function, $\boldsymbol{\varphi_n}$ is the semiconductor work function, $\boldsymbol{\chi}$ is the electron affinity, $\mathbf{E_C}$ is the conductance band, $\mathbf{E_V}$ is the valence band and $\mathbf{E_F}$ is the Fermi energy. In Figure 1.10(a), the metal (left) and semiconductor (right) are in separate systems and are not interacting. In Figure 1.10(b) the metal and semiconductor are brought together. The new terms are $\boldsymbol{\phi_{Bn0}}$, the limiting value of Schottky barrier height, $\mathbf{W_B}$ is the width of the barrier and $\boldsymbol{\psi_{bi}}$ is the built in potential. As contact between the metal and semiconductor occurs, the Fermi energy of the semiconductor and work function of the metal align, the Fermi level of the semiconductor must lower to achieve this, causing the $\mathbf{E_C}$ and $\mathbf{E_V}$ bands to bend. This interface is a potential barrier for the electrons which must tunnel through for conduction in the device. The height of the barrier in the ideal case is dependent on the work functions of both the metal and semiconductor.

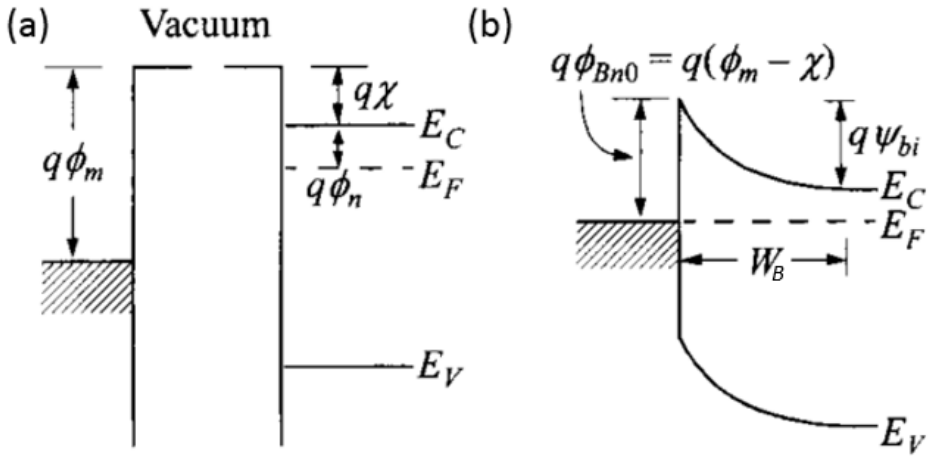

Figure 1.10: *(a) Band diagrams for a metal (left) and n-type semiconductor (right) in separated systems. (b) Formation of the Schottky barrier between the metal and semiconductor interface.*

For some semiconductors, especially $MoTe_2$[91], the location of the Schottky barrier can be determined by Fermi-level pinning (FLP). FLP occurs when the surface state density is high (common for 2D materials due to their high surface area to volume ratio), and the metal work function will align with where the surface states exist between the conductance and valence band. This is visualised in the band structure for p-type $MoTe_2$ by Townsend et al.[91] in Figure 1.11.

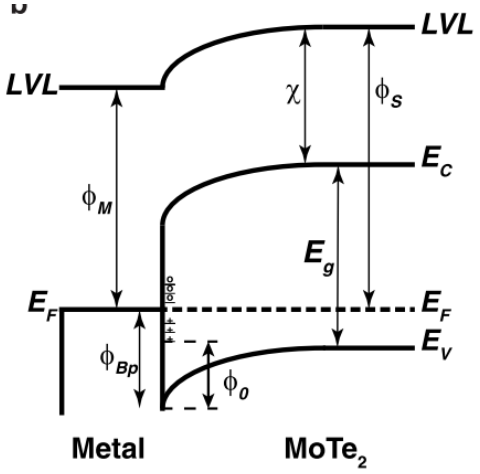

Figure 1.11: *Band diagram for the formation of a Schottky Barrier (SB) in $MoTe_2$. E_C conduction band edge, E_V = valence band edge, E_g = band gap, χ = electron affinity, LVL =*

local vacuum level, E_F = Fermi level, φ_M = metal work function, φ_s = $MoTe_2$ work function, φ_{Bp} = barrier height and φ_0 = energy of the mid-gap states. Trap states are shown at the metal/$MoTe_2$ interface which fix the position of the Schottky Barrier. Taken from Townsend et al.[91]

1.5.2.1. Effect of Contact Metal on Electrical Properties

The effect of the type of contact metal used to provide the FET electrodes (drain and source) should determine the effect of polarity in the ideal case without FLP, due to the different work functions of metals which create different Schottky Barrier heights. However, in $MoTe_2$, the existence of FLP has been shown,[67,91] which affects the Schottky barrier and therefore the polarity and conductivity of FETs. Studies using different contact metals have shown that the carrier polarity is indeterminate of the metal used,[83,87] meaning the doping of $MoTe_2$ is determined by FLP. However, it is noted that the FLP reported in some papers appears less strong, leading to the choice a of metal contact having a significant impact on conduction polarity.[80]

1.5.3. Effect of Ambient and Vacuum Conditions on MoTe2 Conduction Polarity

Not only are the electrical properties of $MoTe_2$ devices determined by the metal contact/$MoTe_2$ interface, they depend strongly upon the environmental conditions in which the device is measured. For other TMDCs such as MoS_2 which are more chemically stable, measuring FETs in air leads to small changes in hysteresis, from adsorbates creating trap states.[95] Hysteretic effects are even stronger in $MoTe_2$, due to the weak Mo-Te bonds[53] that go on to form Te vacancies,[85] to which adsorbates are very strongly attracted in ambient conditions.

The adsorption of dopants through water molecules and oxygen in the atmosphere changes the doping of $MoTe_2$ transistors towards p-type doping. As shown by Chang et al., the doping from adsorbates can be removed via applying high source-drain bias in vacuum, with a resulting reversible change in doping noted from p-doped in air to n-

doped in vacuum.[65] In this thesis, typically the devices are measured in ambient conditions for electrical and optoelectronic measurements. However some measurements are conducted at vacuum, showing a change from strong p-type doping to ambipolar and even n-type doping.

1.5.4. Effects of Encapsulation and Capping Layers

Encapsulation using films/flakes of h-BN is commonly used to improve the electrical performance of devices by protecting them from ambient conditions.[81,83] Qu et al. also used Al_2O_3 capping layers to encapsulated $MoTe_2$, which improved the longevity of $MoTe_2$ transistors over a 3 month period.[85] No significant change except a nominal drop in the mobility was observed using the Al_2O_3 capping, whereas the pristine $MoTe_2$ device showed significant changes in doping over the 3 months. However, Al_2O_3 capping introduced n-type doping into the channel, as also noted by Ji et al.[81]

Using h-BN as an encapsulating layer does not cause the change in doping levels observed with Al_2O_3, presumably since h-BN is chemically very inert. Indeed, work by Sirota et al.[96] shows the protective capabilities of h-BN, showing no change in the doping of $MoTe_2$ from prolonged heating and no change in mobility up to 100 ^{0}C.[96] By fully encapsulating $MoTe_2$ with pristine h-BN, complex electronics alike to integrated circuits are possible, taking advantage the ambipolar nature of $MoTe_2$.[78,83] However, a potential drawback of using other 2D materials, such as h-BN, for capping of TMDCs can be that the stamping process used to create stacks of 2D materials can introduce adsorbates trapped between the various layers of the stack.[97]

1.6. $MoTe_2$ Optoelectronic Devices

$MoTe_2$ photodetectors are a growing field since 2016, with work published from this thesis contributing to the field. The use of $MoTe_2$ for photodetectors in the visible[47,98,99] or near-infrared (NIR)[100] has received particular attention. While the band gap of multilayer $MoTe_2$ ($\sim$0.9 eV, $\sim$1380 nm) is higher in energy than the 1550 nm wavelength commonly used for communications technologies, detectivity at such a wavelength has been seen by Liu[98] and Huang et al.,[101] due to the presence of tail end band states.[102]

Photoresponsivities as high as 2560 A/W have been reported by Yin et al.[79], achieved by taking advantage of photogain at very low light intensities. The photogating mechanism in $MoTe_2$,[79,98,99,101] is discussed in detail in this thesis, in Subsection 3.3.2. The photogating mechanism is only seen using higher energy photons (1.8 – 3.1 eV) in literature, showing that energies far above the band gap of $MoTe_2$ (~1.0 eV) are required for the photogating mechanism to work.

Spatial photocurrent microscopy (SPCM), is used to identify other photocurrent mechanisms for TMDCs, where the regions which produce photocurrent are identified. For $MoTe_2$ devices the origin for photocurrent has been reported by Liu. et al at the metal/semiconductor interface.[98] This photocurrent mechanism at the interface is different from the high gain photogating mechanism, as it occurs without the effect of an applied gate, using only a bias voltage. Both the photogating and SPCM mechanisms were first observed in $MoTe_2$ by Octon et al.,[47] where $MoTe_2$ FETs are examined as photodetectors with a 685 nm laser. This data on SPCM and the photogating effects in $MoTe_2$ are present in Chapter 3 of this thesis.

The ability to use $MoTe_2$ as a gas sensor under ultra-violet (UV) light illumination was demonstrated by Feng et al.,[48] where UV light is used to remove O_2 and other adsorbates, allowing active sites on $MoTe_2$ to be highly sensitive for gas detection. In Chapter 5, in our transient measurements, again taken before the publication of Feng et al., we see evidence of a negative photocurrent with a 473 nm (near UV) laser, which is associated with the removal of adsorbates which cause doping.

In this thesis, the photoresponsivity of pristine and laser-thinned $MoTe_2$ is assessed, along with the photoresponse speed and the mechanisms for photodetection, over a range of visible wavelengths. For lower energy visible light in air, $MoTe_2$ shows similar mechanisms to other TMDCs of the photogating effect[103,104] when the gate is modulated; without an applied gate, an effect at the metal contact/$MoTe_2$ interface appears to be the mechanism. For the higher energy visible light, mechanisms involving the removal of adsorbates, similar to when exposed to UV light as reported by Feng et al.[90], is the dominant mechanism. Hexagonal Boron Nitride is used to isolate $MoTe_2$ from the substrate and is used for encapsulation in this thesis, to try and create faster and more efficient photodetectors. A summary of the use of $MoTe_2$ in 2D heterostructures is

therefore provided below to illuminate the impact that the layering of TMDCs and other 2D materials can have on photodetector device performance.

1.6.1. Heterostructures for Optoelectronic Applications

Research on heterostructures fabricated using $MoTe_2$ falls into two main categories – using graphene as contacts and using two different TMDCs to form a p-n junction for new and exciting optoelectronic properties. Devices using graphene contacts show similar performance to pristine $MoTe_2$ devices, with high photoresponsivity, e.g. of 87 A/W shown by Wang et al.[105] and fast rise and fall times on the order of 10 μs[106] (and comparable to those achieved in this thesis – see Chapter 3).

More ambitious reported use of $MoTe_2$ in heterostructures involve the use of multiple transfers of 2D materials for devices. For example, by using graphene electrodes for the source, drain and gate with encapsulation with an h-BN layer, the properties of $MoTe_2$ transistors can be controlled with precision, as shown by Heo et al.[77] $MoTe_2$ has even been used up to 1 GHz frequencies when introduced into a waveguide with graphene contacts.[66]

As pointed out above, the other prominent heterostructure devices using $MoTe_2$ are for the creation of p-n junctions. Due to the commonly shown ambipolar or p-type properties of $MoTe_2$, it is suitable for use with other TMDCs which generally show n-type doping, as in the case of MoS_2. By using a p-n junction, the overlapping of two different TMDCs can be used as an area to separate photo-excited carriers.[69,107] Interestingly if both materials used in the p-n junction have a direct band gap, then it is possible to form an interlayer band gap between the two materials. For MoS_2 and $MoTe_2$ this band gap is defined from the valence band edge of $MoTe_2$ to the conduction band edge of MoS_2, which is ~0.65 eV. This is suitable for the 1550 nm communications wavelength, at which Zhang et al. showed significant photocurrent from the interlayer gap.[100]

1.7. Thesis Outline

In this thesis, the optoelectronic properties of $MoTe_2$ materials and devices is studied in detail. Firstly, in Chapter 2, the experimental procedures for identifying the quality and thickness of $MoTe_2$ are examined. This experimental chapter also highlights the metrics used to determine the quality of $MoTe_2$ FETs and their optoelectronic performance, as well as the in-house equipment built to attain these metrics.

Chapter 3 examines the performance of $MoTe_2$ as a photodetector in the visible part of the spectrum (using a 685 nm laser for illumination), as well as highlighting the mechanisms which provide $MoTe_2$ with (relatively) high values for photoresponsivity and fast photoresponse times (fast as compared to other TMDC devices). Trap states in $MoTe_2$ are found to be an important part of the mechanism responsible for creating large values of photoresponsivity.

In Chapter 4, the nature of trap states in TMDCs is examined further and explained from a theoretical standpoint that confirms the importance of adsorbates on the properties of $MoTe_2$. This further proves the dominant photogating mechanisms present in photocurrent measurements reported in Chapter 3. The trap states in TMDCs are shown to belong to two separate mechanisms with one linearly dependent upon the drain-source voltage and the other independent of it.

Where trap states dominate the electrical and optoelectrical performance of $MoTe_2$, the effect of using higher energy lasers on $MoTe_2$ is examined, since such higher energies can remove adsorbates on the surface of $MoTe_2$. This removal of adsorbates shows the possibility of creating a negative photocurrent during transient photocurrent and gated photocurrent measurements, as reported in Chapter 5.

While mechanically exfoliated flakes of $MoTe_2$ are commonly used for research, methods to ensure the thickness and quality of flakes is required in the large-scale processing of $MoTe_2$. The ability to use a laser to thin $MoTe_2$ layer-by-layer at any thickness is thus developed in this thesis to ensure a level of quality control unseen previously for $MoTe_2$. Whereas most thinning mechanisms reported in the literature rely upon an increase of temperature to sublimate TMDCs, the technique developed in this thesis for $MoTe_2$ relies strongly upon the relative humidity during laser exposure and exploits a photochemical approach that is extremely precise and operates at very low laser powers. This provides

a further example of how the weaker bonds between Mo-Te (cf. other TMDCs) can in fact be utilised in an advantageous manner.

The conclusions of the work are presented in Chapter 7, along with suggestions for future research directions.

2. Experimental Methods

In this chapter, the methods for fabrication and characterisation of 2D $MoTe_2$ films are outlined. Note that for the work presented in this thesis only mechanically exfoliated flakes are used, whereas in the future larger scale deposition methods such as CVD, PVD or MBE growth will undoubtedly be used so that many devices at a time can be fabricated for industrial applications.

The chapter begins with details for the fabrication of 2D flakes and FET devices made from them, including some information on the annealing parameters which improve the device performance. A section on the flake stamping technique used to create heterostructures from mechanically exfoliated flakes is also included, as this technique is used in this work to encapsulate $MoTe_2$ flakes with 2D hexagonal boron nitride (h-BN).

Methods of identifying and checking the quality of $MoTe_2$ samples, including Raman spectral analysis, surface roughness measurements using atomic force microscopy (AFM) and the assessment of photoluminescence (PL) yields are given. Finally, the electrical and optoelectrical systems used to measure $MoTe_2$ materials and devices will be discussed, which form a homebuilt system allowing optoelectronic measurements in vacuum. Figures of merit for electrical and optoelectronic systems which are used to categorize the effectiveness of the $MoTe_2$ photodetectors are also provided and explained.

2.1. Fabrication of Flakes and Devices

The mechanical exfoliation of TMDCs requires different preparation from graphene flakes, due to the difference in stiffness between the two types of materials.[108] This is addressed in this section, along with the methods used for fabrication of FETs. Annealing methods to improve FET electrical performance and the development of heterostructures are also included in this section.

2.1.1. Mechanical Exfoliation

$MoTe_2$ flakes were created by mechanical exfoliation from bulk crystals of $MoTe_2$ supplied by HQ graphene. A low-tack tape from LoadPoint (6033), normally used for the dicing of silicon wafers, was used to peel flakes away from the bulk sample and for flake thinning. Flakes created in this way were relatively small in area, with maximum sizes of around 10 μm^2. Flakes on the tape were then pushed gently, without forming air bubbles, on to a clean Si/SiO_2 wafer. Flakes created with more than 10 peels of tape, or pressed with great force, were generally very small in size (< 1 μm^2) due to the brittle nature of TMDCs. To create larger area flakes, a different method was therefore used.

Larger area flakes were created by using a polydimethylsiloxane (PDMS) stamp, where after peeling the tape with $MoTe_2$, an area of the tape is transferred to the PDMS stamp, then the PDMS stamp is used to transfer directly onto the Si/SiO_2 wafer. The viscoelastic properties of the PDMS stop the flakes from rupturing, ensuring that the flakes are larger in area than obtained by the tape method alone. This approach is similar to the method reported by Li et al.[108]

Before the transfer of any flakes, wafers were cleaned using acetone followed by isopropyl alcohol (IPA), with sonication in both chemicals for 20 minutes. It was found that $MoTe_2$ flakes transferred onto wafers cleaned by O_2 plasma (a common cleaning method) caused rapid material degradation, due most likely to the presence of O_2 from this treatment (indeed, the degradation of $MoTe_2$ on oxygen plasma cleaned substrates has been reported by Ruppert et al.[62]).

2.1.2. Device Fabrication

To create FET devices, $MoTe_2$ was deposited onto Si/SiO_2 substrates where the Si was highly doped (p++) and was used as the back gate and the SiO_2 (300 nm) was used as the gate dielectric. After flakes were deposited onto the wafers, electron beam lithography was performed to pattern device electrodes, contacts etc.

To begin lithography, a poly-methyl methacrylate (PMMA) photoresist (950K A4) was spin-coated on to the sample to a thickness of 200 nm to ensure proper lift-off after metal evaporation. To minimize contact time between PMMA and $MoTe_2$, the photoresist was

spun immediately before electron-beam lithography was carried out. After the lithography, a developer solution of isopropyl alcohol (IPA), methyl isobutyl ketone (MIBK) and methyl ethyl ketone (MEK) was used in a ratio of 15:5:1 to develop the exposed PMMA. Samples were developed for 30 seconds then the developing was quenched in IPA only. This technique was used for all devices.

With the contact regions exposed, post-lithography, metal evaporation took place in two different systems: a thermal evaporator and an electron beam evaporator. In these systems, different metals were available as contacts (Cr in thermal, Ti in electron beam, Au in both systems). In the thermal evaporator, the sample was baked during the process at a temperature <100 ^{0}C. In the electron beam evaporator, less heating takes place due to the electron beam not creating excess heat. Using both evaporators, high quality devices with good electrical properties were achieved. A pictorial summary of the device fabrication process is provided in Figure 2.1, along with images of a $MoTe_2$ flake before and after contacts have been deposited.

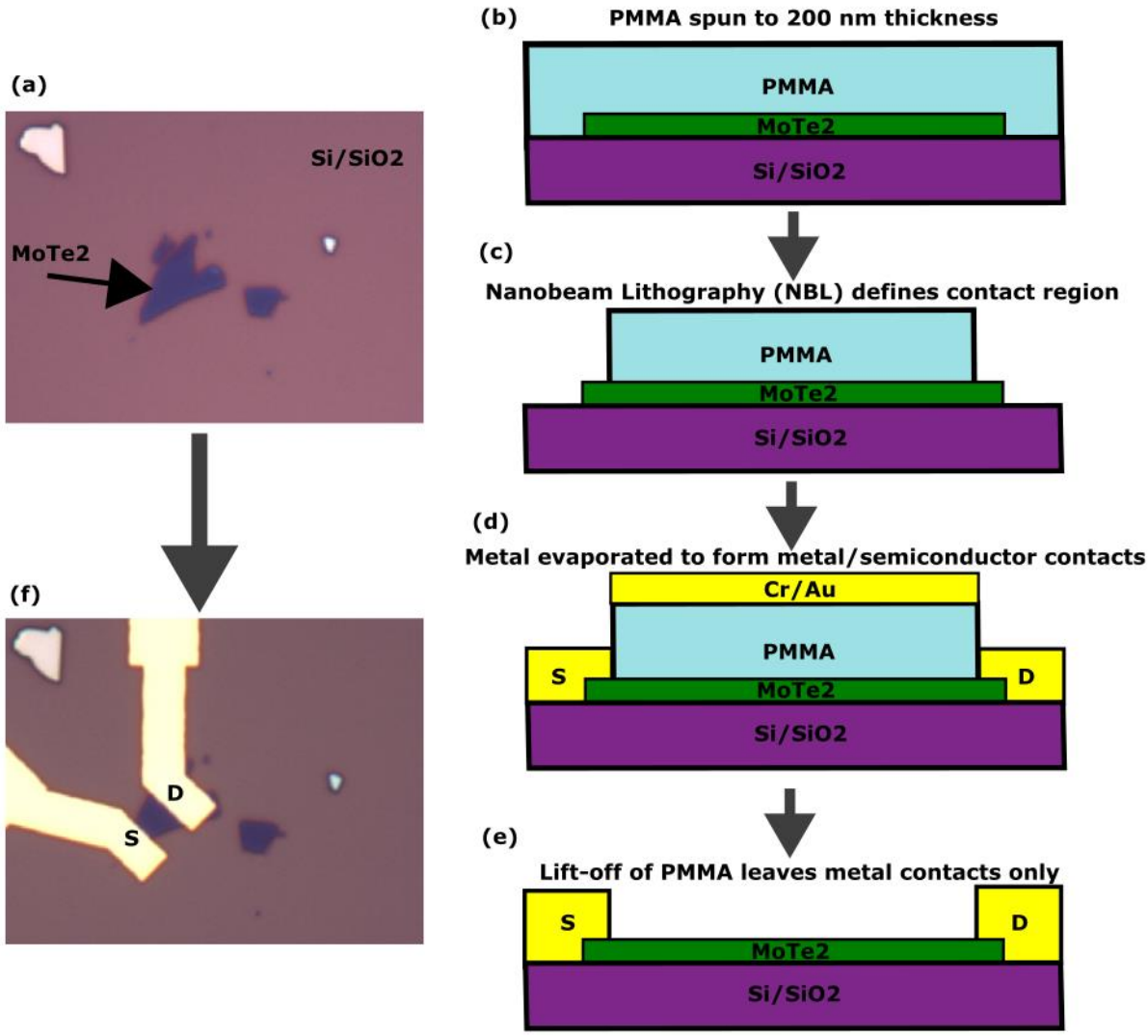

Figure 2.1: *(a) Image of a four-layer $MoTe_2$ flake on a SiO_2/Si (300 nm thick SiO_2) substrate before device fabrication. (b) – (e) Summary of the device fabrication process. (b) PMMA is spun as a photoresist on the substrate. (c) Nanobeam Lithography defines the contact regions with $MoTe_2$. PMMA areas affected in the NBL are removed using developer solution. (d) Contact metals (Cr/Au, 5/50 nm) are deposited on the substrate. (e) PMMA is removed using acetone revealing the finished device. (f) Image of the four-layer flake from (a), with metal contacts forming the source and drain terminals connected to the flake.*

Devices were annealed post contact fabrication, to improve the electrical contact interface and remove adsorbates from the $MoTe_2$, the semiconductor channel. Devices were annealed by two methods in this thesis. The first annealing process takes place in a glass tube furnace at 200 ^{0}C in Ar/H_2 (90%/10%) for 2 hours, with a warm up time of 30

minutes. This combination of gases were used as Ar is stable and inert and H_2 should react strongly with the PMMA residues removing them and improving field effect mobility. A lower annealing temperature is used for $MoTe_2$ than typically used for the more stable MoS_2 which is often annealed up to 400 ^{0}C,[109] due to the weaker bonds present in $MoTe_2$ which can cause layers to sublimate at higher temperatures[110].

The second annealing method used a Jipelec Rapid Thermal Processor (RTP) at 250 ^{0}C in vacuum conditions for 2 hours. Devices annealed in this way had higher mobilities and lower contact resistances, potentially due to the removal of more residues from the lithography process, the annealing environment or higher temperatures used.

Approximately 200 devices were created by this method, with a 40% success rate for fully working devices. The low percentage of working devices stems from the high number of monolayer devices that were tested (which typically show poor electrical performance) and issues with SiO_2 back gates breaking, making gated measurements not possible. A summary of the mobility and total device resistance as a function of flake thickness will be provided in Section 2.4.

2.1.3. Creation of Heterostructures

Heterostructures with h-BN and other TMDCs were made to try and improve the optoelectronic performance of TMDCs through a method using a Polydimethylsiloxane (PDMS) stamp and a microscope setup. The stamping methodology was taking from Castellanos-Gomez et al.,[97] Figure 2.2 shows a schematic of this transfer process. To begin this process, a mechanically exfoliated 2D material flake is adhered to a PDMS stamp. This stamp is then adhered on to a glass slide, where the glass slide is attached to a micromanipulator under a microscope. The desired flakes of 2D materials for the transfer process (one on the stamp, the other on a substrate) are aligned underneath a 50x long working distance (LWD) lens. The PDMS stamp is lowered and makes contact with the substrate until the two flakes are in direct contact. When full contact is made, the PDMS stamp is very slowly (~1 μm/min) removed, leaving both flakes aligned on the substrate. Due to stronger Van de Waals forces between the flakes, the flakes of h-BN or $MoTe_2$ used in the heterostructure procedure attach strongly to the flake on the substrate of SiO_2. This

is made possible from the viscoelastic properties of the PDMS which when peeled very slowly can release the flakes.[111]

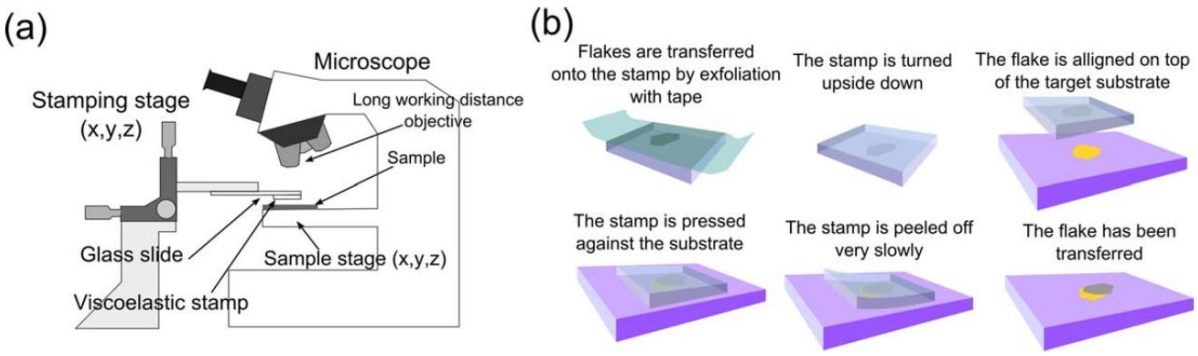

Figure 2.2: *Experimental setup for transfer of flakes through the stamping method. (a) Schematic of the stamping setup, with a microscope used to align the flakes over one another. Micromanipulators on the stamping stage are used to bring the glass slide in contact with the substrate with micron scale precision. (b) Summary of how the heterostructures are made using the PDMS stamping technique. Images used from Castellanos-Gomez et al.*[97]

As noted by Castellanos-Gomez et al.[97], some detrimental effects can occur related to small bubbles forming between the two layered materials, which could not be removed even through annealing steps. This is illustrated in Figure 2.3 (note here that the bubbles formed after the initial stacking of the heterostructure when stored in a low vacuum desiccator, and changed positions slightly upon annealing in Ar/H_2, but could not be entirely removed).

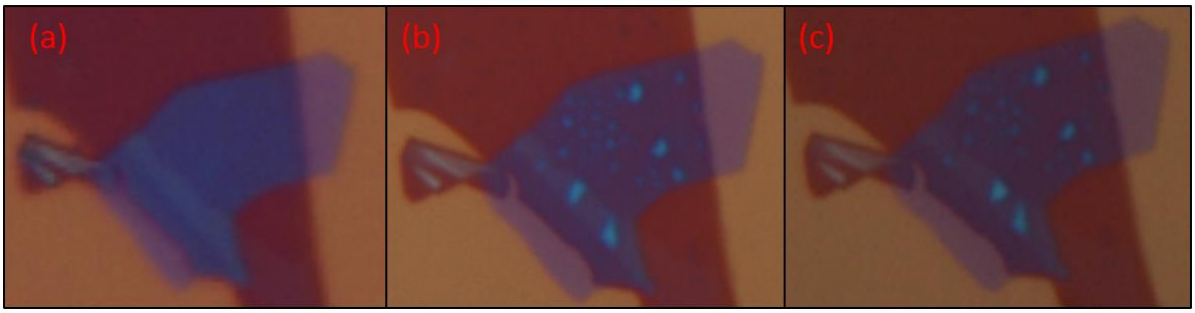

Figure 2.3: *h-BN underneath $MoTe_2$. (a) Shows the heterostructure as fabricated with the h-BN flake around 15 μm in length. (b) Shows the same heterostructure after storage in vacuum, with the creation of bubbles in the interface between the flakes. (c) Shows the same heterostructure after the Ar/H_2 anneal specified in section 2.1.2.*

To select the best areas, i.e. those without air bubbles, an etching procedure was used to define the desired area of the heterostructure. An etching method using only Ar gas (as O_2 gas caused the $MoTe_2$ to oxidise and become unmoveable as a MoO_X compound) was used at flow rate of 10 sccm and 10 W power for 10 minutes. This procedure was able to etch 4 layers of $MoTe_2$. The etching allowed devices created such as those in Figure 2.3. After etching, contacts were fabricated as previously described. Images of individual flakes on the PDMS stamps and substrates which are turned into devices are shown in Figure 2.4.

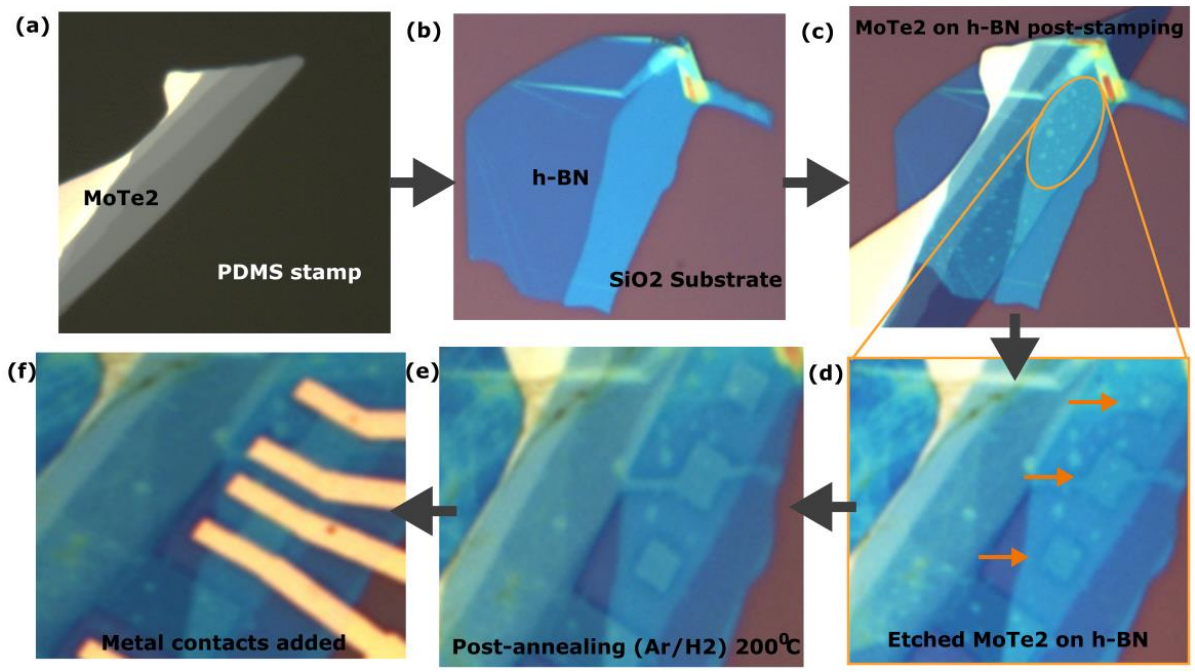

Figure 2.4: *Images of flakes used to create a heterostructure device of $MoTe_2$ on h-BN. (a) $MoTe_2$ flake on PDMS stamp. (b) h-BN on Si/SiO_2 substrate. (c) Heterostructure on the Si/SiO_2 substrate. Orange circle defines area of images (d) to (f). (d) Image of etched $MoTe_2$ on h-BN into small squares highlighted by orange arrows. (e) Heterostructure with noticeably fewer defects after annealing. (f) Heterostructure squares turned into devices by the lithography process.*

2.2. Identification of Few-Layer $MoTe_2$

When using 2D materials, providing information on the number of layers in the sample/device is important, so that any measured properties can be correlated, where appropriate, to layer thickness. The techniques used to determine the number of layers in, and the quality of, the $MoTe_2$ samples prepared in this thesis are: Raman spectroscopy, optical contrast, atomic force microscopy (AFM) and photoluminescence (PL).

2.2.1. Raman Spectroscopy

As already mentioned in Chapter 1, Raman spectroscopy is widely used as a tool to inspect two-dimensional materials, most famously graphene where Raman spectroscopy

can provide information about defects and the thickness of graphene.[112] In Raman spectroscopy, coherent light from a laser scatters off the material of interest, most commonly with no change in energy i.e. via Rayleigh scattering (elastic). A small fraction, around 1 in 10 million photons, can gain or lose energy in Stokes or anti-Stokes scattering (inelastic). This change in energy comes from a photon interacting with a phonon i.e. the molecular vibrations of the sample. The difference between the energy of the initial emitted photon from the laser and the photon returned via inelastic scattering provides information on the molecule. Recording the Stokes shift allows for the unveiling of the energy of the phonons, which can in turn be used to identify material compositions, phases and, in the case of 2D materials, the number of layers in the sample.

The Raman spectrum of $MoTe_2$ is well known,[62,64] with three main peaks, the $\mathbf{A_{1g}}$ (180 cm^{-1}), $\mathbf{E^1_{2g}}$ (230 cm^{-1}) and $\mathbf{B^1_{2g}}$(290 cm^{-1}) with peak positions in brackets attained using a 532 nm laser. Raman spectra in this thesis were recorded in the backscattering configuration, allowing for flakes on non-transparent substrates to be measured. A Horiba confocal microscope with a 100x Olympus objective lens (0.9 NA), CCD detector and a 532 nm laser were used to collect Raman spectra. A spectrometer grating of 2400 grooves mm^{-1}, with a slit aperture of 50 μm and hole aperture of 100 μm were used, providing a spectral resolution of ~1 cm^{-1}. The laser spot size for these measurements was 0.5 μm and a low power density of 0.02 mW/cm^2 was used to avoid any possible damage to samples. An acquisition time of 30 s was used to obtain enough signal to categorise the peaks. To calibrate the peak position, the Si peak was set as a reference, as this peak is present at 520.7 cm^{-1} with 532 nm incident light.

Exemplar Raman spectra for $MoTe_2$ flakes between 1 and 4 layers thickness are presented in Figure 2.5, where the peak ratio of $\mathbf{B^1_{2g}}$ and $\mathbf{E^1_{2g}}$ is also presented, a measure which can be used to identify the number of layers. This method of using peak ratios to identify flake thickness was highlighted by Yamamoto et al.[64] as already discussed in Section 1.4. As previously mentioned, identifying monolayer $MoTe_2$ is easy, despite it being only ~0.7 nm in thickness, due to the absence of the $\mathbf{B^1_{2g}}$ peak.

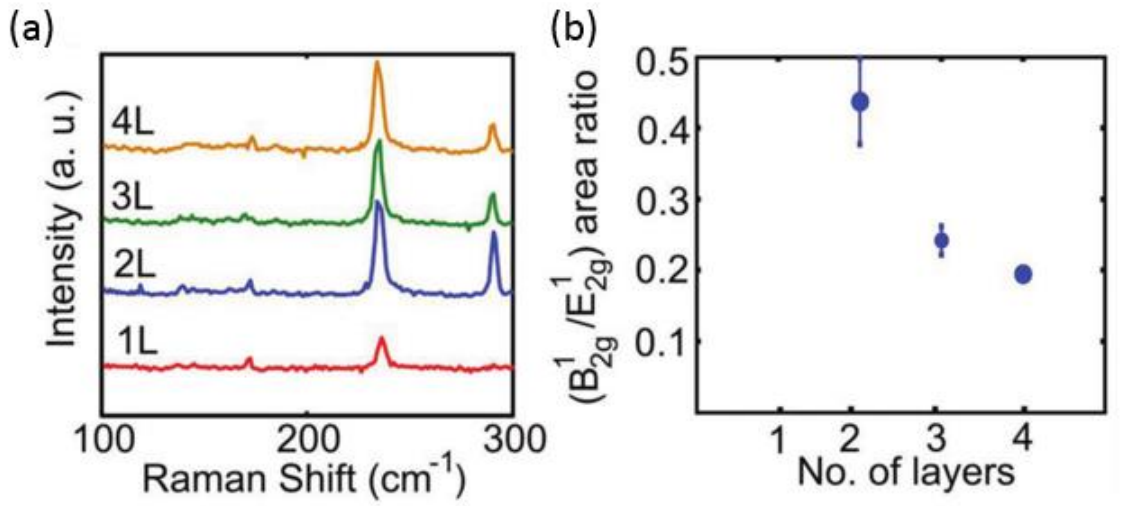

Figure 2.5: *(a) Exemplar Raman spectra for $MoTe_2$ flakes of 1 to 4 layer thickness showing the major peaks of $MoTe_2$. (b) Ratio of the $\boldsymbol{B^1_{2g}}$ and $\boldsymbol{E^1_{2g}}$ peaks, which can be used to identify the number of layers present.*

2.2.2. Raman Spectra of Oxidised $MoTe_2$

As $MoTe_2$ is known for oxidising in air, the spectra of deliberately oxidised $MoTe_2$ is presented in Figure 2.6. The flakes used for this figure are deliberately oxidised by leaving on a hotplate at 300 ^{0}C for one hour. Arrows in this figure are the Raman peaks for MoO_3 and stars refer to peaks in TeO_2.[113,114] Figure 2.6 also includes Raman spectra of a pristine $MoTe_2$ four-layer flake and a four-layer flake thinned via the photochemical layer-by-layer process explored in Chapter 7. A comparison of such spectra with those of the deliberately oxidised sample provides a useful method for determining if any oxidation has occurred for any particular sample (and in the two cases shown in Figure 2.6, it is clear that no oxidation has occurred).

Having proved that the $MoTe_2$ which is pristinely exfoliated is not oxidised, and knowing the Raman spectra of flakes having various number of layers, optical contrast measurements of flakes can then be used to provide a simpler and quicker way to determine sample thickness, as described in the following section.

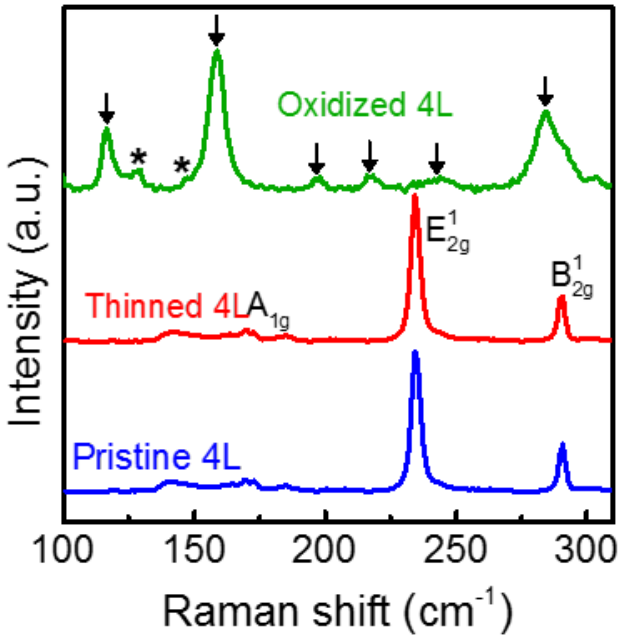

Figure 2.6: *Raman spectra of oxidised $MoTe_2$ against pristine and photochemically-thinned $MoTe_2$, showing the absences of oxidation in our pristine (and thinned) samples of $MoTe_2$.*

2.2.3. Optical Contrast Study

The optical contrast of 2D materials is known to change dramatically with thickness due to the optical cavity formed by the SiO_2 layer on top of the Si substrate and the 2D material itself.[115] In the work of this thesis a SiO_2 thickness of 300 nm was chosen to provide sufficient dielectric thickness for the back gate (used in electrical measurements) while also creating a strong optical contrast between $MoTe_2$ and the substrate. The optical contrast measurements were taken using a Nikon Eclipse LV150 optical microscope with a 100x objective lens and 0.9NA. A Nikon DS-Fi1 camera was used to capture images, at a resolution of 1280x960 pixels and with the light exposure tailored to obtain the best contrast.

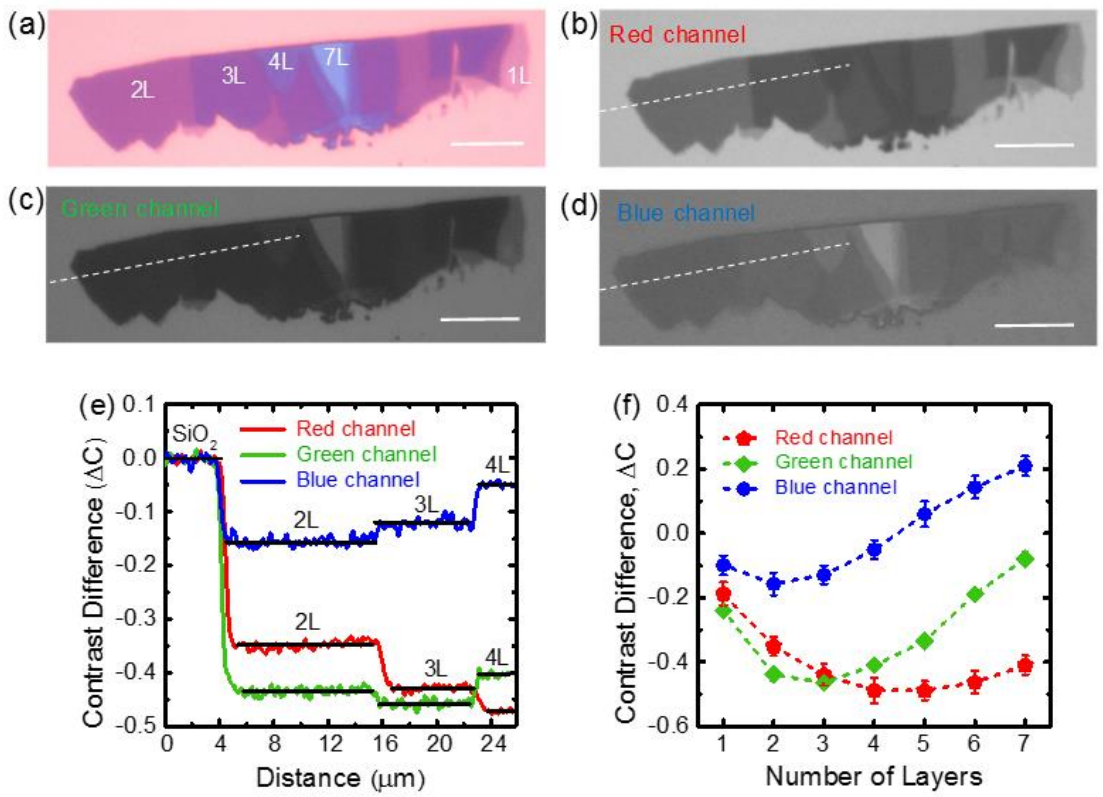

Figure 2.7: *(a) Shows the white light microscopy image of a multi-layered flake. (b), (c) and (d) show the red, green and blue light channels from the camera image (a) to show how different channels can be used to identify the flake thickness. (e) and (f) show the contrast difference first along the white dashed line, then as a function of layer number respectively. (The scale bar is 5 μm)*

In Figure 2.7, by way of an example, the optical contrast of a multi-layered $MoTe_2$ flake is shown under white light illumination (Figure 2.7(a)) and with all three colour channels (Figure 2.7(b)-(d)) (of the camera) in greyscale separated to show the changes in contrast for each channel (using ImageJ software). The optical contrast difference (**ΔC**) is also shown, defined as $\mathbf{\Delta C} = (\mathbf{C_{MoTe2}} - \mathbf{C_{sub}})/\mathbf{C_{sub}}$ where $\mathbf{C_{MoTe2}}$ and $\mathbf{C_{sub}}$ are the optical contrasts of the $MoTe_2$ and substrate respectively. In Figure 2.7(e), the contrast difference along a dashed white line provides **ΔC** between flakes, showing the ease of identifying different flake thicknesses of $MoTe_2$, even between single-layer differences. The full categorisation of the optical contrast is provided for flakes up to seven layers thick is provided in Figure 2.7(f).

2.2.4. Atomic Force Microscopy

Atomic Force Microscopy (AFM) obtains information of the surface topography of two dimensional materials by measuring the deflection of the AFM cantilever as the AFM tip is raster scanned over the material. AFM in this thesis is performed in a Bruker Innova AFM system using contact mode with standard Al coated Si cantilevers with spring constant of 40 N/m and tip radius of 8 nm. Atomic Force Microscopy was used in this thesis as an additional, independent method to measure flake thickness and to assess flake uniformity. Note however, that due to a layer of adsorbates present between SiO_2 and the flake,[8] obtaining accurate flake heights based on differences in height between the SiO_2 and the top of the $MoTe_2$ flake is not advised. AFM was also used to assess the surface roughness of flakes after various treatments, such as the layer-by-layer thinning process described in Chapter 7. AFM measurements of the same multi-layered flake shown in Figure 2.7 are given in Figure 2.8, to demonstrate the usefulness of this technique.

AFM was also used to identify poor quality transfers for heterostructures, successfully showing creases and adsorbates between the layers of some transfers. In Figure 2.9, for example, an optical image of $MoTe_2$ on some h-BN is shown with an AFM scan alongside. The AFM image highlights that this transfer is unsuitable for further study due to the large number of adsorbates between the layers. By completing the stamping procedure at slower speeds and cleaning flakes after exfoliation, the quality of such transfers improved, and this was visible in AFM and optical measurements (see Section 2.1.3).

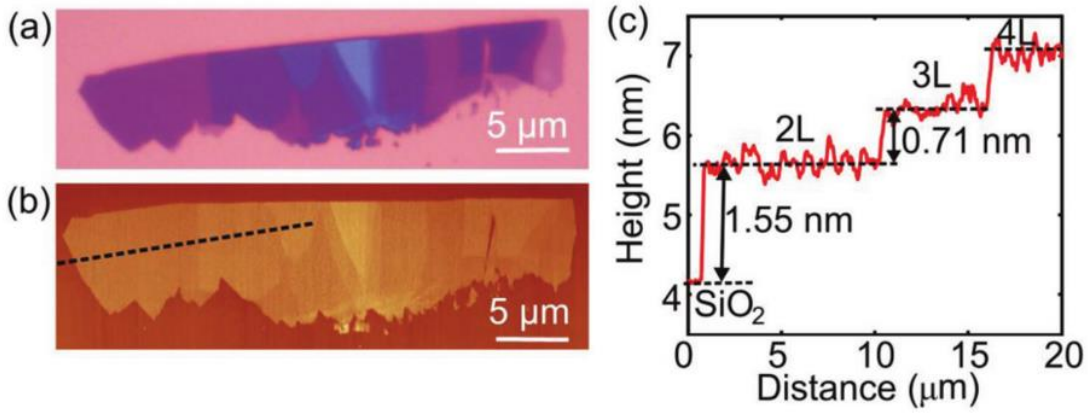

Figure 2.8: *AFM of a multi-layered flake, showing the interlayer separation of ~0.7 nm between a 2L and 3L flake.*

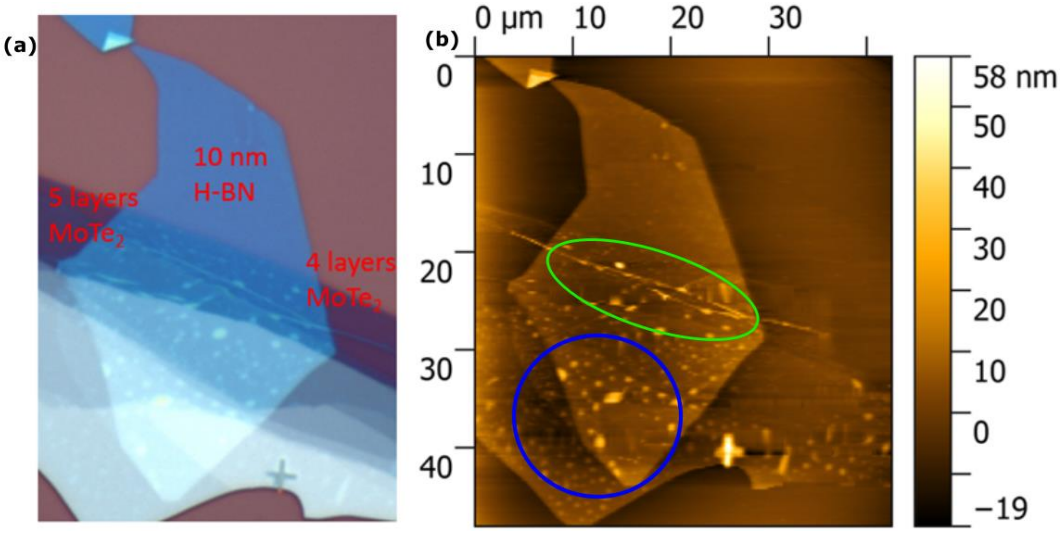

Figure 2.9: *(a) Optical Microscopy image of a heterostructure of $MoTe_2$ on top of h-BN. (b) AFM image showing the creasing of the h-BN during the transfer process in the centre of the image. Blue circle show bubbles also formed during the transfer, and show heights of <10 nm. Green ellipse show a crease in the $MoTe_2$ flake. AFM thus revealed that this transfer was unsuitable for device applications.*

2.2.5. Photoluminescence

Photoluminescence (PL) measurements in this thesis were taken at room temperature in a Horiba Jobin-Yvon LabRam HR Raman/PL spectrometer with an InGaAs detector having a spectral range capable of recording signals in the near infra-red. For photoluminescence, above band gap photons are absorbed by the $MoTe_2$ exciting charge carriers from the valence to conduction band, which then recombine to emit a photon with energy of the band gap. The band gaps of TMDCs are highly dependent upon the number of layers, so PL measurements can be used to determine layer thickness and the band gap of individual thicknesses of TMDCs.

The PL yield is larger for direct band gap materials (cf. indirect band gap materials), since only a photon is required to excite carriers. PL yields are lower for indirect band gap materials, which require changes in momentum through a phonon as well as the changes in energy due to the photon to excite carriers. The band gap in monolayer TMDCs is direct due to quantum confinement,[26] so PL yields for monolayer TMDCs are highest, with bi-layer yields being second highest, etc.

In Figure 2.10, by way of example, the PL measurements of a flake being thinned down from 5 layers to monolayer thickness are shown. The PL peak positions shown in this figure correlate with measurements in literature for room temperature PL measurements.[62]

The band gap of TMDCs becomes smaller with increasing thickness, so the peak PL intensity shifts to higher values as the thickness decreases towards the monolayer, as can be seen in Figure 2.10. It is also clear from the figure that the PL yield is higher for the thinner samples.

Measurements of PL are useful not only to provide information on thickness, but also on whether the phase of $MoTe_2$ is semiconducting or semi-metallic. Since the heat from a laser is known to be capable of irreversibly changing the phase of $MoTe_2$, the ability of PL measurements to differentiate between these two phases is useful.[27]

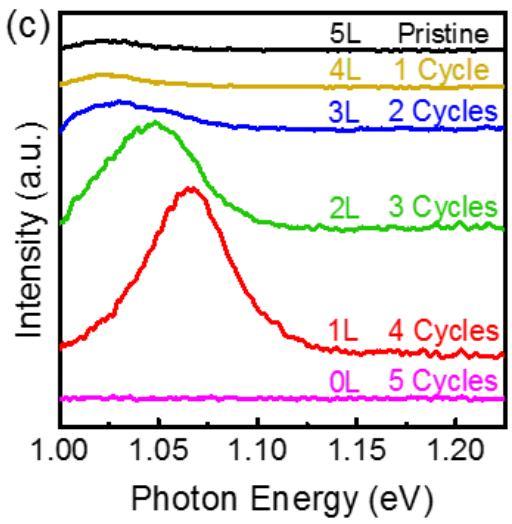

Figure 2.10: *PL measurements for $MoTe_2$ as a pristine 5 layer flake, thinned layer-by-layer to monolayer thickness. Finally a higher power density is used to remove the flake entirely from the substrate, with no PL signal subsequently evident.*

2.3. Electrical Measurements of $MoTe_2$ Devices

The two measurements used to categorise the electrical performance of FET devices fabricated using $MoTe_2$ are the output and transfer characteristics. Output characteristics tell us about the transistor, with a linear characteristic indicative of an Ohmic contact while non-linear characteristics about the presence of a Schottky barrier. Transfer characteristics are important as they define the switching properties of the FET. Parameters for assessing the quality of the FET include the subthreshold swing, mobility, ON/OFF ratio and hysteresis.

To perform these measurements, two terminal devices, fabricated as described in section 2.1.2, are fixed on a printed circuit board (PCB) with silver paint, with gold pads which can connect up all terminals. A schematic of the PCB is shown in Figure 2.11, where a large gold pad is used to apply the gate voltage and surrounding gold pads are connected to the source and drain terminals via thin gold wires. The PCB is used to connect to a switch box, where the individual pins of the PCB can be modulated separately.

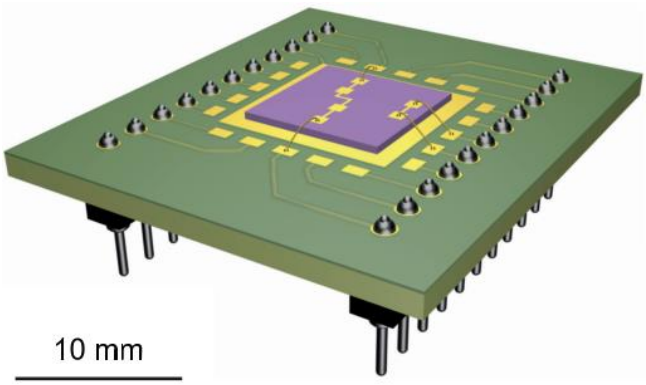

Figure 2.11: *PCB used to measure $MoTe_2$ on Si/SiO_2. Large bottom Au pad is used to apply the gate bias. Gold pads around the central gold pad are used to connect up the source and drain terminals. Figure taken from De Sanctis et al.*[116]

DC electrical measurements were performed in this thesis with a calibrated Xitron 2000 (for the application of the drain-source voltage, V_{ds}), a Keithley 2400 Sourcemeter (for the applied back gate voltage), an Agilent 34410A meter (to record the drain-source current, I_{ds}) and a DL model 1211 current amplifier to boost the signal read by the Agilent 34410A. Output and transfer characteristics were measured here using DC measurements only.

$MoTe_2$ devices were mounted on specially designed printed circuit boards (PCBs) for ease of mounting into optical and electronic measurement setups. PCBs have a ground plane which the device is attached to, and Au mounts for individual contacts. Up to 10 pairs of contacts could be created on a single device using the PCB boards, with a wire-bonder connecting the Au pads of the PCB to Cr/Au squares deposited on the surface of the Si/SiO_2.

2.3.1. FET Output Characteristics

The FET output characteristic, which plots I_{ds} versus V_{ds}, can be used to find the resistance of the device (including the contact resistances), which is usually taken from the steepest slope to obtain a total device resistance as defined by Ohms law. To obtain the output characteristic, the drain-source voltage is here set to a particular value, then swept at a rate of 0.1 V/s. Output characteristics for different values of back gate voltage are usually obtained, to show any impact of back gate modulation. A typical output characteristic

obtained for the $MoTe_2$ FET devices of this thesis is shown in Figure 2.12, for various values of back gate voltage. It can be seen that the output characteristic of Figure 2.12 is non-linear, indicating the presence of a Schottky Barrier, well documented in $MoTe_2$ devices.[84,91]

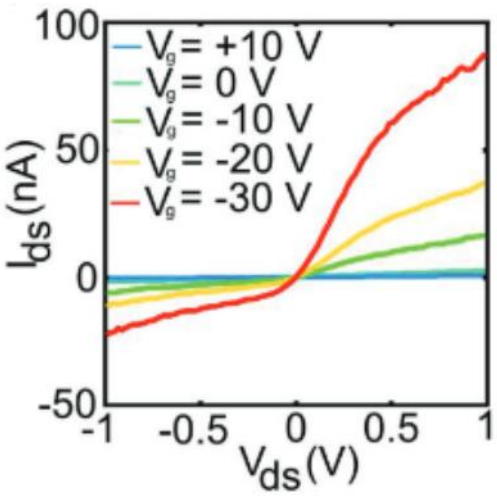

Figure 2.12: *Typical output characteristic for $MoTe_2$ FET devices fabricated in this thesis, here with changes in V_g from +10 to -30 V. This particular device enters into the ON state at V_g ~ -10 V, indicating p-type conduction/doping in this particular case.*

Resistances recorded from the output characteristics of the whole range of $MoTe_2$ FETs fabricated in this thesis varied by 5 orders of magnitude, from 10^5 to 10^{10} Ω, and i some cases devices showed linear behaviour. Devices with high resistance had smaller field effect mobilities, showing the importance of good contact between the metal contact/$MoTe_2$ interfaces to improve the transistor behaviour. Further details and discussions are given in the Appendices, in Section 2.4.

2.3.2. FET Transfer Characteristics

The transfer characteristic of an FET is revealed by measuring the drain-source current as a function of the gate voltage, for fixed values of the drain-source voltage. Transfer characteristics are useful to extract values for the field effect mobility by taking the gradient of the steepest slope in the ON state $\left(\frac{\Delta I_{ds}}{\Delta V_g}\right)$, to extract the threshold voltage (obtained by drawing a line from the linear part of the characteristic to the voltage axis)

and to find out the majority charge carrier, i.e. if $MoTe_2$ enters the ON state at negative gate bias, then holes are responsible for conduction.

The gate voltage sweep rate for the transfer characteristic was, in the work of this thesis, kept at 1 V/s for a compromise between the number of data points in the sweep and speed of measurement. Sweeps started in the OFF state of the device to ensure the highest values for mobility were recorded, as devices left in the ON state will have their transient current drop quickly, as discussed in the Chapter 4.

A typical transfer characteristic from a $MoTe_2$ flake is shown in Figure 2.13. Here the device shows p-type conduction as the FET turns on when $\mathbf{V_g}$ is negative, the gradient highlighted in the red ellipse provides the field effect mobility and the dashed red line from the linear ON state provides a value for the threshold voltage. For this measurement, the up sweep is used, however sizeable hysteresis is shown in these devices, and will be discussed in Chapter 4. Hysteresis in air is large for $MoTe_2$ devices due to how readily $MoTe_2$ reacts with O_2 and water in ambient conditions, creating many available trap states in the material.[72,86] Vacuum measurements are therefore recommended to reduce or eliminate such effects of O_2 and water contamination, with such measurements described in the next section.

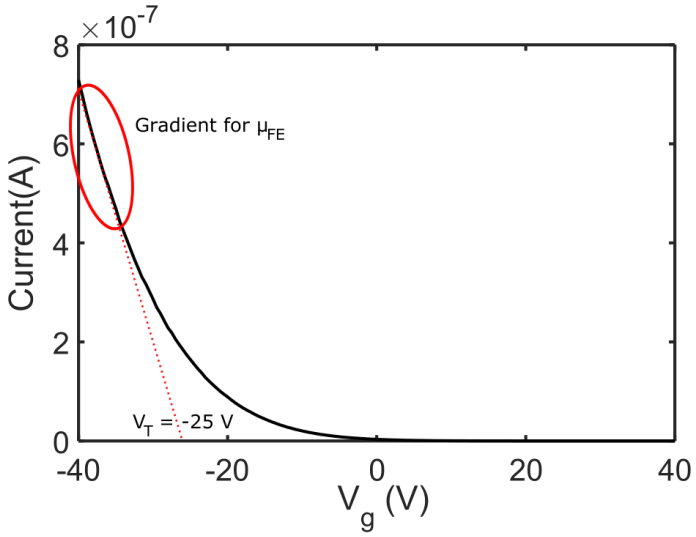

Figure 2.13: *FET transfer characteristic taken in ambient conditions of a four-layer $MoTe_2$ flake.*

2.3.3. Vacuum Measurement of Electrical Properties

When looking at the performance at high vacuum, the hysteresis often seen in the FET transfer characteristic is much reduced, which will be discussed in Chapter 4. This is due to the removal of water molecules from the surface of the $MoTe_2$ due to the high vacuum measurement condition. In the transistors used in this study, the mobility in vacuum conditions on average increased and hysteresis between the up and down sweeps was greatly reduced. While on average mobility was found to increase, the impact of vacuum on electrical measurements has been shown to affect the doping of TMDCs.[65] The vacuum system for electronic measurements uses a roughing and turbo pump to reach high vacuum of 10^{-5} Torr. A full categorization of the transistors used in this thesis is available in Section 2.4.

2.3.4. Figures of Merit for Electrical Performance

From the output characteristic, the largest linear slope is used to extract the total device resistance which is a key electrical figure of merit. From the transfer characteristic, the field effect mobility (μ_{FE}), ON/OFF ratio and subthreshold swing tell us the characteristics of the transistor. To obtain μ_{FE}, equation (2.1) is used:

$$\mu_{FE} = \frac{L}{W} C_{OX} \frac{\Delta I_{ds}}{\Delta V_g} V_{ds} \quad (2.1)$$

Where **L** is length of the channel, **W** is the width of the channel, C_{OX} is the capacitance of the oxide layer, $\frac{\Delta I_{ds}}{\Delta V_g}$ is the transconductance (taken as the linear slope of the gate sweep in the ON state) and V_{ds} is the drain-source bias. A high mobility means the device can typically be operated at lower operational voltages, which will reduce the energy required for continued operation.

The subthreshold swing (SS) is the ΔV_G/ (I_{ds} per decade(**/Dec**)), which has a theoretical limit of ~60 mV/Dec due to thermionic emission.[117] The lowest value of SS in this thesis was found to be 500 mV/Dec, due in part to the smallest step size for gate sweeps being set at 0.5 V; measurements with higher resolution may improve the SS values.

The ON/OFF ratio is defined as the orders of magnitude between the largest and smallest values of $\mathbf{I_{ds}}$ in the ON and OFF states, with a maximum of 10^6 from the devices in this thesis, with this value becoming larger under lower $\mathbf{V_{ds}}$ values.

2.4. Overview of Electrical Performance of FETs Fabricated in this Thesis

In total 78 working FETs , separated into 16 batches, were fabricated during the work of this thesis. In this section the electrical properties of these devices are summarised, showing the importance of flake thickness and device resistance for obtaining the highest mobility devices. Since silicon-based electronics can have mobilities of ~1000 cm^2/Vs, increasing the mobility of 2D materials is crucial to their wide spread commercial usage. The highest recorded mobility of $MoTe_2$ in this study is 42 cm^2/Vs. The mobility from transfer characteristics are shown in accordance to the resistance from the output characteristic, and the thickness of flakes, to observe correlation for the best thicknesses of flakes for further study, and the importance of reducing Schottky Barriers for strong electrical performance.

2.4.1. Total Device Resistance vs. Mobility

The importance of the device resistance against mobility seems clear, a device with higher resistance should have a lower mobility. This statement is tested in Figure 2.14 where the mobility and device resistance are plotted, with the legend showing the batch in which the $MoTe_2$ device was created and the measurement conditions. Overall, transfer characteristic derived mobilities ranged from ~10^{-4} to ~40 cm^2/Vs. The lowest recorded mobility, at 1.9×10^{-4} cm^2/Vs, belongs to a monolayer flake which in literature and from our own findings generally made poor transistors.[74] Our highest mobility of 42 cm^2/Vs is the highest recorded mobility of pristine $MoTe_2$, without encapsulation by h-BN or other methods, to date. The higher mobility devices had resistances lower than ~10^8 Ω, showing the output characteristic had some effect on the transfer characteristic of devices, as seen in Figure 2.14. It is also clear that good contacts are important for the creation of good FETs. Devices in this thesis were made with Cr/Au (5/50 nm) contacts, whereas many devices in literature use just Au contacts, which can lead to the creation of

a smaller tunnel barrier (hence lower device resistance) at the $MoTe_2$/metal contact interface.

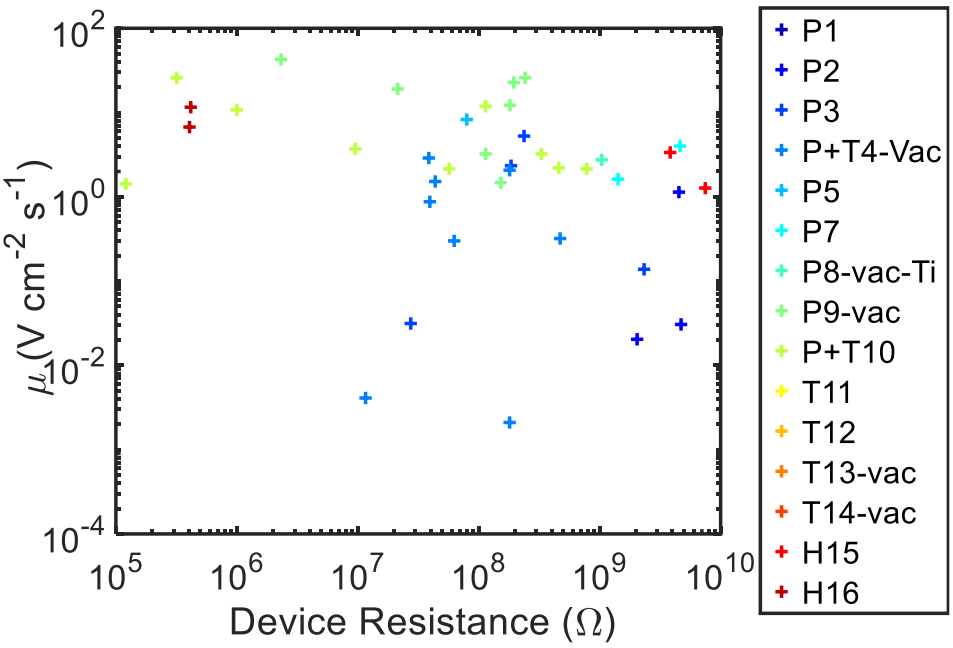

Figure 2.14: *Total device resistance against two-terminal mobility for all $MoTe_2$ devices, separated by their batches. Legend: P, pristine, T, thinned, Ti refers to Ti contacts, Vac, vacuum measurement and, H, heterostructure with h-BN. Batches are numbered 1 to 16.*

2.4.2. Flake Thickness vs. Mobility

The impact of the thickness of flakes was investigated throughout our measurements, finding flakes around 4 to 8 layers having the highest mobilities, in agreement with the literature on $MoTe_2$ FETs.[89]

Devices fabricated from pristine flakes in the early part of the work of this thesis suffered from poor mobilities. We believe the main reason for this is the photoresist used during fabrication, which upon replacement from batch 5 onwards led to an improvement in recorded mobilities. Device performance changed nominally from batch to batch, with thicker flakes performing more consistently as shown in Figure 2.15. With such great disparity in mobility values in literature and own work, more research is required to

understand the effect fabrication procedures to obtain the best mobilities for $MoTe_2$ FETs.

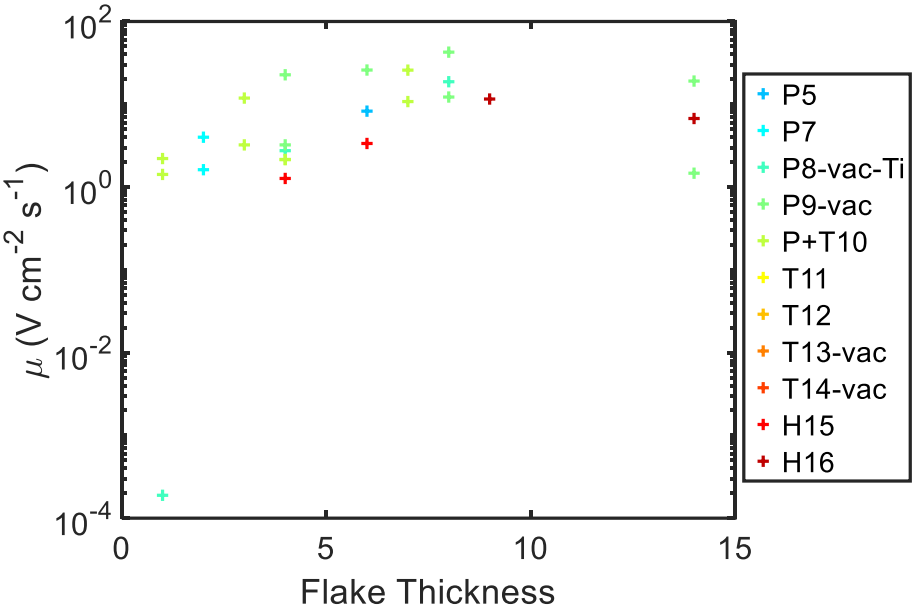

Figure 2.15: *Flake thickness vs. mobility of FETs, with flakes between 4 and 8 layers showing better electrical properties overall. Legend is the same as in* ***Error! Reference source not found.***

Nearly all devices showed strong p-type doping which is attributed to exposure to air.[65] Some devices showed ambipolarity, with a weaker n-type doping, these flakes were more than 6 layers thick (thinner samples showed only p-type conduction in this study). The threshold voltage of a majority of our devices was around 10 to 30 $\mathbf{V_g}$, meaning devices are in the ON state without an applied gate, running in depletion-mode. The largest recorded ON/OFF ratios were ~10^6, from the 10 pA range (noise floor of our measurements) to 10 μA in the ON state. Current drift made it difficult to record consistently good subthreshold swing measurements, however we have recorded 500 mV subthreshold swings (of which the thermal limit is 60 mV/decade)[179], limited by the measurement resolution for the gate voltage.

2.5. Optoelectronic Measurements of $MoTe_2$ FETs

The measurement system used for photocurrent measurements, and the figures of merit used to quantify the optoelectronic performance, of $MoTe_2$ FET devices will now be

described. As for the purely electrical measurements described in section 1.3 above, output and transfer characteristics (this time under the influence of laser illumination) were again measured using DC techniques. For photocurrent mapping and photoresponse time measurements, AC measurements were performed (to help prevent any persistence photocurrent effects) using an Ametek 7270 DSP lock-in amplifier and frequency generator. A DL Model 1211 current amplifier was used for AC current measurement/amplification, this amplifier has a response time of ~2 μs according to the specifications. As shown from measurements of pulsing the gate electrode through a 1 GΩ resistor in Figure 2.16. The time constant from the pulse is < 2 μs in accordance with the specifications, making it suitable for frequency measurements in the kHz range. For photoresponse time measurements an oscilloscope trace of the photocurrent and modulated laser are superimposed to extract the response (rise and fall) time.

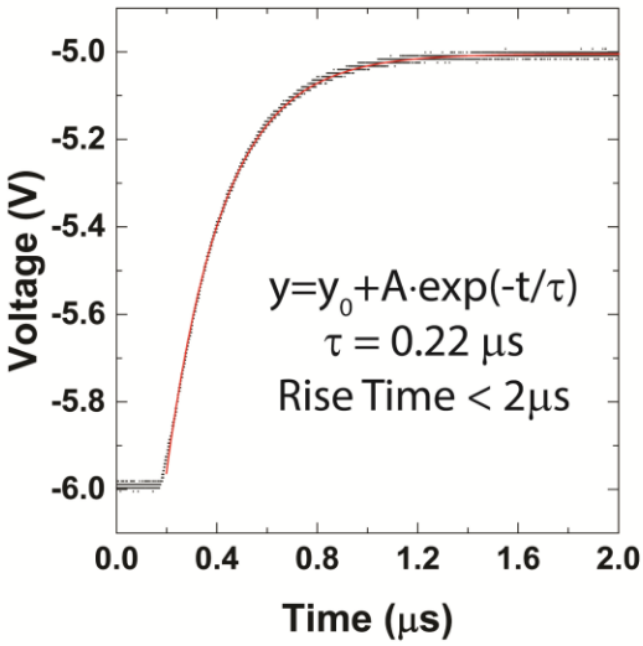

Figure 2.16: Pulsed gate voltage through a 1 GΩ resistor to show the response time of the system as < 2 μs.

2.5.1. Optoelectronic Measurement System

The optoelectronic measurement system used in this thesis is a custom-built optoelectronic setup with a Faraday cage to ensure low noise measurements. The full

details of this system have been reported by Jones et al.[116] The basic use of the system will be covered in this thesis as not all functionality of the system was used for measurements reported here – only electrical and optoelectronic measurements were completed in the setup.

A basic schematic for the system with some functionality of the real system removed is shown in Figure 2.17. The caption for Figure 2.17 details the key operation of the optoelectronic system through labelling.

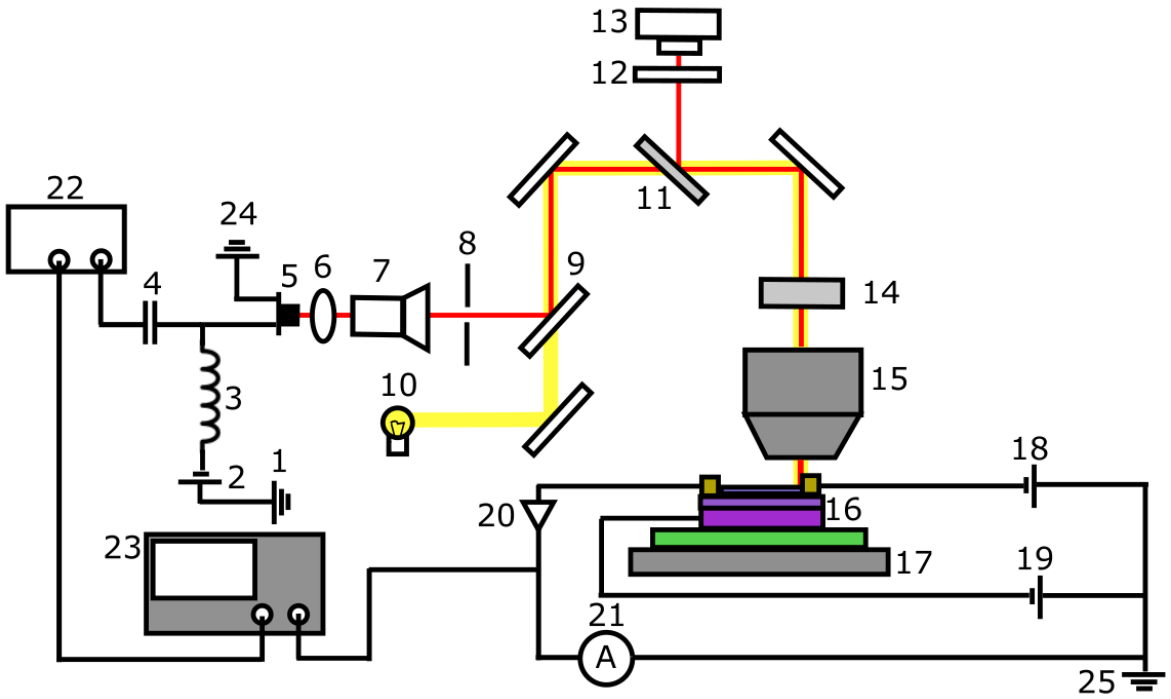

Figure 2.17: *Schematic diagram of photocurrent setup: (1) ground, (2) DC bias, (3) & (4) bias tee, (5) laser diode (685 nm), (6) converging lens, (7) beam expander, (8) pin hole, (9) mirror, (10) white light source, (11) beam splitter, (12) 700 nm long pass filter, (13) camera, (14) ND filter, (15) x50 objective lens, (16) $MoTe_2$ device, (17) xy stage, (18) DC V_{ds} bias, (19) DC V_g bias, (20) pre-amplifier, (21) ammeter, (22) function generator, (23) oscilloscope, (24) & (25) ground.*

In this system four lasers are available at wavelengths of 473, 514, 561 and 685 nm. The system has a moveable XYZ stage which provides the ability to perform scanning photocurrent microscopy (SPCM) with 0.1 μm step sizes. Step sizes of 0.5 μm were however used in this work, as a compromise between the time taken for a single photocurrent map and appropriate resolution for examining the origin of fast

photocurrent. The smallest diameter of the laser is <0.9 μm when using a 50x Olympus lens. All SPCM was performed with the AC system as issues with persistent photocurrent during a DC scan may skew results for photocurrent mapping. To ensure vibrations would not affect the position of the laser on the sample, the system is built upon an isolated optic table.

2.5.2. Optoelectronic Figures of Merit

To determine the quality of a photodetector, some common figures of merit are used. These metrics include the photoresponsivity (A/W), external quantum efficiency (%), or **EQE**, and the photoresponse time (s).

The photoresponsivity simply determines the photocurrent created from the input laser power and is commonly used as a metric to highlight the effectiveness of a photodetector. To obtain the photoresponsivity (A/W), the photocurrent is divided by the optical power of the laser for the measurement: Photoresponsivity **= I_{ph}/P** where **I_{ph}** is the photocurrent and **P** is the optical power of the microscope.

The EQE is used to gauge how effective a photodetector is at converting photons directly into free charge carriers in the FET. To obtain the EQE, the photocurrent is divided by the fundamental charge, **q**, and then this is divided by the photon flux: **EQE = $(I_{ph}/q)/\phi$** where **q** is the fundamental charge and **ϕ** is the photon flux. This is usually given as a percentage and is used to determine the efficiency between how many photons are required to excite a single charge carrier. If this value is above 100% then some gain effects must be present in the photodetector.

The response time is used to gauge the speed of the photodetector. Photocurrent response times were extracted from an oscilloscope trace of the photocurrent response when excited by a (square wave) modulated laser. Measuring response time is done by two main methods in the literature, either by a 3 dB (≈0.707) loss/gain or 90/10% cut-off of the signal.[118]

3. Optoelectronic Properties of Few-Layer $MoTe_2$

3.1. Introduction

Optoelectronics are used in many facets of technology, from laser diodes to light-emitting diodes (LEDs), sensors, photodetection, imaging and optical fibre communications. With the arrival of many two-dimensional materials, a full characterisation of the optoelectronic properties of these newly emerging materials is required to determine their possible use in the future. Despite $MoTe_2$ having a near infra-red direct band gap, it is rarely investigated for its optoelectronic properties.

In this chapter, four-layer flakes of $MoTe_2$ were chosen for optoelectronic measurements, due to their strong electronic properties while still showing strong light-matter interaction. Measurements were conducted with a 685 nm laser to extract the photoresponsivity and photoresponse time for the four-layered $MoTe_2$ FET-based photodetectors Two main mechanisms were found to dominate the optoelectronic response at different response speeds: band-bending at the $MoTe_2$/metal electrode interface which is a fast interaction where the height of the Schottky Barrier is changed, and the slower photogating effect which is responsible for changes in the threshold voltage ($\mathbf{V_T}$), and is found to lead to large photoresponsivity values under continuous illumination.

Attempts to improve the optoelectronic performance (particularly the photoresponse speed) by encapsulating $MoTe_2$ with h-BN were also performed, with a view to isolating $MoTe_2$ from adsorbates. However, additional work will be required using h-BN for encapsulation to extract even better optoelectronic properties for $MoTe_2$ and other TMDCs.

3.2. Optoelectronic Measurements with Continuous Illumination

Optoelectronic Direct Current (DC) measurements were performed to understand the different photocurrent mechanisms in mechanically exfoliated (four-layer) $MoTe_2$ on

Si/SiO_2 substrates in an FET configuration. All measurements in this chapter are conducted with a 685 nm red laser having an energy, at 1.8 eV, lying above the 1.0 eV band gap of four-layer $MoTe_2$. A schematic for the FET used in this experiment is provided in Figure 3.1, along with images of the four-layer flake used for a majority of the results in this chapter. DC measurements carried out include the output characteristic and transfer characteristic, which are then used to determine the photocurrent mechanisms for $MoTe_2$ under constant illumination. For these measurements, the entire channel of the FET is illuminated by the laser (by defocussing the laser spot until full coverage of the device channel and overlap of the metal contact/$MoTe_2$ interface was obtained), since the mechanisms for photocurrent generation under constant illumination may arise from the generation of excited charge carriers in the bulk of the $MoTe_2$ channel and/or at the $MoTe_2$/metal electrode interfaces.

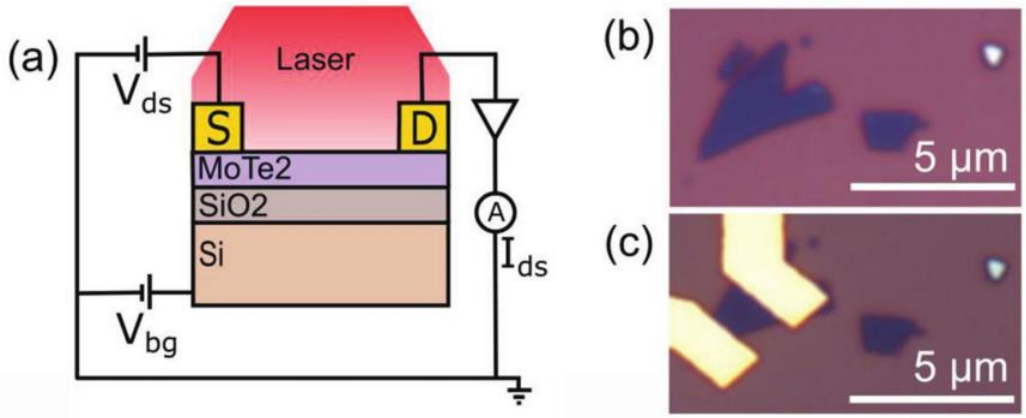

Figure 3.1: *(a) Schematic of the FET under red (685 nm) laser light. V_{ds} is applied to the source electrode, a current pre-amplifier and multi-meter collect I_{ds}. V_g is applied to the Si back gate for transfer characteristics. Laser is shown over the $MoTe_2$ channel and overlap between the $MoTe_2$/metal interface. (b) Four-layer flake used for the measurements in this chapter. (c) Four-layer flake with metal contacts.*

3.2.1. Output Characteristics

Output characteristics were taken first in dark, then with the illuminating laser power increased over the range from 47 kW/m² to 1.2 MW/m². The output characteristic for

$MoTe_2$ shows a clear increase in current from the dark measurement to the illuminated measurement, as shown in Figure 3.2. The resulting photoresponsivity is 5 mA/W under the 47 kW/m^2 illumination, reducing to 0.5 mA/W under the higher power density of 1.2 MW/m^2. The external quantum efficiency (EQE) is 0.9 % under the low power illumination, showing that there are no gain effects under such circumstances.

The results of Figure 3.2 indicate increased conduction via the creation of photo-excited charge carriers by the photovoltaic effect. The mechanism is elucidated by scanning photocurrent microscopy (SPCM) later in this chapter.

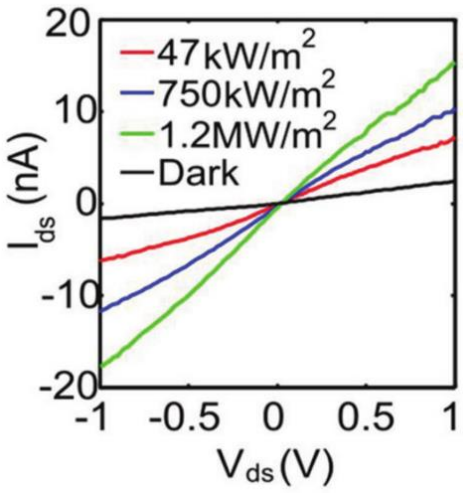

Figure 3.2: *Output characteristics for various illumination power densities using a 685 nm incident laser.*

3.2.2. Transfer Characteristics

Transfer characteristics were performed under illumination to observe photocurrent generation for $MoTe_2$ in the ON state of the FET. The 685 nm laser massively increased the photocurrent for the device in the ON state, generating photoresponsivity and EQE values three orders of magnitude greater (compared to results in Section 3.2.1). A typical transfer characteristic is shown in Figure 3.3 for the four-layer $MoTe_2$ flake. A dark measurement (black line) is performed first, followed by another scan with a 400 nW illumination, which equates to a power density of 20 kW/m^2. A lower power density (20 kW/m^2) is used for the transfer characteristic than the output characteristic (47 kW/m^2)

as the photoresponsivity is significantly greater when less photons are used to induce the photocurrent.[50]

The transfer characteristic shown in Figure 3.3 yields a field effect mobility of μ_{FE} = 2.04 cm^2/Vs for the up sweep (in dark conditions). Under 400 nW illumination, the mobility increases slightly to 2.20 cm^2/Vs due to the aforementioned change in the Fermi level, which reduces the Schottky barrier height (see Section 3.4.2). This mechanism will be addressed in section 3.4.2 that discusses scanning photocurrent microscopy results. However, the increase in mobility is not the reason for the drastic increase in current under illumination in the ON state. More important than the increase in mobility is the change in threshold voltage, V_T, which determines the V_g value where the device enters the ON state. In the dark, V_T for the device of Figure 3.1(c) is ~ -30 V, but this visibly changes under illumination to ~ -22 V, leading to a change in ~ -8 V for V_T. Thus, since the device is entering the ON state earlier in the voltage sweep, illumination generates a maximum photocurrent of ~1.5 μA at V_g = -40 V.

The maximum photoresponsivity in the results of Figure 3.3 is 6 A/W, recorded at V_g = -40 V; this is 12 times greater than the photoresponsivity seen during the measurement of the output characteristic. An EQE of 679% is achieved at V_g = -40 V, compared with < 1% when measuring the output characteristic, thus showing that there is very considerable gain occurring for the results of Figure 3.3. This gain arises due to the changing of V_T by illumination which causes carriers to tunnel through the Schottky barrier more efficiently at metal/semiconductor interface. This mechanism is called photogating and will be discussed in more detail in the following section. This effect is only observed under constant illumination and is therefore a slow photocurrent mechanism.

The measured photoresponsivity strongly depends upon V_g, as also shown in Figure 3.3. The photocurrent drops by three orders of magnitude between the ON and OFF states in the transfer characteristic. This is also evident in Figure 3.4, which presents the transfer characteristic with current in a logarithmic scale and emphasises the differences in the ON and OFF states with and without illumination. The FET under illumination has greater conductivity in the OFF state compared to the dark measurement by two orders of magnitude, due to the Schottky barrier reduction from change in the Fermi level. Under

illumination the ON/OFF ratio of the FET reduces from 10^4 to 10^2 from this generated photocurrent by the previously mentioned Schottky barrier reduction.

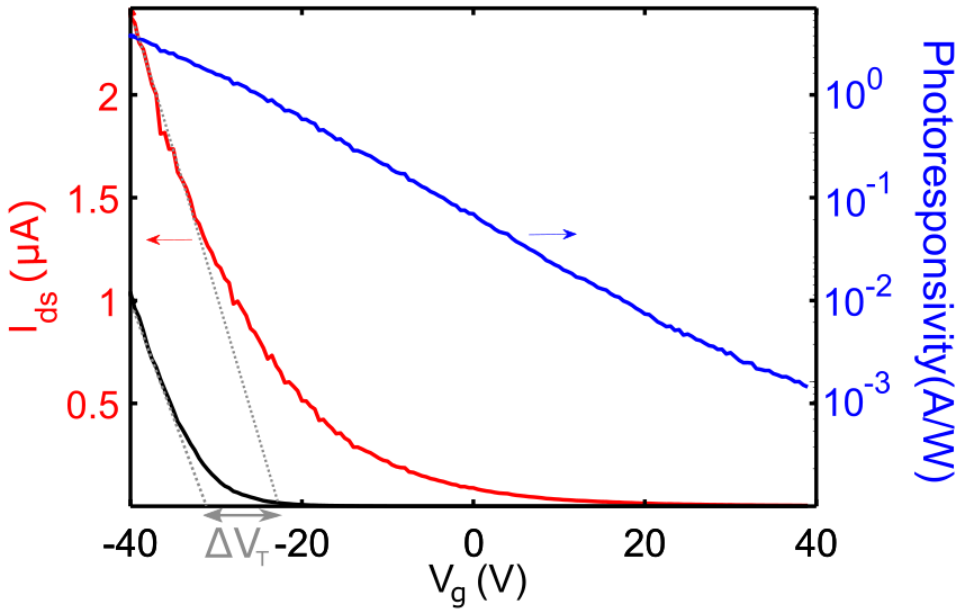

Figure 3.3: *The transfer characteristic of a four-layer $MoTe_2$ FET. A -8 V change in V_T is responsible for the large photocurrent produced by a 685 nm laser at 400 nW illumination power. The black line shows the dark measurement while red shows the illuminated measurement. On the right-hand-side y-axis, the photoresponsivity is plotted as a function of V_g.*

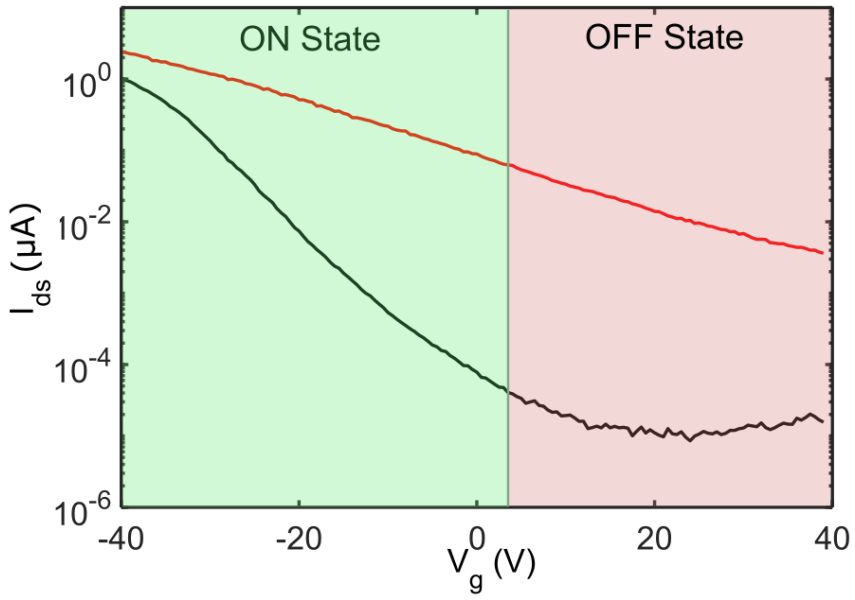

Figure 3.4: *Log-scale I_{ds} from the transfer characteristic of Figure 3.3, showing the change in conductivity between ON and OFF state for dark and illuminated measurements of $MoTe_2$ FETs. OFF state defined as when the dark current (black line) is <0.1 nA.*

3.3. Photocurrent Mechanisms under DC Conditions

Photocurrent mechanisms are a topic of much discussion in the field of optoelectronics, with power dependence,[119] photocurrent mapping,[120] gated measurements[104] and time dependence measurements[104] all being used to define and explain different photoconduction methods. Known photocurrent mechanisms operating in TMDCs include the photoconductive (photogating)[101,103,121], photothermoelectric (PTE)[119,120,122,123] and photovoltaic (PV)[69,104,123,124] effects. Disentangling these contributions is challenging, as they can each dominate on different time scales. However, the PTE effect will not be discussed here, as this is an effect that is only at zero bias and is small magnitude compared to other photocurrent mechanisms. All our measurements showing high photoresponsivity are taken with an applied source-drain bias.

For continuous illumination measurements with the $MoTe_2$ FETs, there are two main photocurrent mechanisms under applied bias. These mechanisms are facilitated by the photovoltaic effect which will be described in the next section. The photogating effect

which, as already mentioned, causes a shift in V_T in the transfer characteristics of $MoTe_2$ will then be discussed. To complete the discussion of photocurrent effects in the $MoTe_2$ FETs examined here, the effects of the changing of the Schottky barrier through band bending at $MoTe_2$/metal contact interface is discussed in Section 3.4.2.

3.3.1. The Photovoltaic Effect

The photovoltaic effect arises from the absorption of above-bandgap photons generating an electron-hole pair. An in-built electric field from a p-n junction or applied bias voltage manipulates the direction of flow of the generated electron-hole pair, thus creating a photocurrent. As the band gap of $MoTe_2$ is ~1.0 eV and the photon energy is 1.8 eV for the 685 nm laser, the energy of the photon is absorbed as it can provide enough energy to a charge carrier and promote it from the valence to the conduction band. Any remaining energy from the absorption process is converted into kinetic or thermal energy. The additional energy can increase the photocurrent even further by thermally exciting more charge carriers into the conduction band. Too much additional energy can cause a recombination of carriers, which then emit photons through mid-gap states. A pictorial description for the photovoltaic effect is presented from Sze et al.[94] in Figure 3.5.

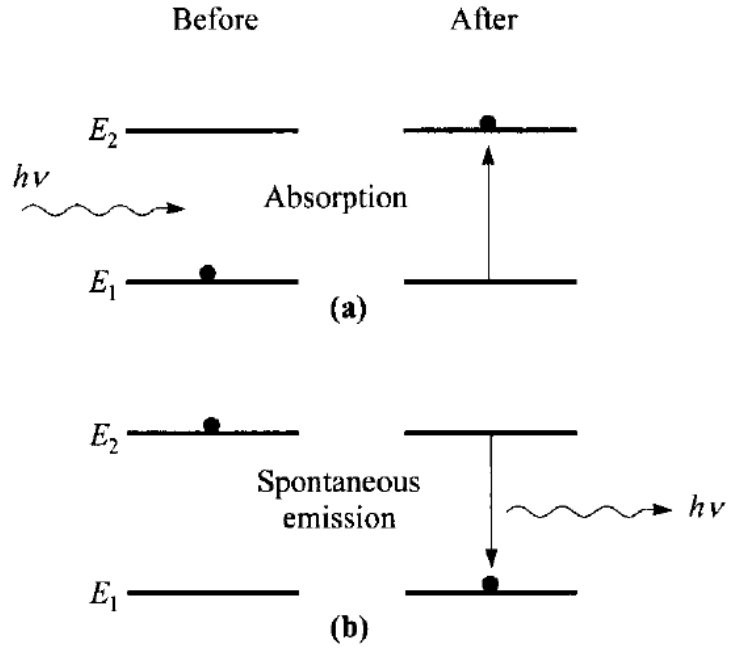

Figure 3.5: *Absorption and emission events in semiconductors. (a) Absorbing a photon promotes an electron from the valence (E_1) to the conduction (E_2) band, creating an electron-hole pair. (b) The reverse process is emission. Reproduced from Sze, Semiconductor Physics.*[94]

3.3.2. Photogating Effect

Photogating is a very important factor in the operation of TMDC photodetector devices.[101,104] Photogating is common in low-dimensional materials and high surface area semiconductors, and is often used to describe many different photoconductive effects as summarised by the review article on photogating by Fang and Hu.[121] Generally, photogating mechanisms involve the trapping, in mid-gap states, of excited carriers generated by the photovoltaic effect, thus creating an additional gating effect for the transistor. The trapping of charge carriers in mid-gap states is a slow photocurrent process, and is only observed under continuous illumination.

In p-doped $MoTe_2$, photogating is observed due to photogenerated electrons becoming trapped in mid-gap states.[104] Trapped electrons act as a local gate voltage which allows

for greater hole conductivity. This effectively modulates the gate sweep voltage causing the change in V_T as the FET enters the ON state at a new, lower V_g value.

The photogating effect for n-type conduction is illustrated from Huang et al.[101] in Figure 3.6, where mid-gap states trap holes instead of electrons, causing greater electron conduction.

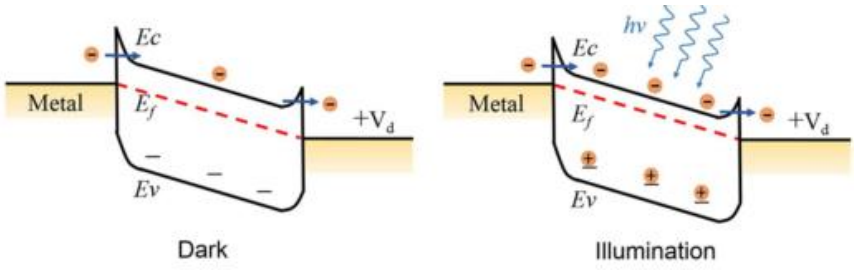

Figure 3.6: *Photogating effect for $MoTe_2$ FETs. In dark conditions, the FET behaves as normal, with the majority charge carrier creating conduction during operation. Under illumination, holes are trapped in mid-gap trap states which due to the large population of trap states present in $MoTe_2$ causes a sizeable shift in the V_T, creating a large photocurrent in the on state of the FET. Image reproduced from Huang et al.*[101]

3.4. Frequency Modulated Illumination in Photocurrent Measurements

To further understand the potential of $MoTe_2$ as a photodetector with a quick response time, modulated laser measurements were used to identify photocurrent mechanisms via power dependence measurements and photocurrent mapping. The speed of the photocurrent response is also acquired through modulating the laser, and extracting the DC current generated via matching the modulated laser frequency to a lock-in amplifier.

3.4.1. Power Dependence of Photocurrent

The power dependence (of the photocurrent) spanning over 5 orders of magnitude of illuminating light power was examined, again using the 685 nm laser, and the results are shown in Figure 3.7. A linear fit between power and photocurrent was found, having a

slope of 0.92 ± 0.04 Note that a slope of 1 is generally taken to indicate a photocurrent generated primarily by photovoltaic effects (see for example the work of Patil et al.[125] or Zhang et al.[119], where a derivation starting with the model for photodetection in the Physics of Semiconductor Devices by Sze[94] is used) In the results of Figure 3.7 the slope is very close to unity, with the fit being slightly below unity due to recombination of photo-excited carriers, potentially due to trap states.

A power/photocurrent dependence of ~0.67 is generally regarded to show that the photothermoelectric effect (PTE) is dominant (as also described by Patil et al.[125] and Zhang et al.[119] The derivation is described by Patil et al, and uses the Mott formula to find the power dependence relationship.). Since the results of Figure 3.7 show a power dependence much closer to 1 than 0.67, it can be concluded that PTE contributes either no photocurrent or an insignificant photocurrent in the four-layer $MoTe_2$ device.

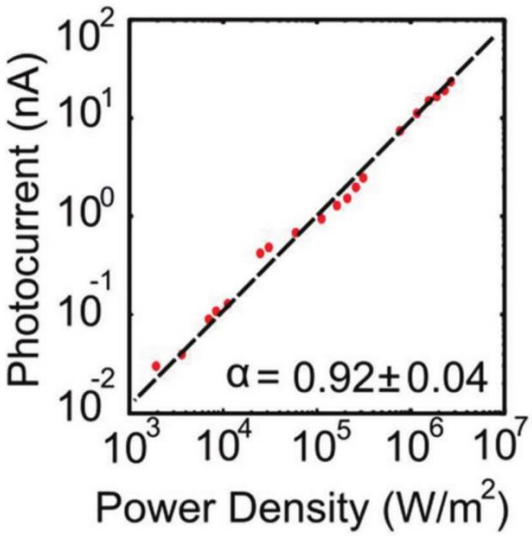

Figure 3.7: *Photocurrent versus illuminating laser power, taken with the modulated laser apparatus. The 685 nm is modulated at 10 Hz and signal recorded by the lock-in amplifier. The slope (α) of the resulting linear dependence is ~1, indicating that the photovoltaic effect is the dominant photocurrent generating mechanism.*

3.4.2. Scanning Photocurrent Microscopy and the Band-Bending Assisted Photocurrent Mechanism

Photocurrent mapping (i.e. measurement of the photocurrent as a function of spatial position across the device) via scanning photocurrent microscopy (SPCM) was carried out to determine which regions of the device were responsible for the generation of photocurrent. A 473 nm laser was used due to the smaller laser spot diameter (0.9 μm) cf. the 685 nm laser. The laser was modulated at 5 Hz to avoid any persistent photocurrent effects confusing the results.

Results are shown in Figure 3.8, where photocurrent maps at V_{ds} values of 0, 1 and -1 V are given. It is clear from these maps that the origin of the photocurrent in these devices is predominantly at the interfaces between the metals of the electrodes and the $MoTe_2$ channel.

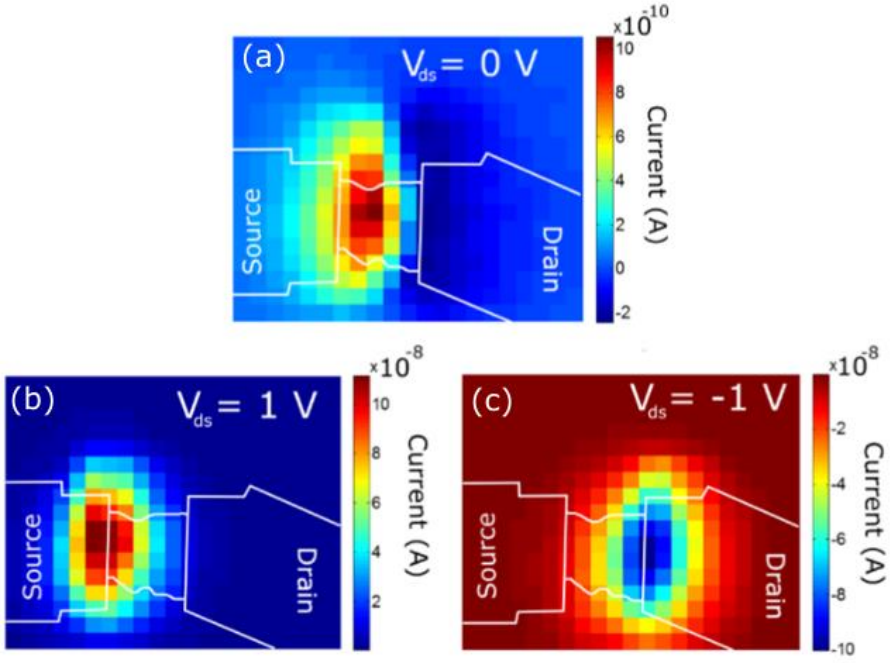

Figure 3.8: *Photocurrent maps at: a) V_{ds} = 0 V b) V_{ds} = 1 V and c) V_{ds} = -1 V, showing the photocurrent generation is mainly at the semiconductor to metal interface when using a 5 Hz modulated 473 nm laser.*

In the map at zero bias (short circuit), the strongest photocurrent is generated at both the source and drain $MoTe_2$/metal interfaces in the transistor. The behaviour at $\mathbf{V_{ds}}$ = 0 V is attributed to the photothermoelectric (PTE) effect[120] which has previously been

observed as an important effect at zero bias conditions.[126] PTE is a very weak effect for the four-layer $MoTe_2$ when compared to all other photocurrent mechanisms, with very low order of magnitude (100 pA) and so is not seen in power dependence measurements taken at $\mathbf{V_{ds}}$ = 5 V. Since the PTE effect is where the energy from absorbed photons leads to an increase in temperature, here in both the metal contact and the $MoTe_2$, then, due to the difference in Seebeck coefficients of these different materials, a temperature gradient forms which translates to a minor difference in voltage at the interface.

Photocurrent at zero bias may also be generated by band-bending at the metal contact/$MoTe_2$ interface, which reduces the height of the Schottky Barrier to allow for greater conduction, making the interfaces the focal point for photocurrent generation. For the band-bending assisted photocurrent, as the source electrode is illuminated a positive photocurrent is created by moving electrons to the drain electrode and holes to the source electrode, driven by the built-in electric field from the applied bias.[127] A much smaller built in electric field is present in the case where no V_{ds} is applied. A negative photocurrent is created through reversing the direction of electrons and holes, which is why a negative photocurrent is observed Figure 3.8(a).[127]

With a $\mathbf{V_{ds}}$ of 1 or -1 V, the photocurrent is generated at a single interface (i.e. between one of the metal contacts and the $MoTe_2$ channel) due to the change in the Schottky barrier, with the source interface generating photocurrent under positive bias and the drain interface with negative bias. Photocurrent with an applied bias is two orders of magnitude greater than at zero bias because of the greater built-in electric field created by the applied bias. A model for the band-bending-assisted increase in the photocurrent is well known and displays the same characteristics.[127,128] This is the defining mechanism for photocurrent measurements without an applied gate.

Overall, the same mechanisms for photocurrent generation without an applied gate are observed, explained from SPCM mapping measurements. The band-bending assisted Schottky barrier lowering is the photocurrent mechanism which dominates with applied source-drain bias.

3.4.3. Photocurrent Response Time

For photodetectors it is not only the responsivity of a device/material that is important, but other aspects, in particular the speed of response, also play a very significant role in determining suitability for particular applications. The response times of TMDC based photodetectors reported in the literature have, in general, been rather slow, often in the millisecond or even second range (see Figure 3.11 below and associated discussion). Thus, the photodetection speed of the $MoTe_2$ devices reported in this chapter was investigated.

More specifically, the rise and fall times of $MoTe_2$ FETs were determined by recording oscilloscope traces of the photocurrent when devices were exposed to square-wave modulated laser light. However, it should be noted that the particular definition used for the rise and fall time can lead to apparent differences in reported device response times, as discussed by Pradhan et al. The three definitions that are typically used are (i) the time between the 90/10% cut-offs of the response to a step-like excitation (see Fig. 3.9(a)), (ii) the time between a ±3 dB (70.7%) change of the response (again to a step-like excitation, see Fig. 3.10) and (iii) a time constant extracted from the response via exponential fitting (see Fig. 3.9(b) and (c)).

Figure 3.9(a) shows typical results, here for illumination by a 685 nm laser modulated at 178 Hz and using a 4-layer $MoTe_2$ device. A rise time of 160 μs and fall time of 300 μs are found from this measurement (using the 90/10 % definition of rise/fall times), which is a considerably faster than many literature reports (again, see Figure 3.11 later). In particular, it is noted that monolayer flakes in literature have previously shown poor photocurrent speeds,[39,50,52,104,129–131] possibly due to the entire semiconducting channel being in close proximity to the substrate, dominating the properties of the TMDC (hence the use of 4-layer flakes in this study). In Figure 3.9(b) and (c) the rise and fall times are fitted with exponentials, which extract similar rise and fall times of 90 μs and 100 μs respectively.

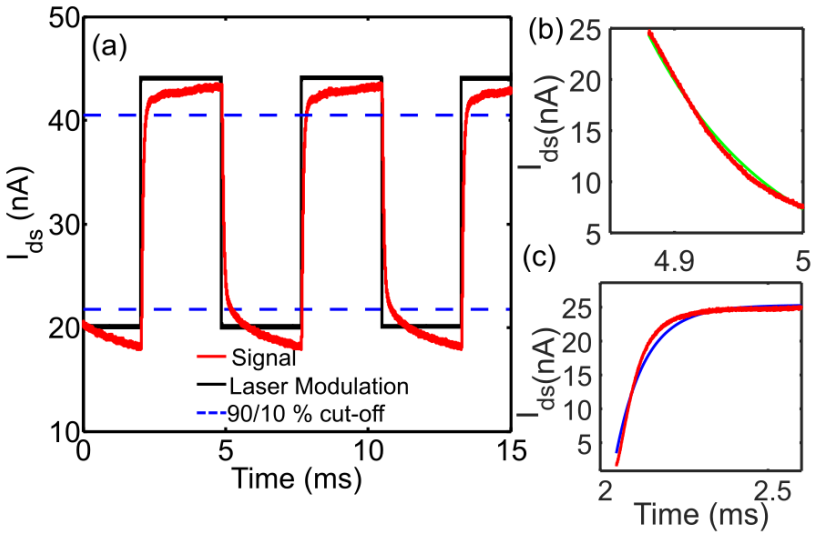

Figure 3.9: *Photocurrent response of a 4-layer $MoTe_2$ FET device under illumination by a 178 Hz square-wave modulated 685nm laser. (a) Full oscilloscope trace of multiple on/off events. (b) Zoomed-in area of where the rising signal crosses the 90% threshold (top dashed blue line). (c) Zoomed-in area of where the drop in photocurrent crosses the 10% threshold (bottom dashed line).*

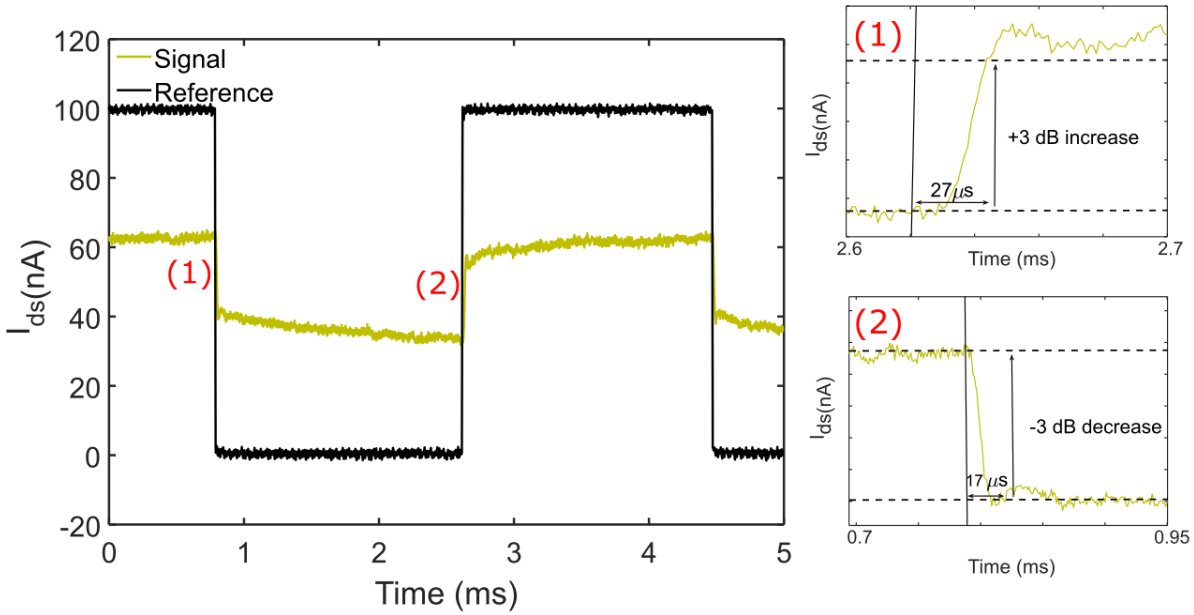

Figure 3.10: *photocurrent switching at 271 Hz for a 6 layer flake using an AC source and 561 nm laser, used to extract the 3 dB gain/drop in signal to attain the fastest response times.*

Using the ±3 dB response time commonly used in industry, the fastest response time is extracted for a thicker, six-layer flake, 561 nm laser, modulated at 271 Hz. By using flakes of greater thickness, photocurrent response times have been shown to decrease.[118,132] Using the ±3 dB definition, faster photoresponse times are obtained as only a ±70.7% change in the photocurrent defines the switching speeds. This measurement is shown in Figure 3.10 where switching speeds of 27 μs and 17 μs for the rise and fall rise times are found, which compares very favourably to literature values, where the best times have been recorded in similar orders of magnitude.[118,132] Note also that this measurement was limited by the >10 μs response time of the current preamplifier, and so the inherent response time of the $MoTe_2$ devices could in fact be lower than that recorded here.

The reasons for this fast photoresponsivity may be due to the flake thickness used, as the best results for two contact TMDC devices generally come from few-layer flakes.[118,133] Crystal quality may also play a role, since this has also been highlighted to improve the photocurrent response times for SnS_2 devices.[132]

A comparison of the overall performance of pristine flake devices of TMDCs, comparing literature reported values of the photo response speed (s) and photoresponsivity (A/W) (at the time of publication for the results in this chapter) is shown in Figure 3.11, where it can be seen that the $MoTe_2$ devices developed in this thesis are amongst the fastest of all, while still competitive in terms of photoresponsivity.

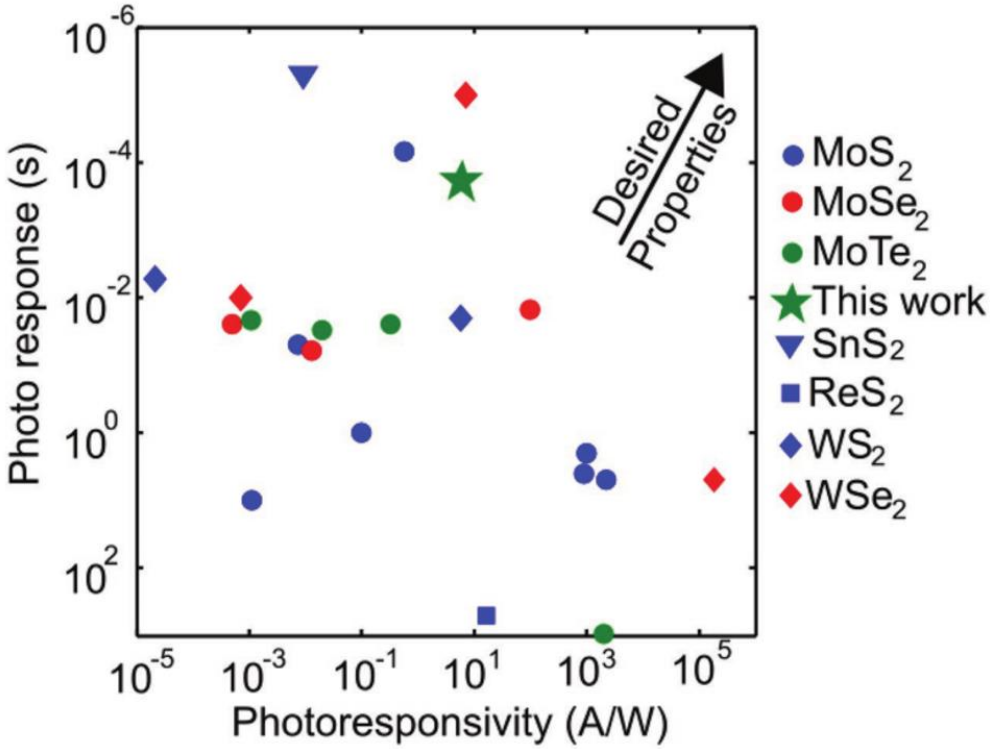

Figure 3.11: *Comparative figure of photoresponsivity and photo response times for pristine TMDC flake devices reported in the literature. References for work on TMDCs:* MoS_2,[50,52,104,129,130,133,134] $MoSe_2$,[39,131,135] $MoTe_2$,[69,71,79,136] SnS_2,[132] ReS_2,[137] WS_2,[138,139] *and* WSe_2[118,123,140]. *Our own work on* $MoTe_2$ *is highlighted by the green star.*

More details of the measurement conditions for the the data points shown in Figure 3.11 are given in Table 3.1. The data in this table shows that under similar measurement conditions, the four-layer $MoTe_2$ is a comparable photodetector.

TMDC (thickness)	V_{ds} (V)	V_G (V) (Max)	Wavelength (nm)	Environ.	Contact	R (A/W)	Photoresponse time (s)
MoS2[6] (1L)	8	-70	561	Ambient	Au	880	4
MoS2[7] (1L)	1	50	550	Ambient	Ti/Au	7.50E-03	5.0E-02
MoS2[17] (1L)	1	100	473	Vacuum	Ti/Au	2200	5
MoS2[19] (1L)	5	100	532	N_2	Ti/Au	1000	2
MoS2[35] (+30L)	1	5 (Al_2O_3 dielectric)	633	Ambient	Ti/Au	0.1	1
MoS2[36] (1L)	1.5	N/A	515	Ambient	Ti/Au	1.10E-03	10
MoS2[32] (3L)	10	N/A	532	Ambient	Au	0.57	7.0E-05
MoSe2[39] (1L)	10	N/A	532	Ambient	Au	0.013	0.06
MoSe2[38] (1L)	1	60	532	Ambient	Ni/Au	5.00E-04	0.025
MoSe2[37] (25L)	20	20	532	Ambient	Ti	97.1	0.015
Our_work **MoTe2 (4L)**	5	-40	685	Ambient	Ti/Au	6	1.9E-04
MoTe2/Gr[22] (10L/2L)	2	-40	532	Ambient	Cr/Au	0.02	0.03
MoTe2/MoS_2[23] (4L/4L)	N/A	N/A	473	Ambient	Ti/Au	0.322	0.025
MoTe2[9] (8L)	-0.2	-10	550	Ambient	Ti/Au	0.001	0.05
MoTe2[21] (10L)	0.5	80	473	Ambient	Au/Cr/Au	2560	N/A
ReS2[40] (~10L)	0.2	50	633	Ambient	Cr/Au	16.14	500
SnS2[33] (+30L)	2	10	633	Ambient	Cr/Pd	0.009	5.0E-06
WS2[41] (10L)	30	N/A	458 - 647	Vacuum	Ti/Au	2.10E-05	5.3E-03
WS2[42] (+60L)	1	5	532	NH_3,	Au	5.7	0.02
WSe2[26] (3L)	1	-150	532	Ambient	Ti/Au	7	1.0E-05
WSe2[43] (1L)	5	-60	650	Ambient	Pd	1.80E+05	5
WSe2[44] (1L)	1	6	532	Vacuum	Cr/Au	7E-04	0.01

Table 3.1*: A table summarising the flake thickness, V_{ds}, V_g, wavelength, operating conditions, metal contacts and figures of merit for the photodetectors reported in Figure 3.11.*

3.5. Bandwidth Measurements with h-BN Encapsulation

Although the photoresponse speed for the $MoTe_2$ devices reported above was very impressive, being faster than for many other reports on TMDC-based photodetectors, it may be possible to improve the speed of response further by reducing the influence of adsorbates and trap states, ever present in $MoTe_2$. Attempts were therefore made in the work of this thesis to isolate $MoTe_2$ from ambient conditions by encapsulating the flake with an h-BN layer, using the method for heterostructure fabrication described in Section 2.1.3.

A number of h-BN protected/encapsulated $MoTe_2$ devices were fabricated, including three-layer $MoTe_2$ device encapsulated with h-BN, along with a four-layer flake of $MoTe_2$ isolated from the SiO_2 substrate by h-BN. In these devices, the -3 dB bandwidth was measured by measuring the amplitude of the photocurrent as a function of frequency (using lock-in techniques). It was found that the h-BN encapsulated 3-layer $MoTe_2$ device, and un-encapsulated 3-layer device and the 4-layer device with just an h-BN layer between the $MoTe_2$ flake and the substrate all had identical -3 dB frequencies of 7.5 kHz, i.e. a response time of 133 μs. The frequency responses of all three devices are shown in Figure 3.12.

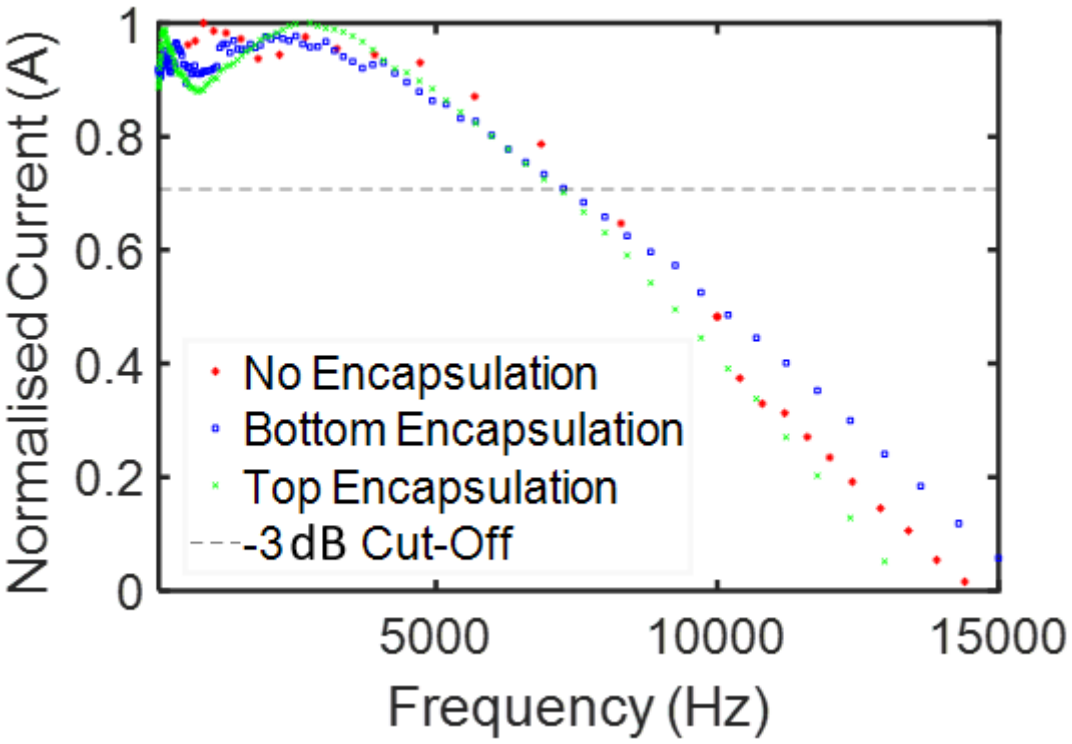

Figure 3.12: *Bandwidth measurement of un-encapsulated, partially encapsulated and fully encapsulated (by h-BN) $MoTe_2$ devices, all showning a -3 dB bandwidth of 7.5 kHz and response times of 133 µs.*

From the above results it appears that the h-BN encapsulation method had no effect on the bandwidth of the resulting photodetector devices. This may be due to the fact that (i) the h-BN encapsulation method does not decrease the photoresponse times, (ii) the h-BN encapsulation was not performed correctly or (iii) limitations with the experimental apparatus. The experimental limit could be due to the response time of the current amplifier used to extract the signal. Since all three bandwidth results culminate in the same value, a different approach should be considered to assess the bandwidth of encapsulated devices. While great care was taken here, using a controlled-air cleanroom for the encapsulation, ideally the process would be carried out in vacuum, since it is known that the fabrication of heterostructures in air can create defects, often seen as microbubbles formed during stamping processes,[97] as described previously in Section 2.1.3.

Future work to find the true photocurrent response times through full encapsulation of $MoTe_2$ should therefore be performed to find the optimal device photodetector properties of $MoTe_2$. It is most likely that a better experimental approach is required to obtain a change in the response time of encapsulated $MoTe_2$. Encapsulation with HfO_2 deposited by atomic layer deposition has already shown great improvement for the photocurrent response time for MoS_2,[141] the same method could also be used for $MoTe_2$.

3.6. Conclusions

The results of this chapter show that 2D $MoTe_2$ materials, here in particular pristine four-layer flakes, can be used to provide fast, high photoresponsivity FET-based photodetector devices for use in the visible part of the spectrum. Due to the high surface area to volume of $MoTe_2$, the photogating mechanism prevalent in low-dimensional materials lead to high photoresponsivities of 6 A/W when the FET is in the ON state. This was coupled with very fast (for TMDC-based devices) photocurrent response times of 20 μs. Schottky barrier lowering through band-bending at the $MoTe_2$/metal contact interface was found to dominate the photocurrent generation without an applied gate voltage. Attempts to decrease the response time through encapsulation with h-BN showed no effect, potentially from the fabrication process used here for heterostructures. In future, flakes of $MoTe_2$ should be fully encapsulated in a vacuum system by h-BN to determine the fastest possible photoresponse times.

4. Understanding the Trap States in $MoTe_2$ via Transient Electrical Measurements

4.1. Introduction

The performance of FETs made from TMDCs and other two-dimensional materials has shown promise to replicate or improve upon the performance of silicon-based electronics in terms of mobilities, ON/OFF ratios and subthreshold values. However, the performance of two-dimensional devices in transient measurements is not well understood and currently lacks a detailed theoretical description. Due to their large surface area to device volume, TMDC properties are dominated by surface states which can then in turn determine their optoelectronic properties. Here, therefore, transient electrical measurements of $MoTe_2$ are used to explore trap states in more detail, with a theoretical model created and tested, to achieve a better understanding of the origin of trap states in all TMDCs.

To create this model for transient current, $MoTe_2$ FET measurements are recorded in the ON and OFF states, with the current examined as a function of time. The transient rise and decay for devices are fitted by a double exponential with two time constants with different orders of magnitude, showing the existence of two types of trap states. Along with transient measurements, transfer characteristics of the devices are obtained in vacuum and show the existence of mid-gap trap states in $MoTe_2$ and the extent to which they dominate the electrical properties of TMDCs in ambient conditions.

In what follows, the theory of classical FET transients is provided as a reference point in the investigation of transient current for TMDCs. A separate, novel theory for atomically thin FET transients is then created from the fact that the FET threshold voltage, $\mathbf{V_T}$, changes with respect to the trap state population, proving the existence of two types of trap states. This novel theory is then tested for validity by changing the $\mathbf{V_{ds}}$ values for transient measurements, showing a linear relationship between $\mathbf{V_{ds}}$ and the decay coefficient for deep traps, whereas shallow trap states show no $\mathbf{V_{ds}}$ dependence as they

do not originate from the material itself but adsorbates on the surface of $MoTe_2$. This new trap-limited transport theory is, it turns out, applicable to other TMDCs, not just $MoTe_2$, and was also shown to work for WS_2 devices by colleagues Amit et al. (who devised this theory).[86] This work also shows that care needs to be taken when carrying out the electrical characterization of $MoTe_2$, especially when recording transfer characteristics which show a relatively fast current decay, as the mobility of $MoTe_2$ may be under reported due to trap-induced effects.

4.2. Evidence of Trap States in $MoTe_2$

Two-dimensional materials are known for showing properties strongly defined by trap states, and, as shown in the previous chapter, such trap states can be responsible for the large photocurrent gain effect due to the photogating mechanism. One way to quantitatively examine the density of trap states is to observe hysteresis in FET transfer characteristics. Trap states are responsible for hysteresis in transfer characteristics due to charges being trapped and released from the trap states, depending on the direction of the gate voltage sweep. Due to the charge trapping and emission, transient measurements for FETs in the ON and OFF states show decay and gain respectively, which can be fitted with time constants to show the rates at which these processes occur.

In this section, evidence for the existence of trap states on $MoTe_2$ is shown by examining FET transfer characteristics in ambient and vacuum conditions, as well as from transient measurements. The equation governing the threshold voltage, $\mathbf{V_T}$, will be explored and it will be shown that changes in $\mathbf{V_T}$ are made through the trap state population. A pictorial representation of trap states, which exist between the valence and conduction band in mid-gap states, is also given to better understand the mechanisms of trap states for the ON and OFF states.

4.2.1. FET Transfer Characteristics in Ambient and Vacuum Conditions

The presence of trap states and their prominence in ambient and vacuum conditions is here presented by measuring the difference in the threshold voltage for FET transfer characteristics. The origin of trap states is invariably adsorbates on two-dimensional

materials, which, due to their large surface to volume ratio, have a big impact on electronic properties. In Figure 4.1 the hysteresis properties of an FET made using a 4-layer $MoTe_2$ flake in both vacuum (10^{-4} Torr) and in ambient conditions are shown. In vacuum, the FET shows small hysteresis, with only a 2 V change for $\mathbf{V_T}$ between up and down sweeps. In ambient, this change in $\mathbf{V_T}$ is more than six times greater, at around 13 V. The difference here indicates that adsorbates, such as water and oxygen, from ambient conditions are responsible for the trap states, as they are removed from the surface in vacuum conditions where the hysteresis is much smaller.

During the sweep, trapped charges affect the doping in the FET as they are captured in the ON state causing a reduction of current in the down sweep. In the up sweep, the reverse happens, charges are emitted in the OFF state. Trapped charges can also be removed by using gate pulsing strategies, which removes the hysteresis by perturbing the trap states,[142] releasing trapped charges from mid-gap states.

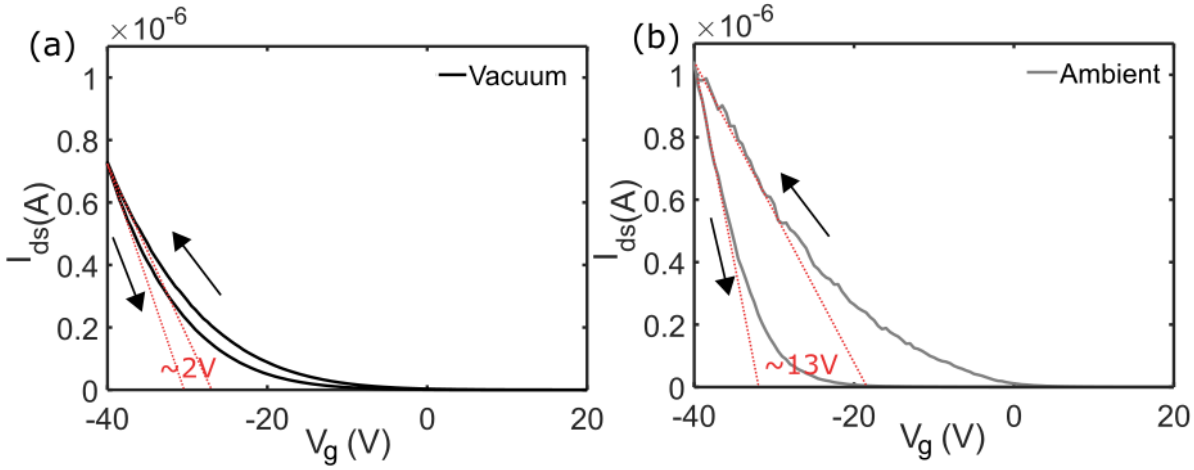

Figure 4.1: *Transfer characteristics at V_{ds} = 1 V for a 4-layer $MoTe_2$ flake in (a) vacuum and (b) ambient conditions, showing the hysteretic properties in the two measurement conditions. Ambient conditions show a 6-fold increase in the ΔV_T as compared to measurements made in vacuum.*

Further comments on the origin of these traps can be made by identifying the change in charge neutrality in ambient conditions for the FETs. Traps can be localised in the following areas: (i) the $MoTe_2$ - metal contact interface, (ii) the $MoTe_2$ - dielectric interface, (iii) the $MoTe_2$ - ambient (atmosphere) interface. Large hysteresis is indicative

of very significant change to the doping levels of the $MoTe_2$ through trapped charges, which are argued to originate here from adsorbates.

In Figure 4.2 the transfer characteristic of a $MoTe_2$ FET fabricated on top of an h-BN flake is shown. In this transfer characteristic, h-BN flakes are used to remove any doubt that it is the $MoTe_2$ – ambient interface that is responsible for trap states, as the $MoTe_2$ is isolated from the SiO_2 dielectric. Here, the charge neutrality point, highlighted in Figure 4.2(a), changes by 50 V between the up and down voltage sweeps. If the $MoTe_2$/metal contact interface were the source of traps, changes to the subthreshold swing would be observed since Fermi-level pinning has a strong effect on the subthreshold swing (SS).[143] For reference, SS is defined as $\mathbf{(d\log_{10}I_{ds}/dV_g)^{-1}}$. In Figure 4.2(b) the subthreshold swing does not change between the up and down sweeps of the transfer characteristic staying at ~2 V Dec^{-1}, so the $MoTe_2$/metal contact interface is unlikely to be the origin of traps. By using $MoTe_2$ devices with h-BN substrates and still observing significant hysteresis, the interaction between $MoTe_2$ and the atmosphere is thought to be the origin of traps, attributable to adsorbates and water molecules.

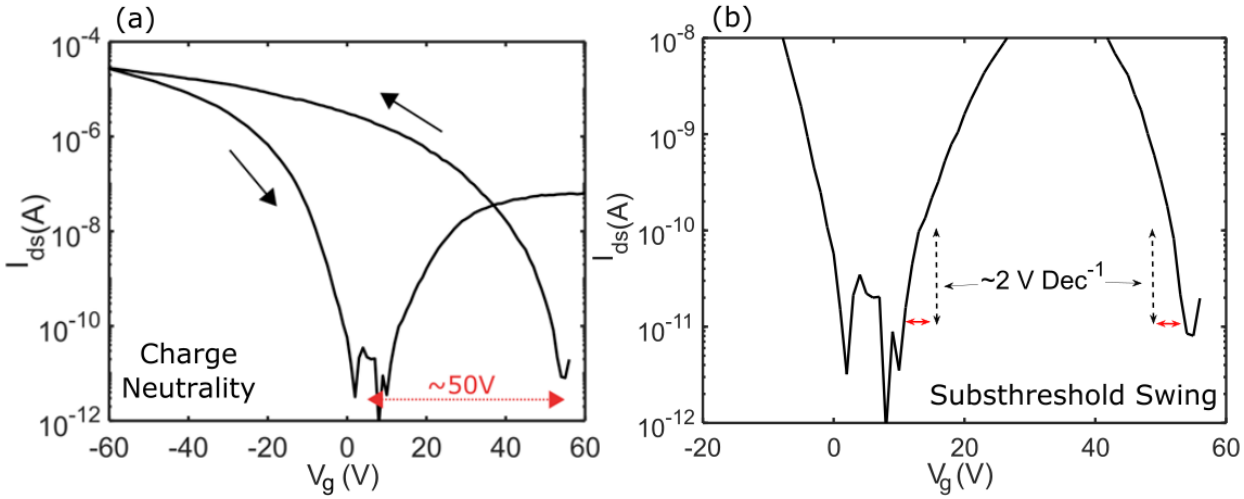

Figure 4.2: *(a) Log-scale transfer characteristic of $MoTe_2$ at V_{ds} = 5 V on h-BN, showing the shift in charge neutrality point by ~50 V. This infers that the $MoTe_2$ ambient (atmosphere) interface is the origin for charge traps. (b) Same plot, examining the subthreshold swing by examining the steepest slope from the charge neutrality points in (a).*

4.2.1.1. Threshold voltage

To show that the change in $\mathbf{V_T}$ is indicative of a change in the trap state population, the well-known equation which describes the threshold voltage in field effect transistors is shown in Equation (4.1):

$$\boldsymbol{V_T = \varphi_{MS} - \frac{Q_i}{C_{ox}} - \frac{Q_T}{C_{ox}} - \Delta E_F} \qquad \textbf{(4.1)}$$

Here $\boldsymbol{V_T}$ is the threshold voltage, $\boldsymbol{\varphi_{MS}}$ is the difference in work function between $MoTe_2$ and the contact metal (Cr in this case), $\boldsymbol{Q_i}$ is the static charge density present in the dielectric underneath $MoTe_2$ (which for the transient measurements is SiO_2 and h-BN), $\boldsymbol{Q_T}$ is the trapped charge density between the $MoTe_2$ – dielectric interface, $\boldsymbol{C_{ox}}$ is the gate dielectric capacitance and $\boldsymbol{\Delta E_F}$ is the difference in Fermi energy required to turn onthe transistor. The only variable in Equation (4.1) that can be changed during the gate sweep is $\boldsymbol{Q_T}$, clarifying that a change in $\mathbf{V_T}$ is indicative of a change in the trapped charge density, via the process of charge trapping during the transfer characteristic. To see the charge trapping process unfold, transient measurements for the $MoTe_2$ FET are taken in the ON and OFF states, with the decay or rise in current fitted by exponentials.

4.3. Transient Measurements in ON and OFF State for $MoTe_2$ FETs

To attain transient measurements, $\mathbf{V_{ds}}$ values are set to an appropriate level (in the results presented here 1 V) then the gate voltage is swept (here at 1 V/s) to a fixed value (here +50, 0 and -50 V) immediately after which transient measurement is started to obtain the temporal decay or rise in the current (arising due to the emission and capture of charges from trap states).

Transient measurements in TMDCs have been shown in the literature for MoS_2 for devices in the ON state, with transient results measured by Late et al.[95] under vacuum, dry air and different humidity values. The results from Late et al.[95] show that the exponential decay of source-drain current seen in transient measurements could be fitted with a double exponential with two separate time constants. These time constants were found to change depending upon the measurement conditions, with decay being fastest

in ambient conditions, increasing in speed with higher humidity, whereas vacuum measurements showed slower decay. In the same study, water molecules are attributed as the source of the charge traps which exist in MoS_2 devices. This study from Late et al. is used as a basis for fitting transient rise and decay of the source-drain current $MoTe_2$ FET devices developed in this thesis

In Figure 4.3 the transient measurements for a seven-layer $MoTe_2$ FET on an h-BN substrate are shown at three values of $\mathbf{V_g}$: +50, 0 and -50 V. An h-BN substrate was used to ensure trap states did in fact originate from adsorbates and not the SiO_2 substrate. For the +50 and 0 V results, an increase in $\mathbf{I_{ds}}$ is observed as the device is in the OFF state at these $\mathbf{V_g}$ values, so trapped holes are being emitted into the channel causing a slow increase in the current. For the -50 V result, a slow decrease is observed as the device is capturing holes in the channel decreasing the carrier density.

The double exponential fit used in Figure 4.3 is determined by a standard exponential expression, the same used by Late et al.[95] and is shown in Equation (4.2):

$$\boldsymbol{I_T = A_1 e^{-t/\tau_1} + A_2 e^{-t/\tau_2}} \qquad \boldsymbol{(4.2)}$$

A summary of the time constants and coefficients obtained by fitting Equation (4.2) to the results of Figure 4.3 are shown in

Table 4.1: Overview of the time constants and coefficients obtained by fitting the double exponential expression of Equation (2) to the transient current measurements of MoTe2 on h-BN. The error for all values is set to ±5%.

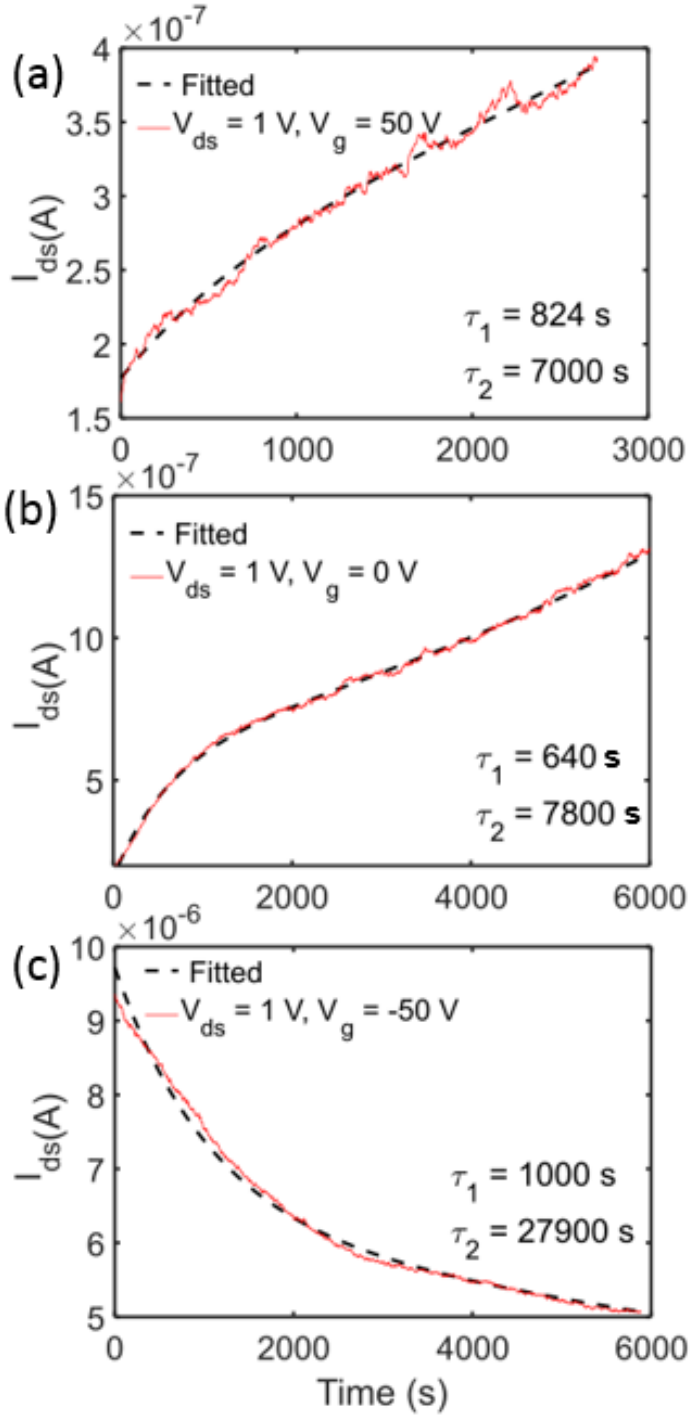

Figure 4.3: *Transient current measurements for a $MoTe_2$ FET comprising a seven-layer flake on top of h-BN. Transient measurements in the (a) OFF state (V_g +50 V), (b) no applied gate (V_g 0 V) and (c) ON state (V_g -50 V). V_{ds} = 1 V in all cases.*

Gate Voltage (V)	A_1 (nA)	τ_1 (s)	A_2 (nA)	τ_2 (s)
50	-89	825	266	-7000
0	-440	640	600	-7800
-50	3480	1000	6240	27900

Table 4.1: *Overview of the time constants and coefficients obtained by fitting the double exponential expression of Equation (2) to the transient current measurements of $MoTe_2$ on h-BN. The error for all values is set to ±5%.*

It can be seen in

Table 4.1 that $\boldsymbol{\tau_1}$ ranges from around 600 to 1000 s, while $\boldsymbol{\tau_2}$ from -7800 to 27900 s. The two time constants differ in magnitude very considerably, indicating that the two types of trap must originate from two different set of states: one a deeper state whose energy is firmly in between the valence and conduction band, and the other a shallower trap close to the valence band edge. The time constants seen here are much larger than those seen by Late et al.[95], however in that study monolayer MoS_2 was used and monolayers are more greatly affected by the trap states as the entire channel is in contact with adsorbates. The seven-layer flake used here has six layers not in direct contact with the trap states, so will be less affected leading to slower transient response. It is also possible that some contribution towards the mid-gap energy states comes from the h-BN layer in contact with the $MoTe_2$, specifically from adsorbates between the two materials, trapped during the heterostructure fabrication. Isolation from the SiO_2 will reduce the effect of trap states on $MoTe_2$, as the h-BN forms a cleaner interface with TMDCs, in some cases removing large amounts of hysteresis when used as a substrate.[3] Measurements completed by Amit et al.[86] report on time constants of $\boldsymbol{\tau_1} \approx 250$ s and $\boldsymbol{\tau_2} \approx 2900$ s for $MoTe_2$ on SiO_2 directly, indicating that in the measurements shown in Figure 4.3 the h-BN is contributing to the larger transient decay time constants.

It can be seen in

Table 4.1 that in some cases the time constant $\boldsymbol{\tau_2}$ and the coefficient $\mathbf{A_1}$ from the double exponential fit are negative, which requires clarification. The result in the ON state at $\mathbf{V_g}$ = -50 V is clear, as all time constants and coefficients are positive, meaning both exponential expressions are current decay terms. For the result at +50 $\mathbf{V_g}$ and 0 $\mathbf{V_g}$, the negative sign for coefficient A_1 means this component contributes to an increase of $\mathbf{I_{ds}}$. In the second exponential, the sign of $\boldsymbol{\tau_2}$ also changes, meaning that this component is no longer an exponential decay but a very slow exponential increase in $\mathbf{I_{ds}}$. In this case, if the experiment were to last for a much longer period of time, $\lim_{t\to\infty} e^t \to \infty$, the transient current, $\mathbf{I_{ds}(t)}$, would reach infinity. This obviously cannot occur, so Equation (4.2) is approximately valid up to, and including time $\mathbf{t} \approx \boldsymbol{\tau_2}$. If left for enough time, the trap state population will reach an equilibrium state where all charges are trapped, resulting in no further change of the transient current. Charge trap saturation is in fact a boundary condition used in classical current transient theory, and is not shown in Figure 4.3 as a greater time scale is required to observe the saturation of all trap states in the $MoTe_2$ FET.

From the results of Figure 4.3, where the transient double exponential fits experimental results well over time periods of up to one hour, there are clearly two different types of traps in operation. This leads to there being two driving mechanisms between capture and emission of trapped charges, determining the electrical properties of $MoTe_2$ and other TMDCs. A pictorial description of the charge trap states is provided below to clarify the mechanisms involved for the decline and increase of current during transient measurements.

4.4. Pictorial description of trap states

The two types of traps are separate through their clear difference in time constants, and fall into categories of shallow and deeper traps. Typically, shallow traps originate from adsorbates and require little energy to remove charges from them. Deep level traps can be troublesome in transistors, as the energy required to remove carriers from these traps is much larger, causing reductions in field effect mobility through the trapping of excited carriers. While this chapter reports of the existence of two types of trap in $MoTe_2$ FET devices, the origin of these traps is not fully known – clearly adsorbates contribute to the trap state population (as previously demonstrated by examining changes in $\mathbf{V_T}$ in ambient

conditions). Deeper level traps may originate from defects (such as vacancies in the crystal structure) which may originate from Chalcogenide deficiencies attained from crystal growth.

In the case of two types of traps, the two trap state energies ($\mathbf{E_{T1}}$ and $\mathbf{E_{T2}}$) lie below the Fermi energy ($\mathbf{E_F}$) in the OFF state of the FET. As the trap states are below $\mathbf{E_F}$, the traps are filled with electrons instead of holes. Any holes that were in the traps are emitted from the trap states in the OFF state. In the ON state, the $\mathbf{E_F}$ shifts downwards due to the high number of conducting holes. The trap states which are now above $\mathbf{E_F}$ will as a result become energetically favourable for holes to occupy in the ON state. The trapping of the holes reduces the ON state current over time. A pictorial description of the trap states in the OFF and ON states is shown in Figure 4.4.

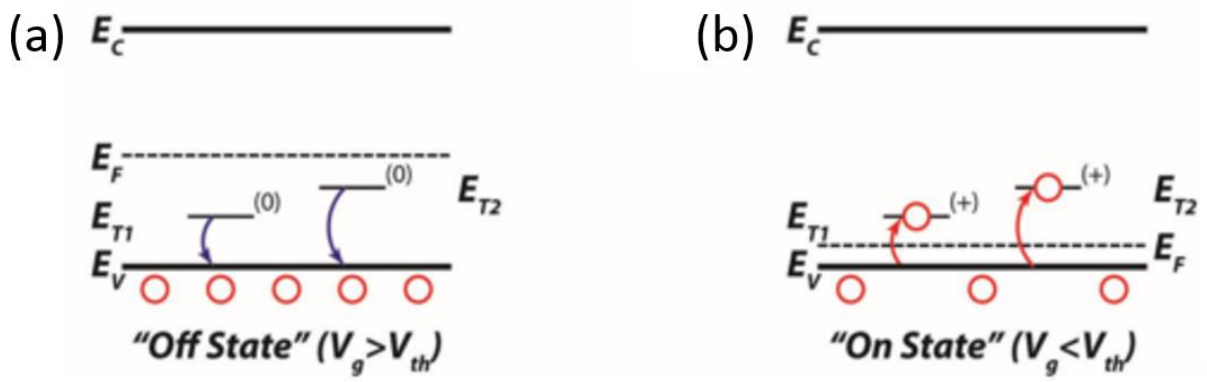

Figure 4.4: *Energy band diagrams for the (a) OFF and (b) ON states in $MoTe_2$. (a) In the OFF state, holes emit from the two different types of trap states at different rates, increasing the current. (b) In the ON state, holes are captured from the valence band into the trap states, causing the current to decrease. Figure reproduced from Amit et al.*[86]

4.5. Theory for Current Transients in $MoTe_2$ FETs

To obtain a description of the effect of the two types of charge traps on the transient behaviour of $MoTe_2$ FETs, the theory for current transients is discussed in this section. The difference between classical semiconductor physics and 2D semiconductors is determined through equations examining time-dependent changes in the threshold voltage. A derivation for the classical transient current will be provided first by way of a reference, followed up by a derivation for atomically-thin semiconductor transient

measurements which describe the results obtained here. The theory relating to the 2D case was derived by my colleague Iddo Amit and reported in Amit et al.[86]

4.5.1. The Classical Case

Classical theory comes from examining the hole capture and emission rates, finding the limits where all traps are occupied or empty so as to create an expression for the density of holes in occupied states. This expression is then used in the classical transient current equation to obtain a solution for classical transient current. The final expression has no dependence on $\mathbf{V_{ds}}$.

First the hole capture and emission rates will be defined. Taking the example of hole capture in the ON state, let the rate of hole capture from the valence band, $\mathbf{R_{pc}}$, be proportional to the hole density in the valence band, $\mathbf{p}$, and the density of unoccupied traps, $(\mathbf{N_T} - \mathbf{p_T})$. The total density of trapped states is taken as $\mathbf{N_T}$ and $\mathbf{p_T}$ is the density of the holes in the occupied states. . The resulting expression for the hole capture rate is then as shown in Equation (4.3):

$$\boldsymbol{R_{pc} = \left.\frac{\partial p}{\partial t}\right|_{capture} = -c_p(N_T - p_T)p} \qquad \textbf{(4.3)}$$

Where $\boldsymbol{c_p}$is the capture coefficient for holes.

The emission rate for holes, $\boldsymbol{R_{pe}}$ is similar in construction. It is assumed that unoccupied states in the valence band, where the holes are emitted, cannot limit the emission rate, as there are enough energy states in the valence band in $MoTe_2$ as it is a non-degenerate semiconductor, with a large enough band gap to not behave as a metal. The emission rate is thus as shown in Equation (4.4), noting $\boldsymbol{e_p}$ is the emission coefficient:

$$\boldsymbol{R_{pe} = \left.\frac{\partial p}{\partial t}\right|_{emission} = e_p p_T} \qquad \textbf{(4.4)}$$

Combining Equations (4.3) and (4.4), an expression for the total change in the traps is provided, as shown in Equation (4.5):

$$R_p = \left.\frac{\partial p}{\partial t}\right|_{capture} + \left.\frac{\partial p}{\partial t}\right|_{emission} = e_p p_T - c_p(N_T - p_T)p \quad (4.5)$$

In the limiting condition where the traps are fully saturated (if the device is left in the ON state), the total density of trapped states is equal to that of the density of holes in the occupied states ($\mathbf{N_T} = \mathbf{p_T}$). This condition simplifies $\mathbf{R_p}$ to become the emission term only in Equation (4.6):

$$R_p = \frac{\partial p}{\partial t} = e_p p_T \quad (4.6)$$

The other limiting condition to simplify the trapping and emission is when the device is left in the OFF state. In this case, every hole trap is left unoccupied due to emission, the implication being the change of hole density in the valence band and change in occupied trap states are both zero, as shown in Equation (4.7):

$$\frac{\partial p}{\partial t} + \frac{\partial p_t}{\partial t} = 0 \quad (4.7)$$

From these two Equations, (4.6) and (4.7), the solution $p_T(t)$ is found using an exponential function, as in Equation (4.8):

$$p_T(t) = p_T(0)e^{-t/\tau} \quad (4.8)$$

In this equation, $p_T(0)$ is equal to N_T, the trap occupation when all states are filled and $\tau = 1/e_p$, the decay constant per single trap. Putting this expression for $p_T(t)$ back in to the expression for $\mathbf{R_p}$ created in Equation (4.6) provides a total rate of change for the traps in terms of the decay constant $\boldsymbol{\tau}$, shown in Equation (4.9):

$$R_p = e_p p_T = \frac{N_T}{\tau} e^{-t/\tau} \quad (4.9)$$

In classical transient current measurements, the expression of Equation (4.10) is used to define the transient current:

$$I(t) = I_0 + qR_pA \tag{4.10}$$

Here I_0 is the steady state current, **q** is elementary charge and **A** is the area of the device. Using the expression for $p_T(t)$ in Equation (4.8), and combining this with the expression for $\mathbf{R_p}$ found in Equation (4.6), a complete expression for $\mathbf{R_p}$ is obtained. This in turn leads to the classical current transient expression being as given in Equation (4.11):

$$I(t) = I_0 + \frac{qN_tA}{\tau} e^{-t/\tau} \tag{4.11}$$

4.5.2. The Atomically-Thin Case

While the above theory works for classical semiconductors, a different approach is required for $MoTe_2$ and other atomically-thin materials. Due to the higher surface area to volume ratio of these devices, TMDCs are much more sensitive to their environment, seen already through hysteresis and transient measurements reported in this thesis. Of note is that this theory applies only for the deep traps intrinsic to the material itself, and not shallow traps which originate from adsorbates.

In particular, it was observed that in the transfer characteristic of $MoTe_2$ FETs the threshold voltage, $\mathbf{V_T}$, changes with time. A derivation of the transient current will thus require changes in $\mathbf{V_T}$ to be considered. To achieve this, the linear regime of a FET is the starting point for understanding the trap states in $MoTe_2$. The dependence of current over time is thus as shown in Equation (4.12):[94]

$$I_{ds}(t) = \frac{W\mu_pC_{ox}}{L}\left(V_T(t) - V_g - \frac{V_{ds}}{2}\right)V_{ds} \quad , \quad V_{ds} \ll (V_T - V_g) \tag{4.12}$$

In Equation (4.12) there is a limit which removes the V_{ds} term in red, so simplifying the equation. I_{ds} is the drain-source current, W is the device width, L is the length, $\mathbf{C_{ox}}$ is the oxide capacitance, μ_p is the hole mobility, V_T is the threshold voltage of the FET, V_g is the applied gate voltage and V_{ds} is the drain-source voltage. An expression for $V_T(t)$ can be appropriated from Equation (4.1):

$$V_T(t) = \varphi_{MS} - \frac{Q_T(t)}{C_{ox}} - \Delta E_F \quad , \quad Q_T(t) = (Q_i + qp_T(t)) \tag{4.13}$$

In the above, the expression for trapped charges, $Q_T(t)$, now includes stationary charges in the oxide, $\mathbf{Q_i}$, as a single variable. An expression for the density of holes, $p_T(t)$ is already known from Equation (4.8). Using this expression, Equation (4.13) can be rewritten to separate terms in $\mathbf{Q_T}$ as in Equation (4.14):

$$V_T(t) = \varphi_{MS} - \frac{Q_i}{C_{ox}} - \frac{qN_T e^{-t/\tau}}{C_{ox}} - \Delta E_F = V_{T,sat} - \frac{qN_T e^{-t/\tau}}{C_{ox}} \tag{4.14}$$

Expressions in Equation (4.14) that have no time dependence are grouped into the term $V_{T,sat}$. The expression for $I_{ds}(t)$ in Equation (4.12) is combined with this expression for $V_T(t)$ to create a helpful expression for $I_{ds}(t)$ with two distinct terms:

$$I_{ds}(t) = \frac{W\mu_p C_{ox}}{L}\left(V_{T,sat} - \frac{qN_T e^{-t/\tau}}{C_{ox}} - V_g\right)V_{ds} = I_{ds,sat} - \frac{qW\mu_P N_T V_{ds}}{L} e^{-t/\tau} \tag{4.15}$$

This equation for the transient current, $\mathbf{I_{ds}(t)}$, contains two clear expressions. One expression, $\mathbf{I_{ds,sat}}$ which does not vary with time and another expression which has dependence upon $\mathbf{V_{ds}}$. No dependence on $\mathbf{V_{ds}}$ is observed for classical transient current theory (see Equation (4.10)). As the expression for the transient current with changing threshold voltage has linear $\mathbf{V_{ds}}$ dependence, $\mathbf{V_{ds}}$ can be varied to check the validity of the theory. If the deep trap coefficient shows a linearity with $\mathbf{V_{ds}}$ then the theory as presented above would appear to be valid. Emission experiments proving this relationship are thus for deep traps shown in the next section.

4.6. Dependence of Emission Coefficients on V_{ds}

The emission coefficients at five separate $\mathbf{V_{ds}}$ values between 0.2 and 1 V were measured for a $MoTe_2$ FET. These emission experiments were conducted in ambient conditions and the relevant results are shown in Figure 4.5. The emission coefficients for both trap types as a function of source-drain bias are shown, to prove the threshold voltage dependent transient theory.

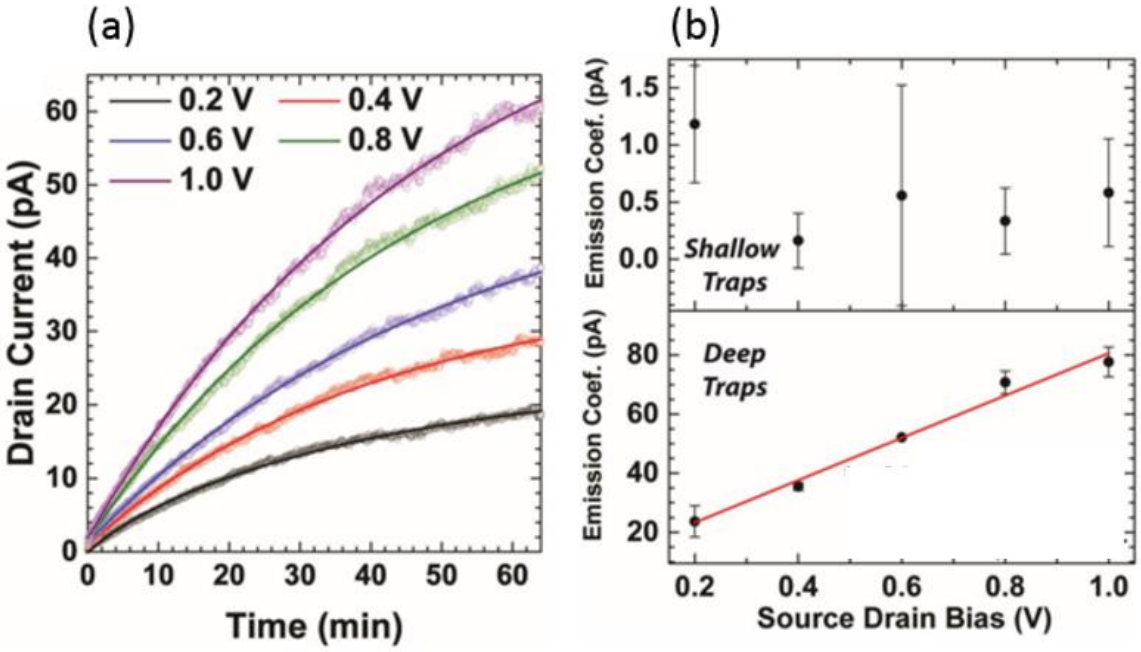

Figure 4.5: (a) *Current transient measurements for a $MoTe_2$ FET for V_{ds} values from 0.2 to 1 V. (b) V_{ds} dependence on the shallow and deep traps. Deep traps showed linear dependence with V_{ds}, with shallow traps showing no dependence on V_{ds}. V_g = 0 V for all emission experiments. Image reproduced from Amit et al.*[86]

From Figure 4.5 it is clear the two current transient measurements have a different relationship to $\mathbf{V_{ds}}$. The deep traps, which have a much larger emission coefficient than the shallow traps, are linear with $\mathbf{V_{ds}}$. Shallow traps show no dependence upon $\mathbf{V_{ds}}$. This is the same description for transient current measurements of the deep traps as in Equation (4.15), indicating that the theory for current transients with changing threshold voltage in 2D materials (as developed in the previous section) is valid. Indeed, measurements on CVD grown WS_2 showed the same behaviour as for of results as for the $MoTe_2$ devices studied here, with the shallow and deep traps having an identical relationship with $\mathbf{V_{ds}}$.[86]

4.7. Conclusion

Trap states are often seen as a nuisance to the electronic properties of TMDCs, generating unwanted hysteresis and causing transient current decay in the ON state of TMDC FETs.

However, trap states lead to the creation of very high photoresponsivities and detectivity through the photogating effect, as shown in this thesis in Chapter 3 and by others (e.g. Furchi et al.[104]). The trap states studied in this chapter are indeed the same as those reported in Chapter 3. Trap states can even be utilised for the creation of non-volatile memories,[144] showing the importance of finding a theoretical description for the trap states in TMDCs.

To investigate the nature of trap states in 2D $MoTe_2$, transient current measurements were carried out on FET devices, with the results being well-fitted by a double exponential expression separating the trap states into two different levels of shallow and deeper traps. As classical theory is not suitable for understanding the transient currents in TMDCs, a theory based upon the change of the threshold voltage during the transient measurement was adapted. From this, the two traps were found to respond differently to $\mathbf{V_{ds}}$, with shallow traps having no dependence and deeper traps showing linear dependence. This was experimentally proved by changing $\mathbf{V_{ds}}$ values for current transient measurements. Trap states are particularly important in $MoTe_2$ due to Te deficiencies leading to a higher proportion of dangling bonds, with higher densities of trap states than other TMDCs. Understanding how these trapped charges are emitted and captured provides knowledge for how to best use TMDCs in optoelectronics applications.

5. Photo-Desorption of Adsorbates on $MoTe_2$ using High Energy Lasers in Ambient Conditions

5.1. Introduction

Optoelectronic measurements on $MoTe_2$ with the 685 nm in Chapter 3 show that $MoTe_2$ is suitable for optoelectronic applications, with a band-bending assisted photocurrent mechanism and photogating creating a fast and high responsivity photoconductivity respectively. However, further photocurrent studies using higher energy (shorter wavelength) visible light lasers resulted in a rather different photocurrent mechanism that created a reduction, or in some cases a negative, photocurrent. These mechanisms for negative photocurrent are not often seen in literature, but are facilitated through the photo-desorption of adsorbates.[145,146] Te deficiencies are prevalent in $MoTe_2$, and when adsorbates are removed these Te deficiencies can create highly reactive centres for chemical and humidity sensing applications.[3-5] By using high energy visible wavelength lasers, it is possible to forcibly remove adsorbates selectively from areas of $MoTe_2$, leading to device applications which could exploit differences in trap state populations, such as memory[51,147,148] and photodetection[104,130] devices.

In this chapter, transient optoelectronic measurements are shown where an initial increase in photocurrent is observed, followed by a complete decay of photocurrent on the timescale of seconds. FET transfer characteristics with 561, 514 and 473 nm lasers show a decrease in conductivity by removing the source of trap states in $MoTe_2$ which contribute to doping. A dependence of the photo-desorption on the energy of incident photons is also observed, with the higher energy 473 nm laser causing the faster photo-desorption in $MoTe_2$. The dependence of photo-desorption on layer thickness is also demonstrated, showing that thin flakes are more susceptible to these effects. The photo-desorption is seen only for $MoTe_2$ flakes in ambient conditions, as adsorbates are removed by electrical annealing of devices in high vacuum.[65] By examining the dependence of this effect as a function of flake thickness and wavelength, future work on

using photo-desorption for devices is made possible, such as applications in humidity or chemical sensors, the former being examined in $MoTe_2$ based FETs for harmful gases.[48,149]

5.2. Photocurrent Transients

Transient measurements without an applied gate voltage are shown in this section with lasers modulated manually in ambient conditions. Transient data with the 685 nm laser returned expected results, with an increase in current under illumination from standard photocurrent generation mechanisms described in Chapter 3. Recordings with higher energy lasers, 473, 514 and 561 nm caused an initial rise in current from illumination, followed by a decay which is fitted by a double exponential in a similar way to the transient measurements from Chapter 4.

The thickness dependence and wavelength dependence of the photocurrent decay is verified by completing transient measurements on FET devices having $MoTe_2$ flake thicknesses between two and fourteen layers. Due to the double exponential fit of the decay and theoretical work in Section 4.5.2, the believed mechanism for the photocurrent decay involves the perturbation of the trap state density through photo-desorption of adsorbates on the surface of $MoTe_2$.

5.2.1. Wavelength Dependence of Photo-Desorption Effects

In this section, transient photocurrent measurements using 473, 514, 561 and 685 nm lasers are performed on a four-layer $MoTe_2$ FET device. Different wavelengths affect the photo-desorption in $MoTe_2$ differently, depending on the energy of photons in the laser. With the 685 nm laser, the photocurrent transient shows photocurrent being generated quickly due to band-bending at the metal contact/$MoTe_2$ interface due to the increase of excited carriers in the $MoTe_2$, described previously in Chapter 3. The photocurrent transient result with the 685 nm laser at 0.2 μW is shown in Figure 5.1.

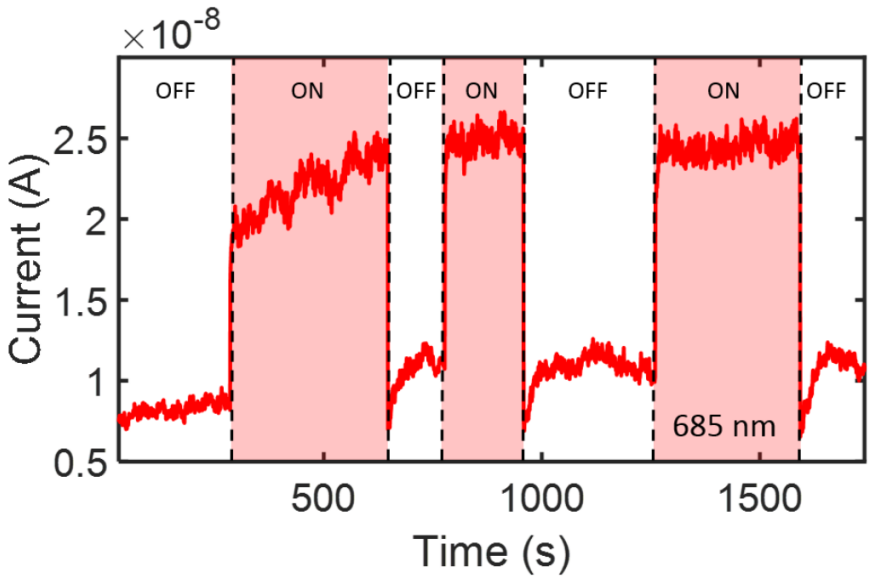

Figure 5.1: *Photocurrent transient measurement with the 685 nm laser on a four-layer $MoTe_2$ FET. V_{ds} = 5 V, V_g = 0 V.*

From Figure 5.1, laser illumination produces an immediate photocurrent of 10 nA, which then slowly increases to 15 nA. This increase of 5 nA is here explained as being due to transient emission effects from trap states, as described in Chapter 4, as it is not observed in the second or third laser ON segments. Indeed, the photocurrent in the second and third segments is stable and does not decay, in line with the results and discussions in Chapter 3 where it was shown that $MoTe_2$ FETs operate quickly and sensitively to the 685 nm laser.

The transient measurements using the three higher energy lasers are however somewhat different, as shown in Figure 5.2. With the 473, 514 and 561 nm lasers, an initial and relatively rapid increase of photocurrent, here of between 15 and 20 nA, is observed, followed by a slower decay. Transient measurements are fitted to a double exponential in the same manner as electrical transients in Chapter 4, with exponential fits shown in Figure 5.2. It can also be seen that the 473 nm transient (Figure 5.2(a)) shows the fastest decrease in current, with 561 nm showing the slowest characteristic (Figure 5.2(c)). The behaviour is repeatable over many scans on the same device, as revealed by the second ON illumination period of the 514 and 561 nm results (Figure 5.2(b) and Figure 5.2(c)).

Figure 5.2 also reveals that when the laser is turned off, the current initially drops (here by around 10 nA in all cases), then a slow exponential increase of current occurs, having a time constant of around 500 s and restoring the $\mathbf{I_{ds}}$ to a similar value as before the illumination.

It is also noted that, in the case of the 473 and 514 nm measurements, a net negative current is observed (i.e. the 'final' photocurrent is lower with the laser ON compared to the laser OFF) whereas in the 561 nm case there is almost no difference in the 'final' photocurrent values, indicating a wavelength dependent nature of the photo-desorption mechanism.

Finally in this section, it is noted that while some previous optoelectronics studies on $MoTe_2$ have used similar wavelengths to those described above and not reported photo-desorption effects, such studies invariably used rather low power densities (~250 mW/cm^2)[79,82,105] that are not expected to show the photo-desorption mechanism on reasonable timescales. For the transient measurements in this chapter, however, a much higher power density of 8800 mW/cm^2 was used.

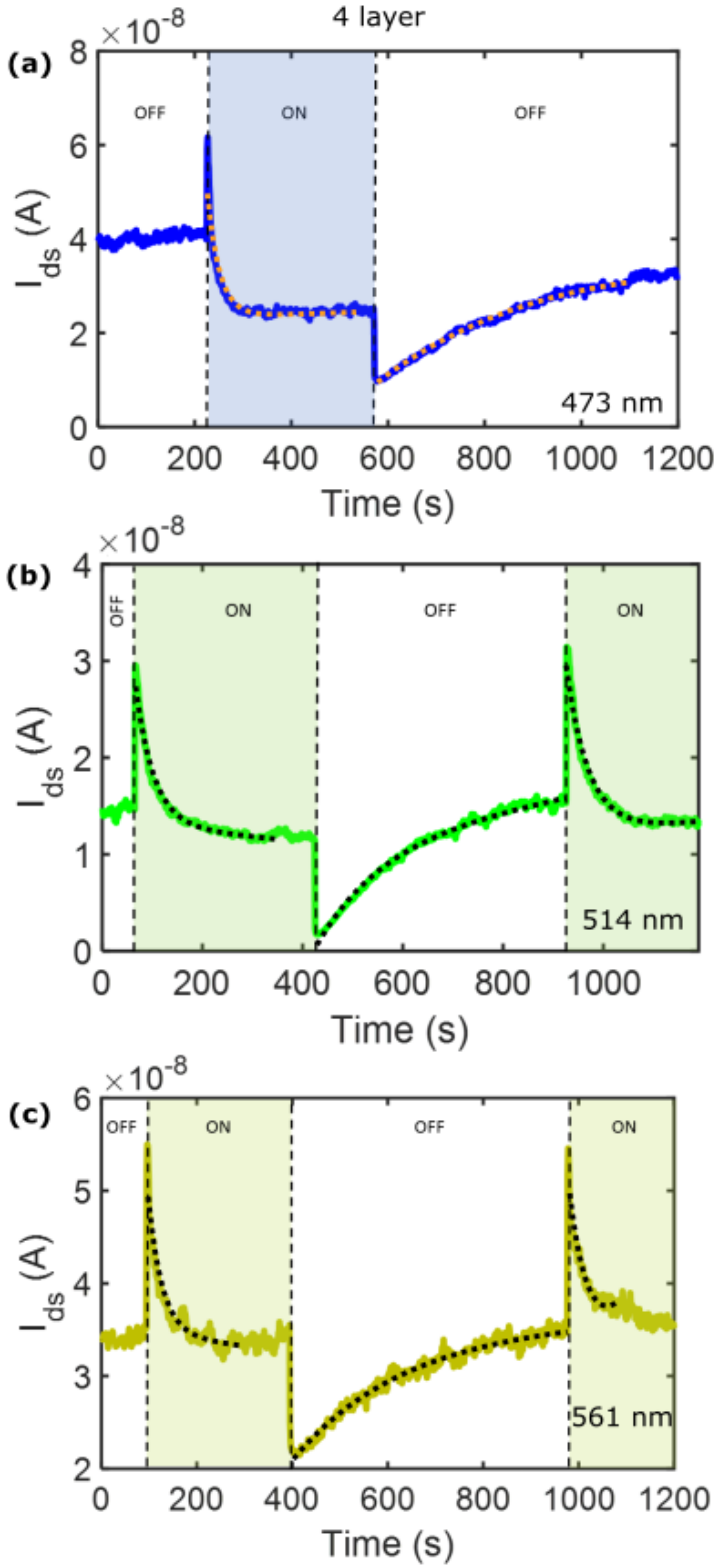

Figure 5.2: *Photocurrent transients of a $MoTe_2$ FET fabricated using a 4-layer flake at V_{ds} = 5 V, V_g = 0 V and at (a) 473 nm, (b) 514 nm and (c) 561 nm. Finely dashed lines in all figures represent the double exponential fit for transient rise and decay of current.*

5.2.2. Dependence of Photo-Desorption on $MoTe_2$ Flake Thickness

The thickness dependence of the photocurrent transients was investigated, by using FET devices fabricated with flake thicknesses between 2 and 14 layers. Thinner flakes were more strongly affected by photo-desorption, possibly as they have lower carrier densities than the thicker flake devices.

The photocurrent transients for the two-layer flake are shown in Figure 5.3. For all three wavelengths, the two-layer device showed an initial increase followed by a decay of photocurrent with the laser being turned on (note that the laser modulation was in this measurement of a shorter period than that used for the results of Figure 5.2). After the initial on/off cycle of the laser, the second on/off cycle produces spikes of photocurrent that are not as prominent, as this device has not recovered all the lost adsorbates back in to the channel. The trend with wavelength for the two-layer device of Figure 5.3 is the same as for the four-layer case of Figure 5.2, with the 473 nm laser causing the fastest decay of current and the 561 nm the slowest. A summary of the decay times with respect to thickness and wavelength are shown in Table 5.1.

The response, shown in Figure 5.4, of the eight-layer flake device is different to the two previous cases above, with only the 473 nm light causes the transient measurement to lead to an overall decay in the current Transients with the 514 and 561 nm lasers show little change in current during the on/off cycles, similar to the measurement carried out at 685 nm and shown in Figure 5.1. This is thought to be because the thicker, eight-layer flake is not as heavily dependent on adsorbates for its conductivity. Thicker $MoTe_2$ flakes may also require higher power densities to remove adsorbates such as water and oxygen molecules. Indeed, reported studies using $MoTe_2$ as a chemical sensor thus far have used thinner flakes to obtain effective photo-desorption.[48,90,149] Thus, the properties of devices fabricated with thicker $MoTe_2$ layers are expected to be less strongly determined by environmental conditions, making them more stable in ambient conditions for optoelectronics applications, but making them less suitable for devices that rely heavily on photo-desorption, such as chemical sensors.

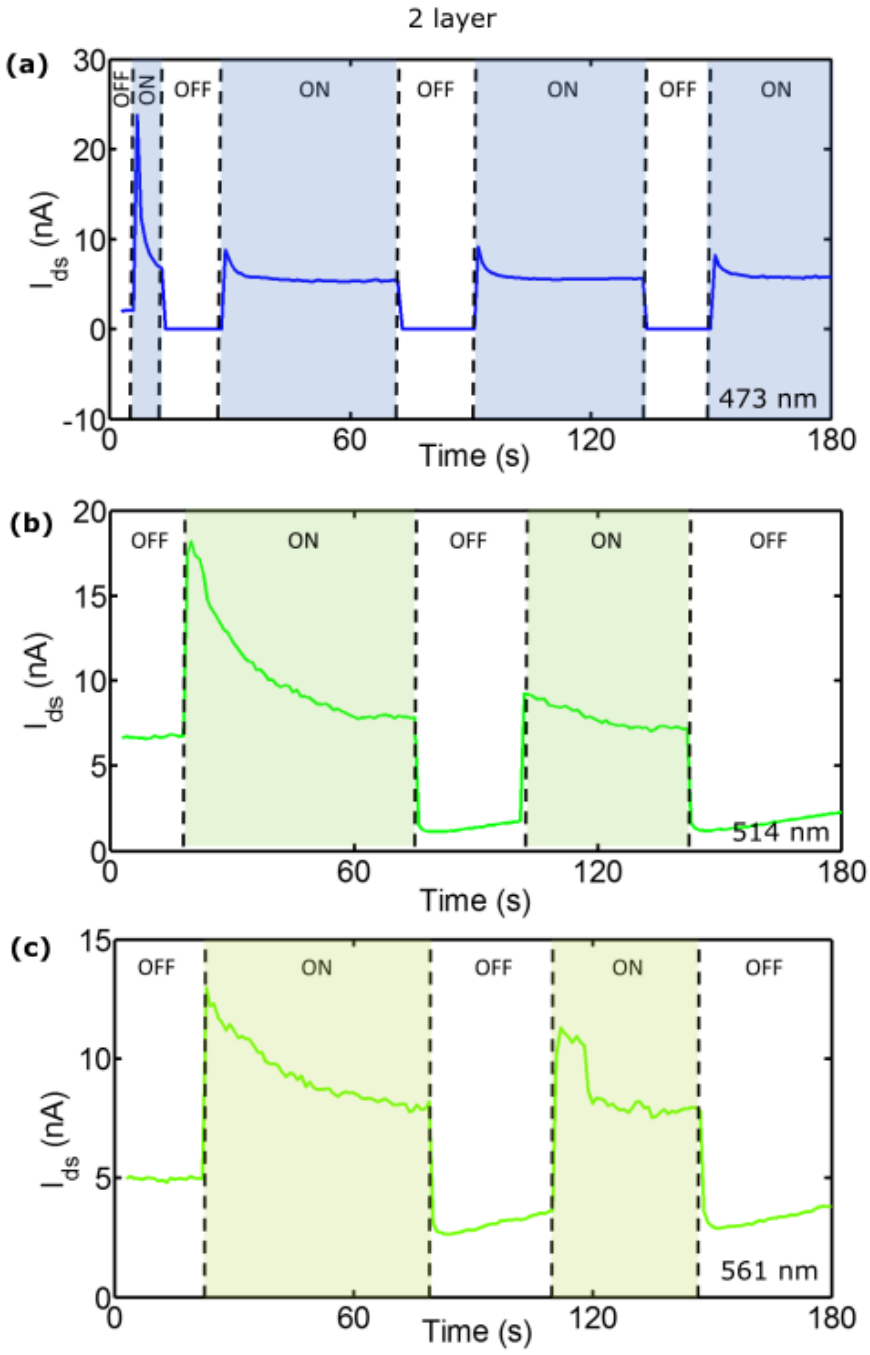

Figure 5.3: *Photocurrent transients of an $MoTe_2$ FET fabricated using a 2-layer flake at V_{ds} = 5 V, V_g = 0 V and at the wavelengths of (a) 473 nm, (b) 514 nm and (c) 561 nm.*

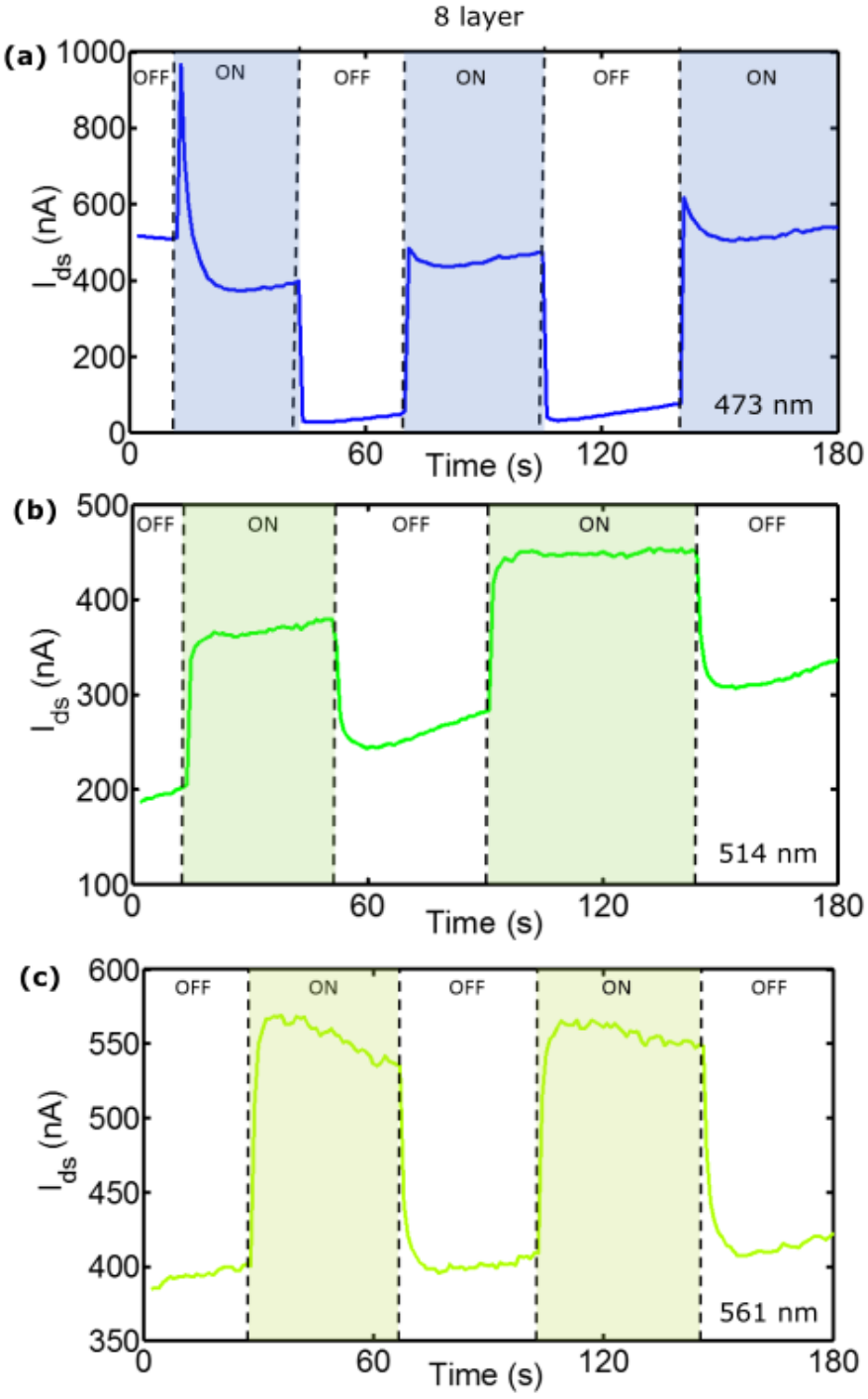

Figure 5.4: *Photocurrent transients of an $MoTe_2$ FET fabricated using an 8-layer flake at V_{ds} = 5 V, V_g = 0 V and at the wavelengths of (a) 473 nm, (b) 514 nm and (c) 561 nm.*

5.2.3. Summary of Transient Photocurrent Results

Transient photocurrent decays observed above were fitted with double exponential, in a similar manner to the results in Chapter 4. In Table 5.1, the double exponential fit coefficients are shown for all the transient decays. Data for the 2- and 4-layer flake devices is present for all three wavelengths of laser, but the 8- and 14-layer devices do not shown appreciable decay for the 514 and 561 nm lasers (so fits at those wavelengths not attempted for these devices)

It can be seen from Table 5.1 that the first exponential coefficient is of greater importance in all cases, with magnitudes up to 100 times larger for $\mathbf{A_1}$ over $\mathbf{A_2}$. The time constants for the decay are also much shorter for $\boldsymbol{\tau_1}$, so it is clear that the first exponential describes most of the decay in these devices.

Thickness	Wavelength (nm)	A_1 (A)	τ_1 (s)	A_2 (A)	τ_2 (s)
2	473	3.79E-09	7	1.72E-10	970
2	514	1.45E-08	17	3.05E-09	-380
2	561	3.00E-09	15	1.82E-09	500
4	473	3.50E-07	15	2.38E-09	5400
4	514	3.60E-08	36	5.60E-09	2000
4	561	1.27E-07	30	1.17E-08	4700
8	473	4.31E-07	3	9.48E-09	-240
14	473	2.72E-07	6	1.72E-10	570

Table 5.1: *Table summarising the double exponential fit for the transient decays in the photocurrent for $MoTe_2$ FET devices fabricated using a range of flake thicknesses and for various illumination wavelengths.*

Values for $\boldsymbol{\tau_2}$ in Table 5.1 are large (~500 – 5000 s), with a similar order of magnitude to the time constants displayed in Chapter 4 for transient current decay. In two cases, $\boldsymbol{\tau_2}$ is negative, however transient measurements were taken over time scales much shorter than $\boldsymbol{\tau_2}$, except measurements taken with the four-layer flake. The uncertainty in measurements of $\boldsymbol{\tau_2}$ for the two, eight and fourteen-layer flakes is larger than uncertainty for the four-layer flake measurements, which may be responsible for the negative values of $\boldsymbol{\tau_2}$ shown in Table 5.1. Measurements taken with the four-layer flake over the longer time period of one hour are the best indicators of values for $\boldsymbol{\tau_2}$ for all transient measurements taken. Values of $\boldsymbol{\tau_2}$ found for the photocurrent decay of the four-layer flake reach between 2000 s and 5400 s, the same order of magnitude as for the deep traps observed in Chapter 4. From observing values for the time constants for $\boldsymbol{\tau_2}$, and the knowledge on trap states from Chapter 4, it is inferred that the origin of shallow traps identified in Chapter 4 are removed from the surface of the $MoTe_2$ with the high energy, visible wavelength photons. The origin of the shallow traps is believed to be adsorbates, whereas deep traps are intrinsic to $MoTe_2$, potentially stemming from Te vacancies prevalent in $MoTe_2$.

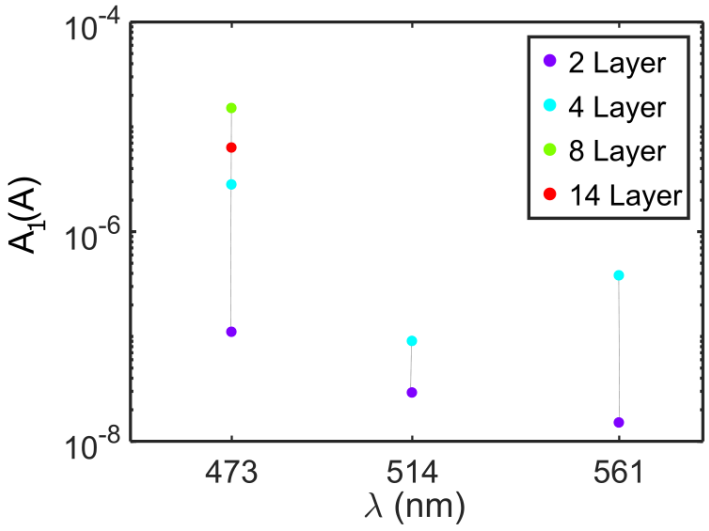

Figure 5.5: *Data from Table 5.1 of A_1 against the incident wavelength for all devices. The layer thickness of each result is given in the attached legend.*

In Figure 5.5 the decay coefficient $\mathbf{A_1}$ is presented as a function of the wavelength of the incident light for devices with various $MoTe_2$ thicknesses. The decay coefficient shows the largest values for flakes of all thickness when perturbed with the 473 nm laser. There

is a clear trend between the incident wavelength and decay coefficient, showing that the highest energy wavelength promotes stronger photo-desorption in $MoTe_2$. The largest values for the decay coefficient are seen for the thicker (eight and fourteen-layer) flakes as they are more conductive than the few-layer flakes (two and four-layer). The higher conductivity allows for higher decay coefficients as they have higher initial I_{ds} values. Eight-layer flakes are known to show the best conductivities, a result observed by Ji et al.,[89] and from the results on $MoTe_2$ FETs used in this thesis in Section 2.14.

Figure 5.6 provides greater clarity into the importance of the dependence of wavelength for the photo-desorption and photocurrent decay. The 473 nm laser shows an average decay constant of 10 s across all devices, with the measurements at 514 and 561 nm recording higher average decay constants of ~25 s. It appears that the higher energy photons are perturbing $MoTe_2$ more strongly via the photo-desorption mechanism. The mechanism for photo-desorption will be discussed in the following section, including remarks on why the energy of the photons is important for this mechanism to work.

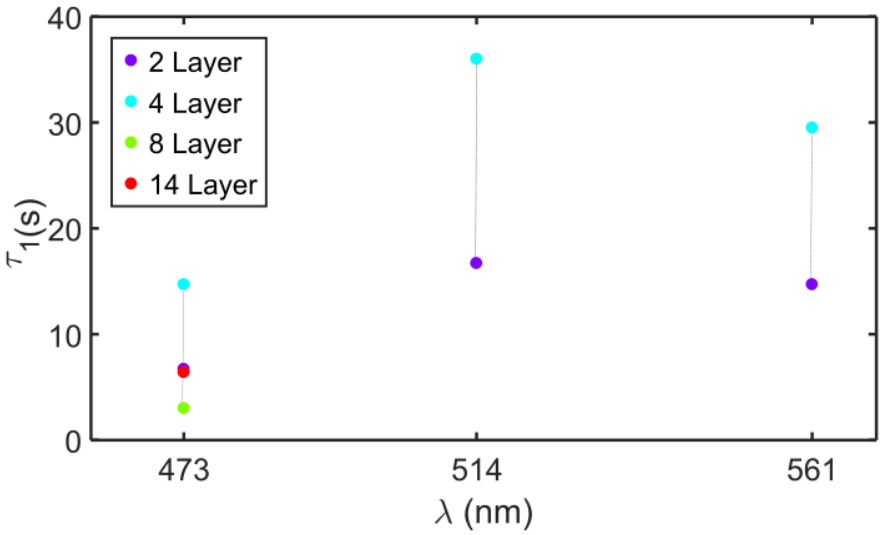

Figure 5.6: *Data from Table 5.1 of values for τ_1 against incident wavelength for all devices, with a legend included to observe thickness dependence on decay constant.*

5.3. Photo-desorption Mechanism for Adsorbates in $MoTe_2$

Research on negative photoconductivity in TMDCs is not often reported, with only two studies commenting on the negative photoconductivity in MoS_2.[150,151] More recently, a study by Wu et al[149] has demonstrated negative photoconductivity in transfer characteristics when exposing $MoTe_2$ to 254 nm, UV light, where decreasing conductivity was seen by affecting the doping in the channel through the removal of oxygen.[149] Negative photoconductivity is more common in high surface area materials, as interaction with light can cause changes in the surface chemistry, such as photo-desorption from hot electrons created by far above band gap photons.[152] Studies of negative photoconductivity on nanowires[153–157] and atomically thin materials[48,151,158] are numerous and depend on the desorption of adsorbates for their mechanisms.

As observed by Chen et al,[159] $MoTe_2$ has defect sites caused by Te deficiencies, which are strongly reactive in air. Binding energies of ~166 meV between the Te deficiency and an O_2 molecule are created, much stronger than those between defect-free $MoTe_2$ and O_2, with a smaller reported binding energy of ~36-64 meV.[159] The larger binding energy at the Te deficiency promotes strong absorption of adsorbates such as O_2, which act as electron acceptors and promote p-type doping,[160] which is seen strongly for all $MoTe_2$ devices in this thesis. From the fact we see strong p-type doping and changes in the threshold voltage from Section 4.2.1, it is clear O_2 and other adsorbates are present on the surface of $MoTe_2$. Chemical sensing applications in $MoTe_2$ use UV light to remove these adsorbates,[90,149] which increases their ability to detect harmful gases such as NO_2, as the surface of $MoTe_2$ is free of adsorbates.

Where the 685 nm wavelength photons do not affect the adsorbed O_2, it is because the energy of the photons is not enough to break the relatively strong Te-O bonds of ~166 meV, so only photocurrent mechanisms highlighted in Chapter 3 from above band gap excitation are observed. However, with the three higher photon energies at 473, 514 and 561 nm, desorption of the O_2 occurs as photons have enough energy to create electrons and holes, with excess thermal energy. The thermally excited holes are attracted to the adsorbates such as O_2, which transfer their energy causing the bonds to break, freeing oxygen from the surface. With $MoTe_2$ in this thesis being strongly p-doped, loss of the electron acceptors such as O_2 causes a decrease in doping and a decrease in the conductivity.

When the $MoTe_2$ is no longer exposed to light in ambient conditions the surface becomes strongly reactive once more, with defect sites attracting adsorbates. The various stages of the photo-desorption mechanism over the entire on/off cycle thus as described pictorially in Figure 5.7, in terms of the 4-layer device illuminated with the 473 nm laser.

The photo-desorption mechanism is highly dependent on the incident wavelength for $MoTe_2$, not observed with the 685 nm laser. Photo-desorption in single-walled carbon nanotubes (SWCNTs) also shows strong wavelength dependence, with higher energy photons promoting photo-desorption.[157] To provide more evidence that the photo-desorption mechanism here does require far above band gap photons, other studies on TMDCs where photocurrent decreases occur are examined, with Khan et al. showing negative photocurrent in an O_2 environment for MoS_2 (1.9 eV) at 220 nm (5.6 eV),[151] and Feng et al. showing negative photocurrent results for $MoTe_2$ (~1 eV) at 254 nm.[48]

Negative photoconductivity is not observed for photocurrent results taken in vacuum conditions, shown in the following chapter, despite using the same photon energies used in this study. In vacuum conditions, adsorbates on the surface of $MoTe_2$ FETs are removed, causing the device to no longer show the photo-desorption mechanism. Interestingly Nowak et al.[155] show that photo-desorption became stronger in higher humidity conditions when using SbSI nanowires, with $MoTe_2$ also showing stronger photo-desorption in the presence of ambient (i.e. higher humidity) conditions.

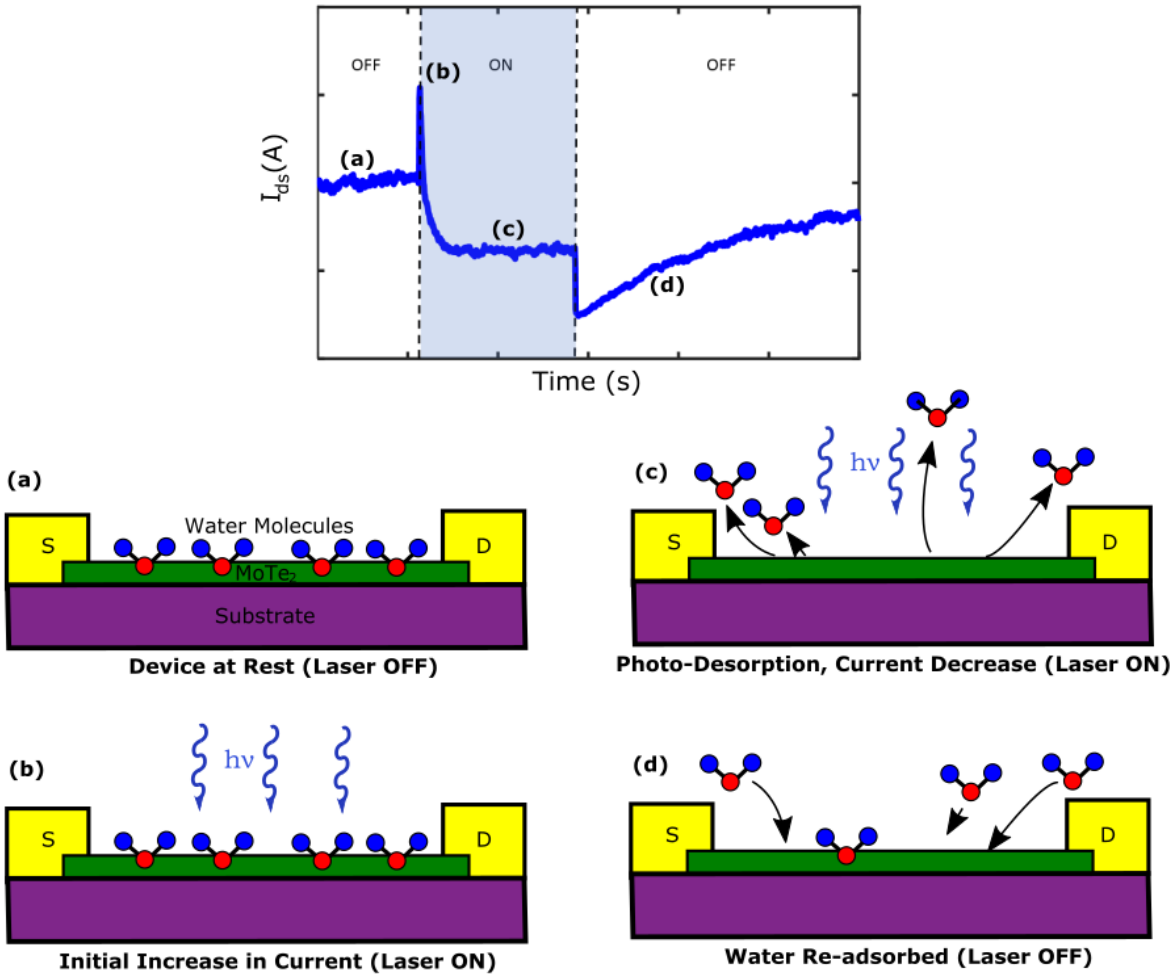

Figure 5.7: *Photo-desorption mechanism in $MoTe_2$. (Top figure) 473 nm transient from 4-layer device used as reference for mechanism during measurement. (a) Device in ambient has adsorbates on surface, contributing to the conductivity. (b) Laser initially turned on, the photons contribute to photo-excitation of carriers, causing sharp increase in photocurrent. (c) As the device is exposed to high energy photons for longer periods, adsorbates are removed due to their weaker binding energies. Decrease in current due to the removal of adsorbates. (d) Laser is turned off, water and other adsorbates return to the $MoTe_2$ surface.*

5.4. Negative Photoconductivity Effects from Transfer Characteristics

Finally in this chapter $MoTe_2$ FET transfer characteristics are investigated for four wavelengths: 473, 514, 561 and 685 nm, to show any effect of wavelength on the transfer characteristics. As already discussed, the higher energy lasers remove adsorbates, leading to a reduction in the p-type field effect mobility of $MoTe_2$. An incident power of $5x10^4$ mW/cm^2 was used for all the illuminated transfer characteristics presented here.

In Figure 5.8 the transfer characteristics are shown for the four aforementioned wavelengths. There is a clear wavelength dependence on the field-effect mobility ($\boldsymbol{\mu_{FE}}$), (extracted from the gradient $\left(\frac{\mathbf{\Delta I_{ds}}}{\mathbf{\Delta V_g}}\right)$ in the ON state of the $MoTe_2$ FET) of all sweeps, with 473 nm causing the greatest reduction in the photocurrent, as it more strongly removes the p-type donor adsorbates. Work by Khan et al[151] shows similar results using MoS_2 FETs measured in O_2 gas, also experiencing a decrease in mobility under UV light from the removal of p-type donors such as O_2.

The mobility is highly dependent upon incident wavelength. Mobility in the dark is 1.11 cm^2/Vs, and with the 685 nm laser the mobility increases to 1.50 cm^2/Vs, due to the increased number of photo-excited carriers increasing the conductivity of the device. There is a clear increase in the photocurrent due to a shift in the threshold voltage using the 685 nm laser, as already seen in Chapter 3; this is from the photogating effect seen in TMDCs. The mobility from the higher energy sources are 1.06 cm^2/Vs for the 561 nm, 0.88 cm^2/Vs for the 514 nm and 0.56 cm^2/Vs with the 473 nm laser.

From Figure 5.8 it is clear that in all three of the higher photon energy (473, 514, 561 nm) transfer characteristics, there is an intercept between the dark and illuminated measurements at $\mathbf{V_g}$ = -27 V. There is no clear shift in the threshold voltage seen from the photogating effect using the higher energy photons (473, 514, 561 nm), due to the photo-desorption of adsorbates which are the cause of the photogating mechanism. With the removal of adsorbates, the source of the trapped charge carriers which behave as an effective gate are no longer available to shift the threshold voltage.

Despite the decrease in current in the ON state, the OFF state shows the reverse, with all lasers increasing the photocurrent. This increase is also wavelength dependent, with 473 nm creating the greatest increase. For the higher energy photons of the 473 nm laser, the electron-hole pairs generated have higher energy than those generated by the other wavelengths and so carriers more easily tunnel through the Schottky barrier and create a higher OFF current.

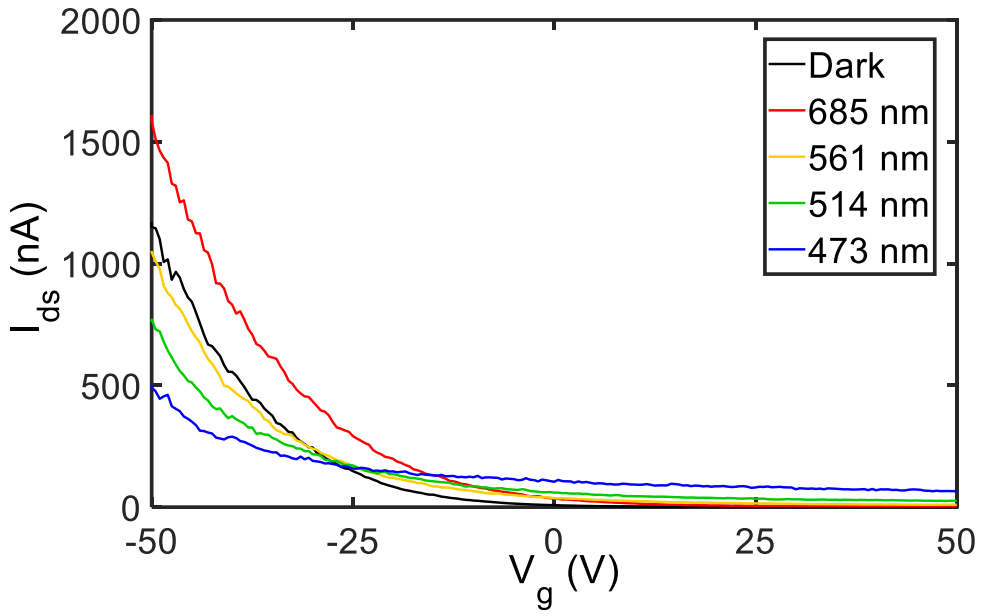

Figure 5.8: *$MoTe_2$ FET characteristics for all four wavelengths and in the dark. (V_{ds} = 5 V). Only the 685 nm laser increases the current in the ON state due to the lack of photo-desorption.*

The photo-desorption mechanism occurs on the order of a 10 s time constant, modulating the laser during a gate sweep at rates much faster than the decay constant can be used to show an increase in the photocurrent, as the photocurrent generation mechanisms stay the same when the adsorbates are present. In Figure 5.9 the transfer characteristic is shown for the case with the laser modulated manually for no longer than 3 s at a time, showing that the negative photocurrent is not observed as the photo-desorption occurs on a slower time scale than the laser modulation itself.

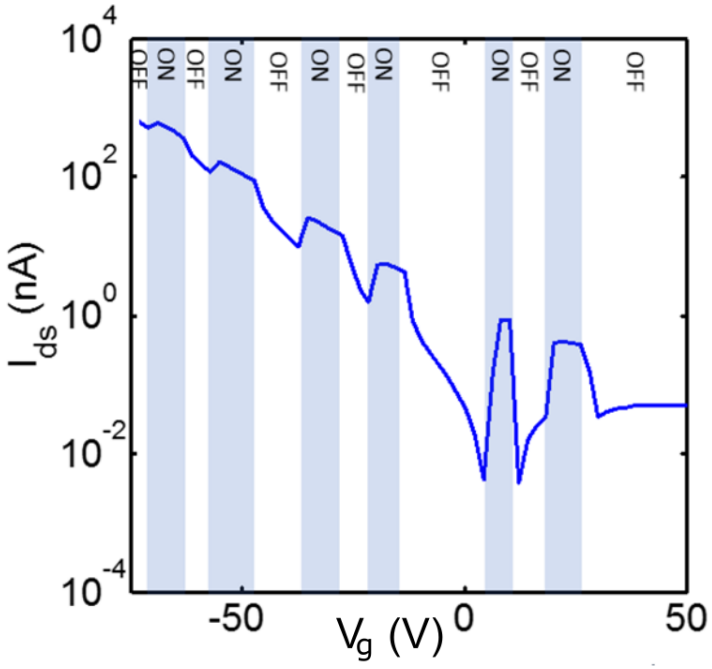

Figure 5.9: Transfer characteristic with relatively fast modulation of the 473 nm during the measurement, showing a complete lack of negative photoconductivity.

5.5. Conclusion

The photo-desorption of adsorbates from the surface of $MoTe_2$ FET devices has been examined with high energy, visible light photons. Such high energy photons are required due to the prevalence of Te vacancies which strongly attract O_2 to form relatively strong Te-O bonds. The bonded oxygen is removed with the creation of charge carriers via the photovoltaic effect, with the excess energy of charge carriers being used to remove adsorbates from the surface. A negative photoconductivity is observed for transient photocurrent measurements with the highest energy laser used (λ = 473 nm), and correlation between the wavelength and the layer thickness with photo-desorption is shown, with thinner flakes at higher photon energies more strongly affected by photo-desorption. Transfer characteristics with high energy photons did not show the photogating photocurrent mechanism, observed with measurements using the lower energy 685 nm photons, as the sources of trap states were removed in photo-desorption. Deeper traps explored in Chapter 4 remain unaffected by photo-desorption process, showing that adsorbates are responsible only for shallow trap states in $MoTe_2$. In future, photocurrent transient measurements of $MoTe_2$ could be completed in different

environments, such as in small concentrations of harmful gases or a humidity controlled surrounding. $MoTe_2$ continues to show interesting properties in comparison to other TMDCs due to Te deficiencies which strongly affect its characteristics.

6. Layer-by-Layer Laser-Thinned $MoTe_2$

6.1. Introduction

While $MoTe_2$ and other TMDCs are interesting materials to research in optoelectronic devices, methods of creating samples to the desired number of layers are limited in scope. Mechanical exfoliation is not a dependable method of obtaining wanted flake thicknesses, although is commonly used for research purposes it tends to produce flakes having random areas and thicknesses. While other methods of creating samples, such as chemical vapour deposition, have been shown to work well for a number of TMDCs[161,162], $MoTe_2$ is more challenging due to the inherent weakness of its Mo-Te bond (due to the small difference in electronegativity[53]) making it difficult to create precise, user-defined thicknesses in $MoTe_2$.[41,53,55]

In this chapter, therefore, two methods suitable for laser thinning of $MoTe_2$ are developed, each exploiting a different physical mechanism. One technique, has been demonstrated before for MoS_2,[163–165] and involves thinning a flake directly to monolayer thickness through an increase of temperature. The second technique, an entirely novel and previously unreported approach, provides a controllable method for thinning $MoTe_2$ to any desired thickness by removal of a single layer at a time. This unique thinning procedure is highly dependent upon environmental humidity and can be achieved at much lower power densities than previous TMDC thinning methods. Moreover, it offers many advantages over previous top-down techniques used to control the thickness of TMDCs such as chemical,[166] thermal[167] and plasma[168] methods, as it is a simple method, with low-cost and can be used to selectively thin without a lithographic process. In addition, compared to other thinning processes which invariably have detrimental effects on the surface roughness, the layer-by-layer humidity-assisted thinning process reported in this chapter is shown to even reduce the surface roughness. A full material characterization including Raman, AFM and PL spectroscopy is used to identify any changes between the thinned and pristine $MoTe_2$.

To make sure this new, unique, thinning procedure has no adverse effect on $MoTe_2$, thinned monolayers of $MoTe_2$ and layer-by-layer thinned devices are tested optoelectronically in FET configurations as photodetectors, and compared to pristine $MoTe_2$. These thinned devices show a fast photoresponse, relatively high photoresponsivity, and enhancements in the field effect mobility, even in the case of monolayer $MoTe_2$ which has relatively poor electrical properties.[74] Furthermore, by thinning the channel area only, leaving multi-layer $MoTe_2$ at the $MoTe_2$/metal contact interface, monolayer $MoTe_2$ channels show great potential for optoelectronics applications.

6.2. Laser Thinning Methodologies and Mechanisms

The two thinning procedures, bulk to monolayer and layer-by-layer, have their methodologies and thinning mechanisms outlined in this section. The two methodologies function through different mechanisms, with the layer-by-layer technique dependent on the humidity in which the samples are thinned and requiring very low laser power densities. The bulk to monolayer process works through the well-known temperature increase methods seen in literature already for various TMDCs,[163–165] leading to sublimation of all but the bottom layer of $MoTe_2$.

Laser-thinning here is performed in the Raman system (AIST-NT, Horiba Jobin-Yvon Xplora) in ambient conditions, which has the advantage of allowing the flake thickness to be monitored (by Raman spectrum) in-situ. The system uses continuous wave excitation at 532 and 618 nm, although the 532 nm was used for a majority of results reported here. The optical spot size in the Raman system is around 0.5 μm (for the 0.9 NA objective used), and a xyz motorized stage automates the raster scanning to generate a desired area of thinned flake. Raman spectral maps of thinned regions were taken at lower power density (i.e. lower than the power for thinning) to show the uniformity and quality of thinned flakes. To control the humidity, the Raman system was placed inside a controlled chamber at standard room temperature and pressure, with the humidity being varied between 30 and 90% using an in-chamber humidifier.

6.2.1. Bulk to Monolayer Photothermal Thinning

Flakes of $MoTe_2$ of any thickness can be thinned using laser ablation by using high power densities of around >10mW/μm^2 for TMDCs on SiO_2 substrates (i.e. Si substrates with an SiO_2 layer on top)[164,165]. In this method, the temperature increase from the incident laser causes the ablation of the top layers of $MoTe_2$ leaving only the bottom layer of the TMDC. The bottom layer of the TMDC survives the treatment due to the substrate, with the SiO_2 acting as a natural heat sink, lowering the effective temperature experienced by the $MoTe_2$ in direct contact with the SiO_2 layer.[165] Thinning on other substrates has however proved to be more difficult from our own experience, particularly in cases such as quartz which acts as an even more effective heat sink compared to SiO_2. However, through calibration of the method using different power densities and exposure times it should be possible to thin $MoTe_2$ on any substrate.

For the straight to monolayer thinning the laser power was set to 2 mW, far above that used for Raman spectra acquisition (typically 20 to 30 μW) and for photocurrent measurements (0.4 to 26 μW). The humidity for this thinning method is not monitored or relevant, since the mechanism is independent of humidity, relying purely on increasing the temperature (the estimated temperature increase induced is ~650 K, as estimated by Cho et al.[27]). The areal rate of thinning achieved was around 5 μm^2 per minute, limited mainly by the scanning speed of the sample stage.

An example of the effect of bulk to monolayer thinning is shown in Figure 6.1, where flakes pinned down by Cr/Au contacts are thinned through this method. The initially tri-layer flakes are thinned down to monolayer thickness, as confirmed by their optical contrast and Raman spectra. Note that the thinned devices do not show any damage or stress in the optical microscopy image, despite the large central blue flake showing some degradation after the thinning procedure.

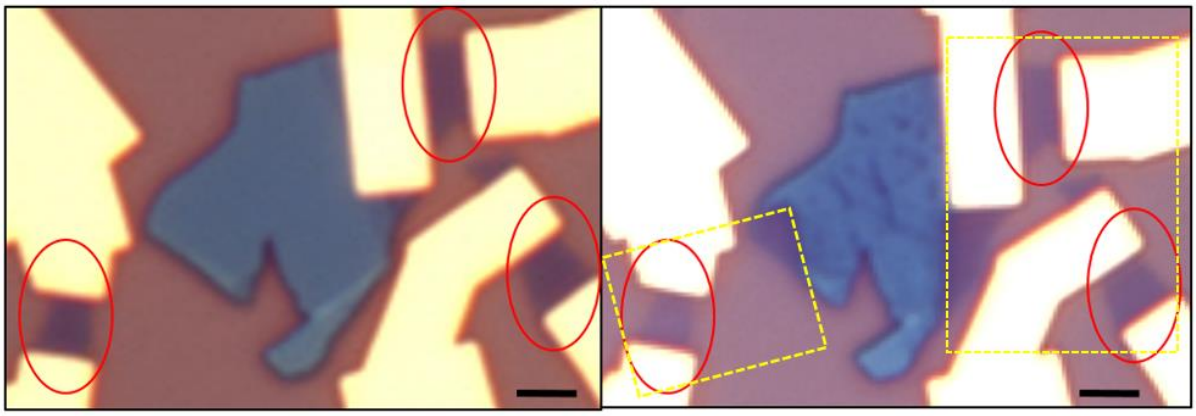

Figure 6.1: *$MoTe_2$ flakes thinned from a tri-layer to monolayer with a 2 mW laser power. Thinned tri-layer devices are highlighted by red rings. The dashed yellow boxes indicate the laser-thinning treatment area. Scale bar in black is 2 μm.*

6.2.2. Layer-by-Layer Thinning

By utilizing lower laser powers and by increasing the relative humidity in the Raman system chamber, it was found that flakes of $MoTe_2$ could be thinned by a single layer at a time. Instead of temperature increases causing sublimation, a different method involving the presence of surface water on the $MoTe_2$ and photon absorption results in the $MoTe_2$ being reliably thinned under certain conditions. The physical mechanisms responsible for this process are discussed in this section, after introducing the methodology for thinning.

To test the requirement for humidity in the thinning mechanism, humidity is separated into 3 different regimes of relative humidity (RH) between 20–40%, 40-60% and 60-80%. In Figure 6.2 the incident laser power density is modulated for a five-layer flake of $MoTe_2$ to see the effect of the three regimes of RH for the thinning response. Flake thicknesses were measured after the applied power density by Raman spectroscopy (at a much reduced laser power density to prevent any interference with the thinning result). Four power densities were used as shown in Figure 6.2 (with lines between points used only to show trends).

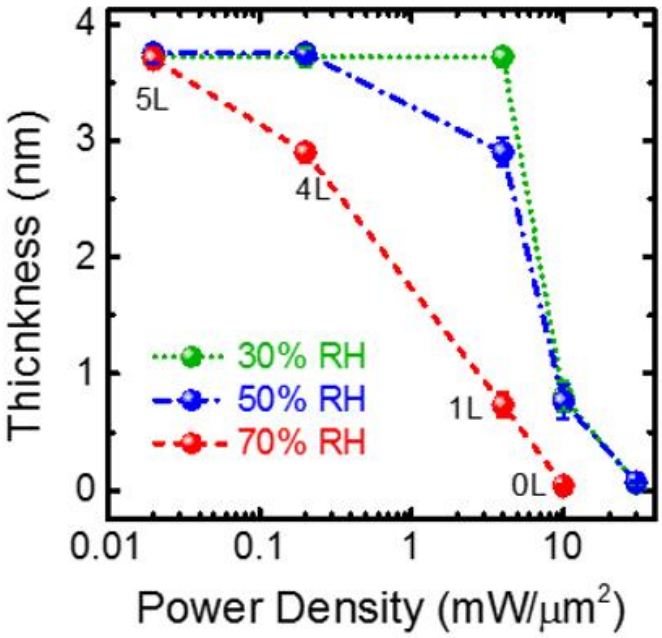

***Figure 6.2**: Graph showing $MoTe_2$ flake thickness changing with laser power density at three different relative humidity values. At the highest humidity value, thinning appears more controllable and thinning to a single layer requires the smallest power density.*

The plot in Figure 6.2 shows that at the lowest RH regime (20-40%), the five-layer flake is unaffected by the laser for power densities up to 4 mW/μm², then is suddenly thinned down to a monolayer when a power density of 10 mW/μm² is used. The intermediate RH regime (40-60%) shows greater thickness control at lower laser powers, ≥ 4 mW/μm². At the highest RH regime (60-80%), an exceptionally low power of just 0.2 mW/μm² is able to thin the five-layer flake down to a four-layer flake. Subsequent scans at this RH regime using the same laser power were used to obtain a bi-layer flake of $MoTe_2$ (see Figure 6.3 and associated discussion). To obtain a monolayer from this bi-layer, a higher power of 4 mW/μm² was required to overcome the heatsink effect from the SiO_2 substrate. Illumination with a laser power of 10 mW/μm² then resulted in complete ablation of the $MoTe_2$ from the substrate. Optical microscope and AFM images of the five-layer flake during each stage of the 5-cycle thinning process described above are shown in Figure 6.3. Interestingly the AFM images in Figure 6.3 reveal that the surface morphology is shown to lose many of the defects observed for the pristine flake, showing the this new layer-by-layer thinning technique can be used to remove adsorbates from

the surface of $MoTe_2$. Note that Raman spectra and Photoluminescence (PL) measurements on thinned samples will be shown later in this chapter (Section 6.3).

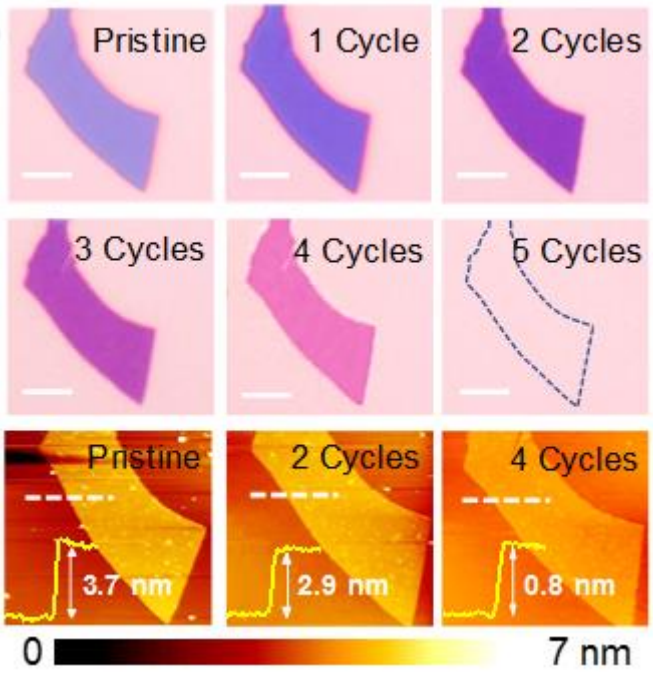

Figure 6.3: *5-layer $MoTe_2$ flake being thinned layer by layer, with optical microscope images being shown after each thinning cycle (top two rows). AFM images of the pristine flake and after 2 and 4 cycles are also shown (bottom row) to provide further proof of the layer-by-layer thinning method, with step heights shown along the dashed white line in the AFM image correlating with expected layer thickness.*

The proposed mechanism for this layer-by-layer process is described in the following section, along with discussion on whether or not the method is possible from only the increased temperature of the sample and if the flake is oxidised in the process.

6.2.3. Mechanisms Responsible for the Layer-By-Layer Humidity-Assisted Thinning Process

With the low laser power densities used in this layer-by-layer thinning method along with the high dependence upon RH, the standard laser-thinning thermal ablation mechanism is discounted as being the cause of thinning. Instead, a photochemical etching method is theorized to remove just a single layer at a time, with help from the increased presence of water and other adsorbates. $MoTe_2$ itself reacts readily with oxygen in ambient

conditions,[114,159] with the photocurrent results from Chapters 3 and 5, along with the transient measurements in Chapter 4 all relying upon the trap states garnered from O_2 and other adsorbates. For these reasons, $MoTe_2$ is a viable candidate for etching through photochemical methods. Photochemical and photothermal etching effects have been seen for atomically thin materials before, such as in graphene,[169] TMDCs[170] and interestingly photochemical thinning has been used as a technique to selectively etch GaAs based on doping levels.[171]

The basic photochemical process at play during the layer-by-layer thinning of $MoTe_2$ is postulated to be as shown in Figure 6.4. The absorption of photons breaks chemical bonds in the presence of the reactant species, H_2O and O_2. At the high RH values, H_2O occupies all available sites on $MoTe_2$, resulting in a continuous layer of water on the surface as shown by Figure 6.4(b). Since low power densities of 0.2 mW/μm^2 are used with the 532 nm laser, it is speculated here that photons are absorbed non-linearly, leading to an increase in the concentration of photogenerated free carriers in the $MoTe_2$.[169,172] (Indeed, a recent article by De Sanctis et al.[173] on a similarly volatile TMDC, HfS_2,[174] shows how free radicals are generated from the presence of water in the form of OH^- and O^- with the interaction of incident photons[173]), The highly reactive OH^- and O^- radicals react strongly with the $MoTe_2$, able to overcome the relatively weak covalent Mo-Te bonds in a photochemical decomposition, as shown in Figure 6.4(c). After a single-raster scan to remove one layer, by the time the second scan occurs (5 minutes later in these results), the underlying layer is exposed to high humidity for a long enough time, depicted in Figure 6.4(d), allowing the following layer to be thinned by the same method.

To provide some experimental proof that the layer-by-layer thinning process is not driven by photothermal effects, and that it does not result in oxidation of the $MoTe_2$ layer, Raman spectroscopy was used, as described in the follow sections.

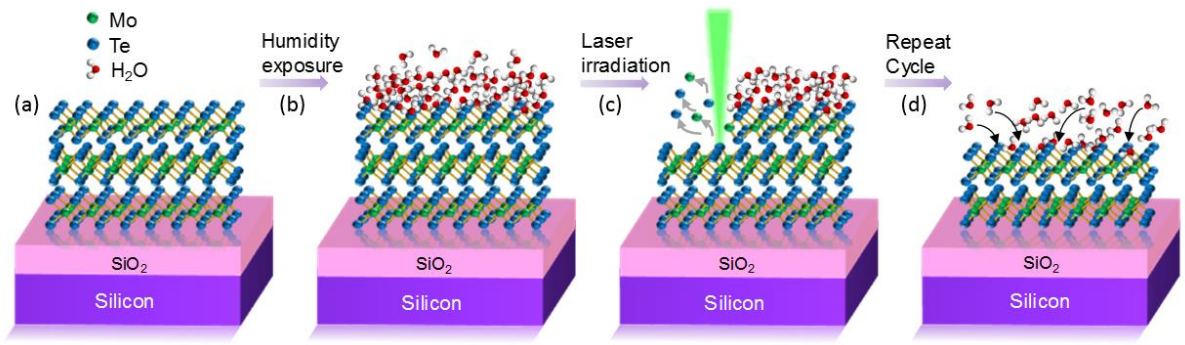

Figure 6.4: *Schematic of the proposed photochemical mechanism responsible for layer-by-layer thinning of $MoTe_2$ in the presence of high relative humidity.*

6.2.3.1. Estimating Temperature Change during Layer-by-Layer Thinning

Any increase in temperature during thinning of $MoTe_2$ as described above can be estimated from the temperature-induced shifting of Raman peaks for the sample. Indeed, we find that the temperature increase going from 3 to 2 layers is only around 100 K (see Figure 6.5),[175] far lower than that suggested as being required for photothermal thinning (~ 400 to 625 K, see Cho et al.[27]).

Figure 6.5 shows the two strongest Raman peaks for $MoTe_2$ before, during and after thinning (here from 3 to 3 layers). The equation $\boldsymbol{\chi_T = \Delta\omega/\Delta T}$ is used to estimate the temperature increases from the Raman shifts, where $\boldsymbol{\chi_T}$ is the first order temperature coefficient of the respective Raman mode, $\boldsymbol{\Delta\omega}$ is the change in frequency of the Raman peak position and $\boldsymbol{\Delta T}$ is the change in temperature of the flake.[175] The first order temperature coefficients of $MoTe_2$ are taken as -0.0117.5 cm^{-1}/K ($\mathbf{E^1_{2g}}$) and -0.0161 cm^{-1}/K ($\mathbf{B^1_{2g}}$) by using the average of the bi and tri layer coefficients.[176] The observed redshifts for the $\mathbf{E^1_{2g}}$ and $\mathbf{B^1_{2g}}$ peaks shown in Figure 6.5 are 1.2 cm^{-1} and 1.4 cm^{-1} respectively, leading to an approximate temperature increase of ~95 K. Thermal sublimation occurs at a much higher temperature, around 650 K,[27] so the results of Figure 6.5 provide fairly strong evidence that the layer-by-layer thinning process is not photothermal in origin.

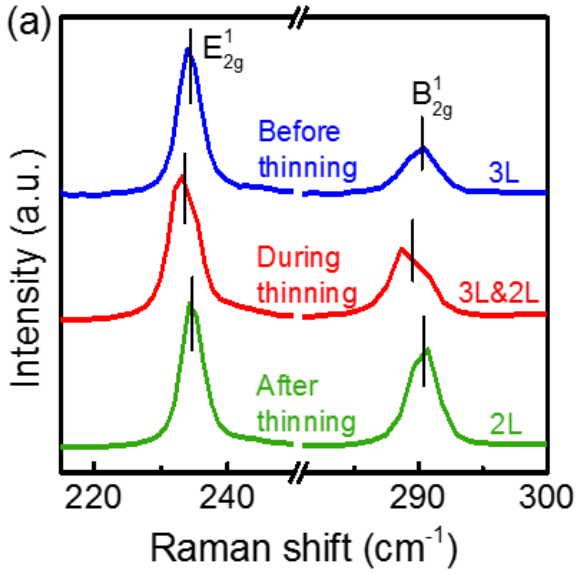

Figure 6.5: *Raman spectra before, during and after the layer-by-layer thinning method for a flake between 3 and 2 layers. These spectra are used to estimate the change in temperature during the thinning process by examining redshift of the peaks during the thinning.*

6.2.3.2. Lack of Oxidation peaks in Raman Spectra for Single Layer Thinned $MoTe_2$

While the thinning does take place in a humidity-controlled chamber, the chamber is still at ambient (atmospheric) conditions, which could lead to some form of oxidation when the flake is experiencing any increase in temperature. To investigate whether oxidation was happening as a result of the layer-by-layer thinning, $MoTe_2$ flakes were deliberately oxidised by heating them on a hot plate, their Raman spectra obtained and compared to those of samples subject to layer-by-layer thinning (and to pristine flakes).The results are shown in Figure 6.6, from which it is clear that the sample is not being oxidised due to the increase in temperature caused by the incident laser during thinning

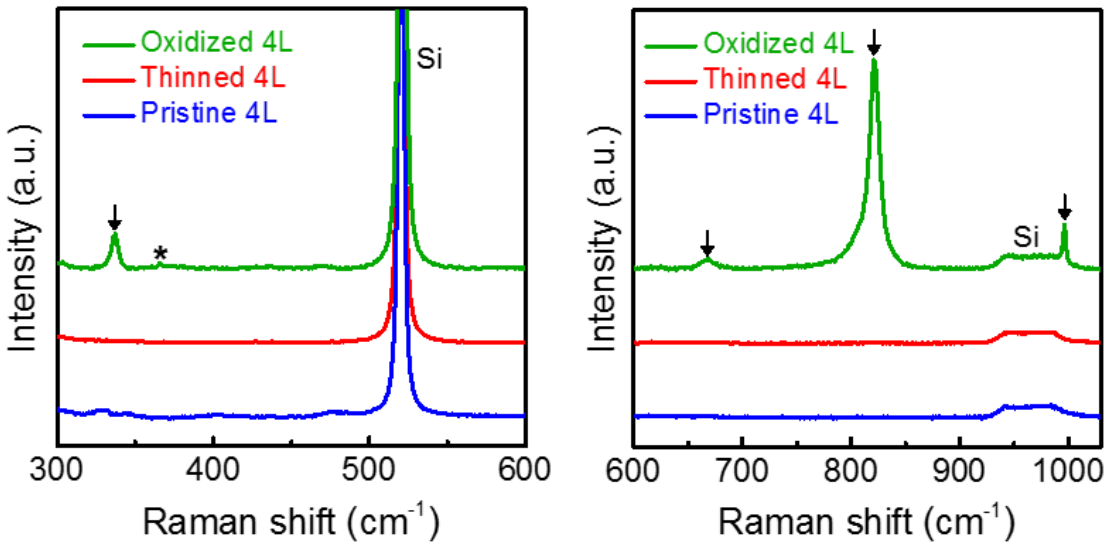

Figure 6.6: *Raman spectra highlighting the oxidation peaks of $MoTe_2$ for deliberately oxidised flakes against pristine and thinned flakes of the same thickness. No oxide peaks are seen for the thinned or pristine $MoTe_2$.*

6.3. Characterization of Thinned and Pristine $MoTe_2$

To ensure the practicality of the layer-by-layer thinning technique, Raman spectra, Atomic force microscopy (AFM) and photoluminescence (PL) measurements were taken, and examined, with comparisons made to pristine samples. Raman measurements showed little change between pristine and thinned flakes and AFM measurements revealed a reduction in the surface roughness, showing the flake surface is cleaned from the thinning technique. PL measurements show similar results (between pristine and thinned flakes) with a slight shift in the peak position due to a change in doping from the laser thinning method.

6.3.1. AFM Characterization

AFM measurements of pristine and thinned flakes were compared, to examine if the thinning technique is thinning the entire desired area, and also because some methods reported in literature showed an increased surface roughness after laser-thinning/etching.[165]

AFM scans are shown in Figure 6.7, (along with optical microscope images) here for a flake thinned from a 3 to 2 layers (i.e. pristine at 3 layers) using a step size of 200 nm, a laser power density of 0.2 mW/μm^2 and a RH of 70%. It can be seen from Figure 6.7 that thinning has reduced surface roughness, in this case from ~ 0.8 to ~ 0.2 nm r.m.s. This improvement is thought to occur due to the top layer of the pristine $MoTe_2$ flake being contaminated by residues of PDMS and tape from the fabrication process, or from the removal of adsorbates as a result of thinning.

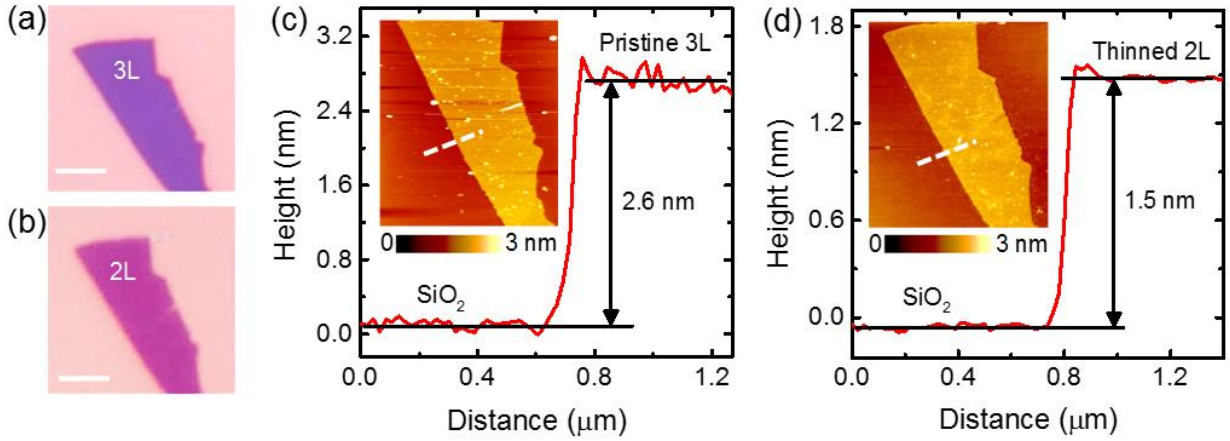

Figure 6.7: *Before and after a multi-layered flake is thinned down one layer. (a) & (b) Optical microscope images show the change in optical contrast after the thinning, which correlates to optical contrasts of 3-layer and 2-layer flakes respectively. (c) AFM of pristine flake with height profile taken from dashed white line in inset. (d) AFM of thinned flake with height profile taken at the same position as pristine flake. Noticeable change in the surface roughness is seen in the AFM height profile.*

6.3.2. Raman Spectroscopy

The Raman spectra peak positions and ratio of peak amplitudes were examined for pristine and thinned flakes having thicknesses from 9 layers right down to monolayer. In Figure 6.8(a) the Raman shifts of the $\mathbf{E^1_{2g}}$ and $\mathbf{A_{1g}}$ peaks are shown, with good agreement between the pristine and thinned flakes of all thicknesses. Changing of peak positions can indicate changes to the stress experience by atomically thin materials and changes in the band gap. The fact that the two sets of peaks show strong correlation indicates that the

thinned $MoTe_2$ should have similar properties and behave similarly in devices to pristine flakes of the same thickness.

Figure 6.8(b) shows the $\mathbf{B^1_{2g}/E^1_{2g}}$ and $\mathbf{E^1_{2g}}$/Si peak height ratios, which are commonly used to identify the thickness of $MoTe_2$ flakes. The $\mathbf{E^1_{2g}}$/Si ratio is best used for this purpose, and in Figure 6.8(b) both pristine and thinned Raman spectra show the same ratios, within uncertainty.

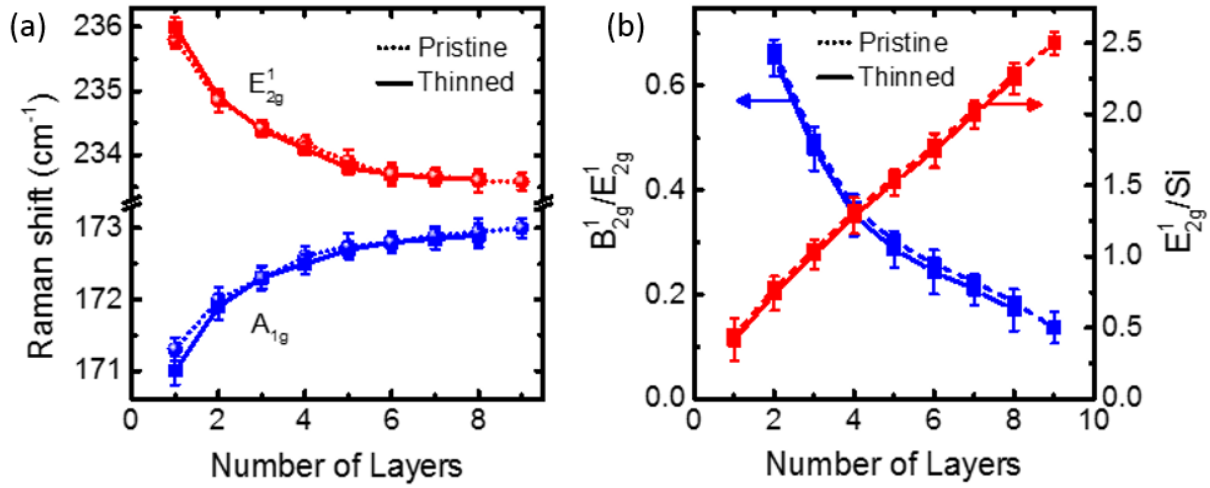

Figure 6.8: *(a) Raman spectra shift for the two main peaks for thinned and pristine $MoTe_2$ samples ranging in thickness from 9 to 1 layer (b) The Raman peak ratios $\boldsymbol{B^1_{2g}/E^1_{2g}}$ (left axis) and the $\boldsymbol{E^1_{2g}}$/Si (right axis) , used to identify flake thickness; both pristine and thinned $MoTe_2$ data is provided and is identical (within measurement uncertainty).*

6.3.3. Photoluminescence

The Photoluminescence (PL) signals of flakes of thicknesses ranging from 5 to 1 layer were recorded to determine if any difference could be observed between pristine and thinned samples. In Figure 6.9(a) the PL of a pristine monolayer $MoTe_2$ is shown, with a change in the peak position of 7 meV noted for when compared to a thinned monolayer. This shift is attributed to a change in doping level in the thinned samples from water adsorbates, during exposure to high humidity conditions during the thinning process. Shifts in PL peak position have been seen previously for MoS_2 when annealed in ambient conditions and were also attributed to doping.[177]

In Figure 6.9(b) the peak positions and the full width at half-maximum (FWHM) values of the PL response are shown for up to five layer thick $MoTe_2$ of pristine and thinned form. Again, a change in peak position of 7 meV is seen for monolayer thinned flakes (c.f. the pristine case), with all other thicknesses experiencing a smaller 3 meV shift, from the same reasons as already mentioned. The FWHM of the PL response shows strong agreement between pristine and thinned samples, with the peaks becoming narrower as the thickness reduces and the band gap becomes more direct.

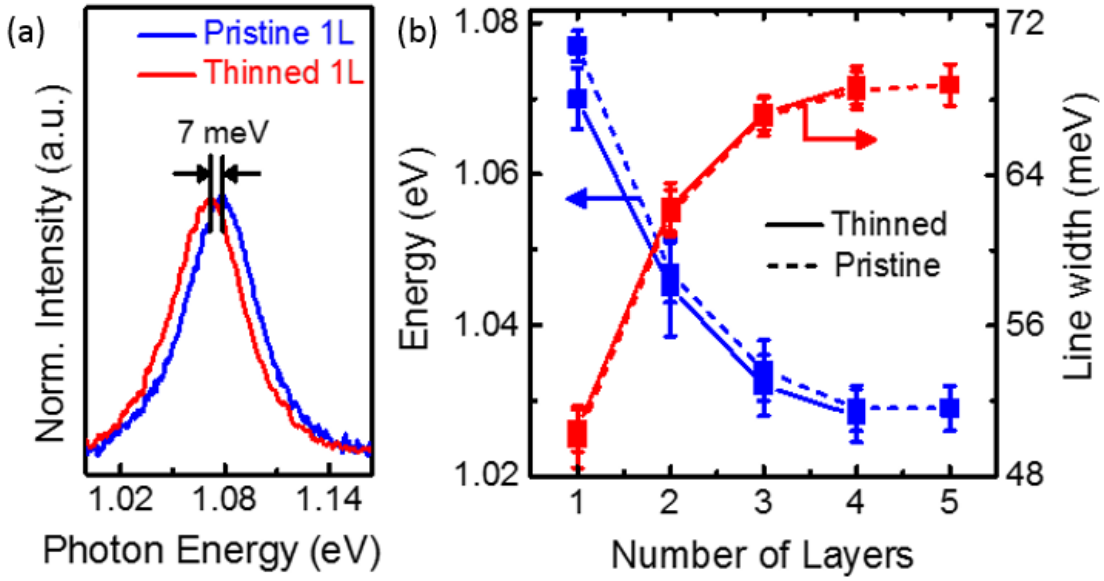

Figure 6.9: *(a) Comparison of the photoluminescence response of pristine and thinned monolayer $MoTe_2$. (b) Comparisons of PL spectral peak position and linewidth for pristine and thinned flakes with thicknesses from 1 to 5 layers.*

In summary, pristine and layer-by-layer thinned $MoTe_2$ samples showed no significant differences in Raman spectra, along with a slight improvement on cleanliness of the surface and shifts in the PL spectra to do, most likely, with the removal of adsorbates. Optical contrast measurements also showed no noticeable change between pristine and thinned flakes of the same thicknesses. Indeed, from the characterizations described above, the novel photochemical thinning method developed during the work of this thesis seems to only improve the quality of flakes.

6.4. Photothermally Thinned Monolayer $MoTe_2$ Devices

To show the photothermal thinning technique can be used to provide $MoTe_2$ semiconducting channels with user-defined thicknesses in actual devices, thinned flakes were used in FETs who's electrical and optoelectronic properties were then tested in ambient and vacuum conditions. Of particular interest is whether thinned channel devices present any improvements in photoresponsivity or photoresponse times as compared to devices fabricated with pristine (un-thinned) material. Note that in the device results presented here, the thinning is carried out *in-situ* (i.e. after the basic FET device has been fabricated) only the area of the channel itself is thinned, so the device electrical contact is between pristine (here four-layer) $MoTe_2$ and the Cr/Au electrodes. Having thicker flakes at the $MoTe_2$/metal contact interface shows significant impact on the electronic properties by lowering the Schottky barrier height,[108] especially important for monolayer $MoTe_2$ which typically shows poor performance in devices in literature[74] and our own work (see Section 2.4). An overall schematic for the process of thinning the $MoTe_2$ channel in FET devices is shown in Figure 6.10.

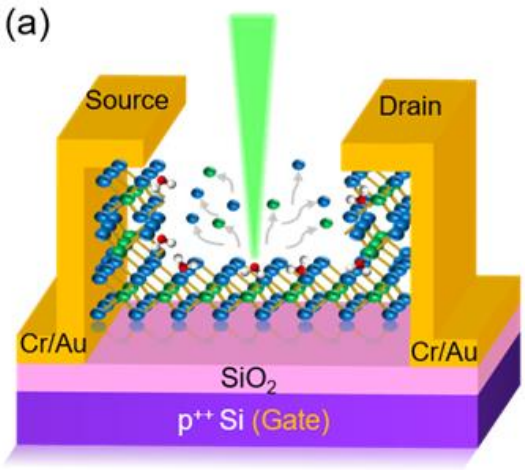

Figure 6.10: *Schematic of in-situ thinned-channel FET devices, with pristine $MoTe_2$/metal contacts.*

6.4.1. Electrical Measurements

FET devices fabricated in this thesis entirely with pristine, monolayer $MoTe_2$ showed relatively low mobility (see Section 2.4), in line with other studies on monolayer $MoTe_2$.[74] Initial devices using completely thinned monolayer $MoTe_2$, including thinning the flakes at the $MoTe_2$/metal contact interface (the latter being carried out *ex-situ*), also showed rather low mobility. To remedy this issue, in subsequent investigations only the channel area was thinned, with the resulting device performance much improved. Using thicker flakes is already known to reduce the contact resistance in MoS_2 devices,[108] and the same effect is expected for $MoTe_2$ devices, with a subsequent improvement in performance.

An example of a pristine $MoTe_2$ monolayer FET is shown for reference in Figure 6.11. A mobility of 0.19 mcm^2/Vs is found for the monolayer $MoTe_2$ FET, with more than 20 other monolayer devices showing no conductivity at all in ambient conditions. This shows the marked improvement of laser-thinning the channel for the conductivity of $MoTe_2$ FET devices.

In Figure 6.12, the output and transfer characteristics for a pristine, four-layer $MoTe_2$ FET device are shown, along with results for the same device with the channel thinned to a monolayer. The output characteristic shows a large difference in resistance from ~1 GΩ to ~50 MΩ. The pristine device shows a hole mobility of 0.2 cm^2/Vs, which increases to ~0.3 cm^2/Vs with the thinned channel device when V_{ds} = 10 V. Due to the increased conductivity of the monolayer device, the ON/OFF ratio increases from $2x10^4$ for the pristine device to 10^5 for the thinned channel, which compares very well to other $MoTe_2$ FET ON/OFF ratios measured in ambient conditions.[74,93]

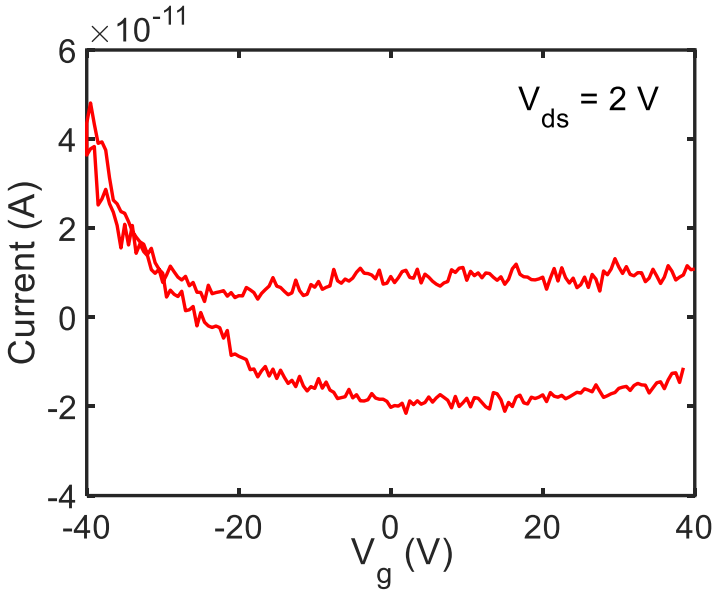

Figure 6.11: *Transfer characteristic of a pristine monolayer $MoTe_2$ flake, showing extremely poor conductivity in ambient conditions.*

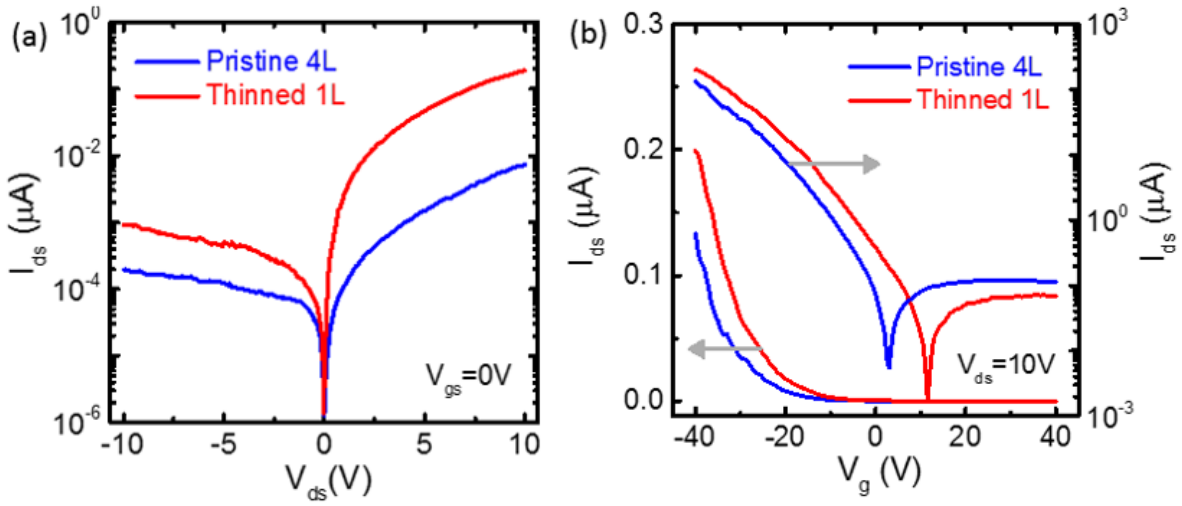

Figure 6.12: *(a) Output characteristic and (b) Transfer characteristic for a pristine, four-layer flake, which is then thinned to a monolayer channel and re-tested, showing enhanced conductivity.*

Figure 6.13 shows additional output characteristics for the thinned device, at V_g values between +60 and -60 V, along with transfer characteristics at V_{ds} values between 0.5 and 10 V. The output characteristics show a strongly rectifying behaviour for the thinned

device. From Figure 6.13(b), mobilities of ~1 cm^2/Vs at V_{ds} = 4 V are shown for the thinned, monolayer channel FET, similar to result shown in Chapter 3.

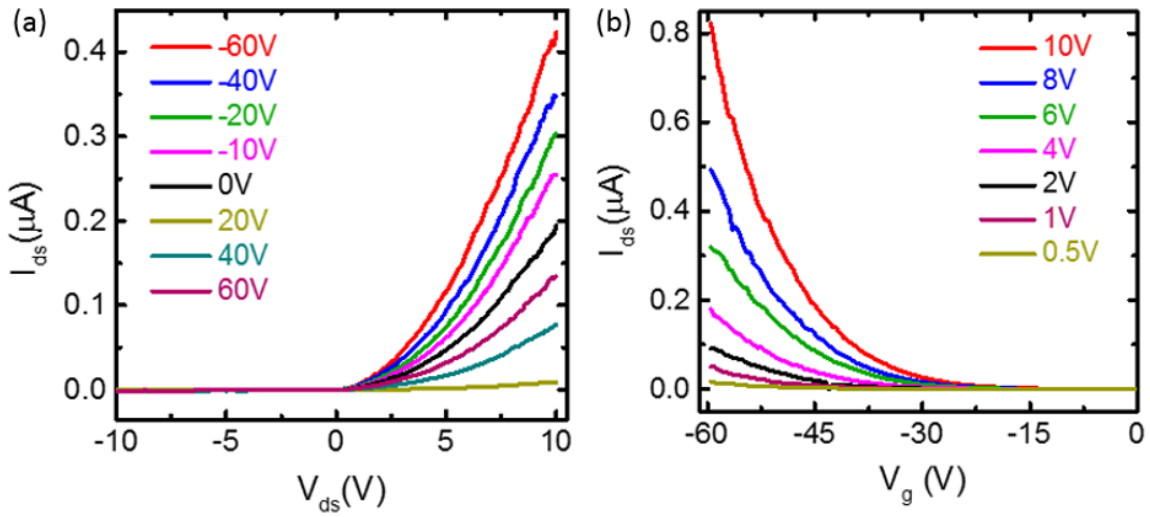

Figure 6.13: *(a) Output characteristics of the thinned monolayer channel FET with V_g varied between +60 V and -60 V. (b) Transfer Characteristics of the same FET, with V_{ds} values set between 0.5 V and 10 V.*

More typically, few-layer (bilayer and above) thicknesses are used in $MoTe_2$ FET devices, due to their increased mobilities at the few-layer thickness.[89] Previously monolayer $MoTe_2$ transfer characteristics have shown mobilities of 0.03 cm^2/Vs,[56] $3x10^{-4}$ cm^2/Vs,[74] along with rather low conductivity.[93] Devices with h-BN encapsulation show much better mobilities with reduced effects from trap states.[83] One study on monolayer $MoTe_2$ devices by Kim et al.[67] did show a high mobility and ON/OFF ratio[67] , but this could be a result of treating the substrates with an oxygen plasma that is known to have positive effects on the mobilities of TMDCs[50], but does unfortunately have a detrimental effect on the lifetime of $MoTe_2$.[159] Overall however it is likely that with high levels of defects and adsorbates, monolayer $MoTe_2$ is unable to form a low-resistance good electrical contact with evaporated metal contacts, making monolayer $MoTe_2$ devices challenging to use. By using thicker $MoTe_2$ at the $MoTe_2$/metal contact interface, it is possible to circumvent the issues with monolayer $MoTe_2$ FETs.

6.4.2. Optoelectronic Measurements

The transfer characteristic and transient photocurrent measurements for a thinned monolayer device were taken, showing the optoelectronic performance of the thinned monolayer $MoTe_2$ channel device. In Figure 6.14, by way of example, a transient measurement of a monolayer channel FET is shown, here resulting in a photocurrent of ~25 nA over a time period of 100s. No significant decay of the photocurrent is observed here (from photo-desorption methods discussed in Chapter 5) as the 685 nm laser is used for this measurement.

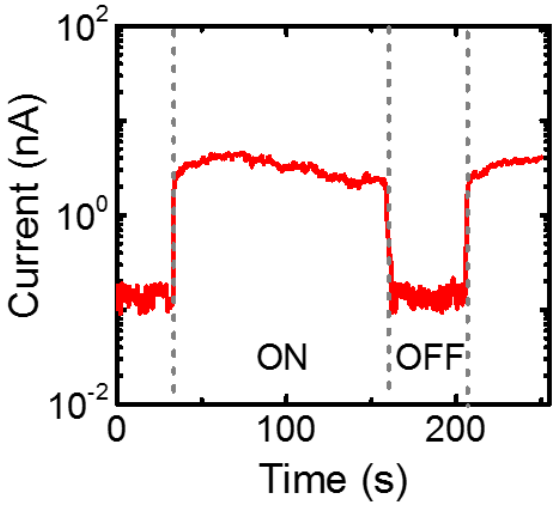

Figure 6.14: *Transient photocurrent measurement with 685 nm laser modulated on a slow timescale (V_{ds} = 10 V).*

In Figure 6.15 the transfer characteristic of the same FET is shown for illumination by a 3 µW 685 nm laser. In this figure, a photocurrent of 290 nA is generated in the ON state which relates to a photoresponsivity of 105 mA/W. The main mechanism for photocurrent generation during the transfer characteristic for pristine $MoTe_2$ is photogating, as described in chapter 3. However, photogating is not prominent for the monolayer device of Figure 6.15, with only a minor change occurring for the threshold voltage (V_T). This may be due to the smaller trap state population as some adsorbates were removed from the surface, shown by a reduction in the surface roughness. These results show that laser-thinned monolayer $MoTe_2$ semiconductor channels can in fact be used for optoelectronic applications, despite its low mobility in literature[74] and issues with oxidation in ambient conditions[159].

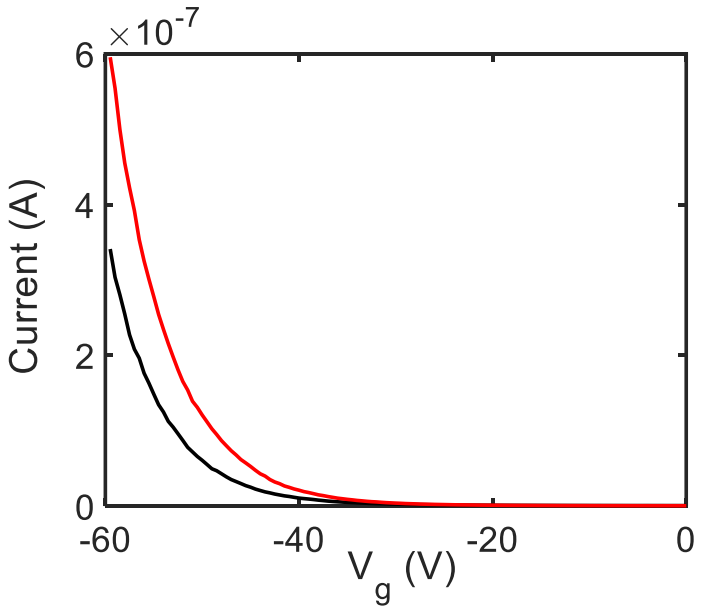

Figure 6.15: *Transfer characteristic of a monolayer thinned-channel $MoTe_2$ FET in the dark (black line) and with a 685 nm laser of 3 μW power (red line). Minimal photogating effects are seen from this device, due to the laser-thinning method cleaning the substrate and removing the source of trap states.*

6.5. Humidity-Assisted Layer-by-Layer Thinned Devices

A 14-layer flake was also thinned down to 9 layers with the humidity-assisted layer-by-layer thinning method on the semiconducting channel area only, to see the effect on the layer-by-layer thinning method for electrical and optoelectrical performance. Measurements on this device were taken at 10^{-5} Torr, to remove traces of adsorbates and water molecules from the surface to showcase the best properties for thinned and pristine $MoTe_2$

6.5.1. Electrical Results

The output characteristic of the pristine fourteen-layer device and a nine-layer thinned channel device are shown in Figure 6.16. The resistance, at ~1MΩ, is much lower for both the pristine fourteen-layer and thinned channel nine-layer devices than the results for the monolayer thinned results; this is because of the increased thickness at the

$MoTe_2$/metal contact interface. There is only a minor change shown in the output characteristic between the two measurements. As these measurements are taken at high vacuum, large improvement in mobilities and device resistance are observed, as also seen in the literature.[67]

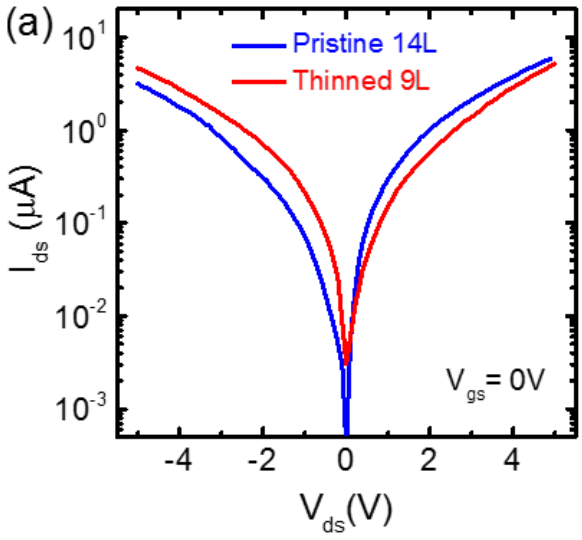

Figure 6.16: *Output characteristic of pristine14-layer device against the layer-by-layer thinned 9-layer device. Both devices show high conductivity (which was measured at 10^{-5} Torr).*

The transfer characteristics for both devices are shown in Figure 6.17, for values of V_{ds} ranging from 0.1 to 1 V. These results reveal a mobility increase from 12.4 to 13.5 cm^2/Vs after thinning. Based on the results of Figure 6.16 and Figure 6.17, it appears that the layer-by-layer thinning mechanism appears to cause no significant changes for $MoTe_2$ FETs; indeed, it possibly improves their properties by cleaning the surface of the material.

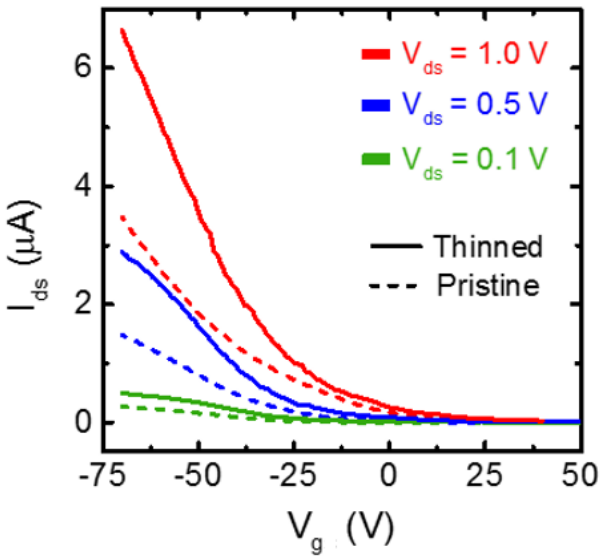

Figure 6.17: *Transfer characteristic for the thinned and pristine $MoTe_2$ devices as described above. Different values of V_{ds} were used to highlight the difference in mobility between the thinned and pristine flake.*

6.5.2. Optoelectronic Results

To show the potential of the photochemically layer-by-layer thinned $MoTe_2$, optoelectronic measurements, similar to those reported in Chapter 3 and Chapter 5, were carried out, here in vacuum conditions and using 473, 514 and 685 nm wavelength lasers.

6.5.2.1. Photocurrent Transients

The results of typical photocurrent transient measurements are shown for the layer-by-layer thinned nine-layer channel device in Figure 6.18. Here the laser was modulated manually and 514 nm and 685 nm wavelengths used. Both lasers had a power set to 6 μW and V_{ds} was set to 0.5 V. A photocurrent of ~35 nA is seen with the 514 nm laser and ~50 nA with the 685 nm. The results show strong stability for the photocurrent over a long time period of more than 300 seconds over multiple modulation cycles.

Despite using the 514 nm laser in the results of Figure 6.18, there is no decrease in the photocurrent with time as was seen for analogous results for non-thinned devices shown in Chapter 5, in Figures Figure 5.2Figure 5.3Figure 5.4. This is most likely a result of the removal of adsorbates from the channel in the high vacuum conditions, so photo-

desorption is not possible (changing the doping of $MoTe_2$ by removing adsorbates with electrical annealing has been observed by Chang et al.[65]). Photocurrent generation occurs here through the standard photovoltaic processes observed in Chapter 3, with the band-bending assisted photocurrent generation from the change in Fermi energy for $MoTe_2$.

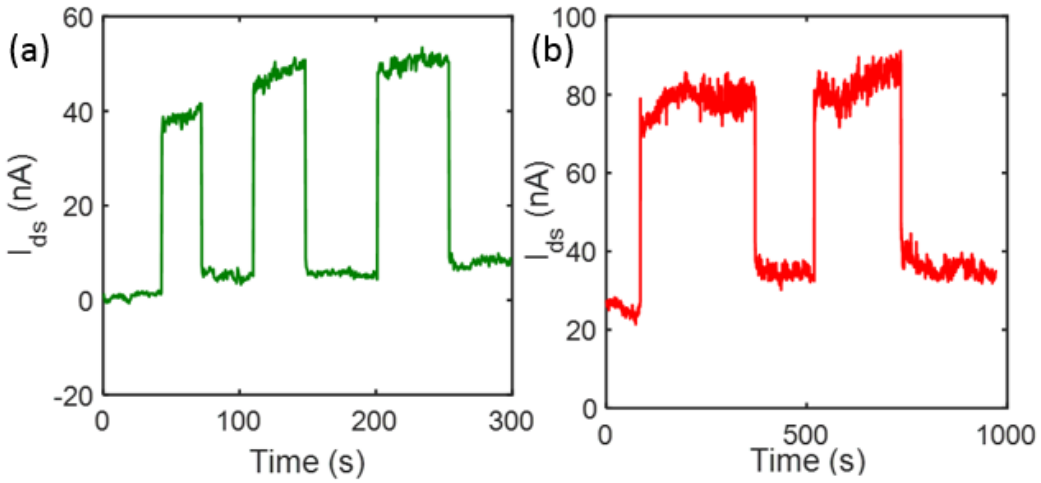

Figure 6.18: *Transient photocurrent measurements of the layer-by-layer thinned nine-layer channel device with V_{ds} = 0.5 V and V_g = 0 V for (a) 514 nm and (b) 685 nm lasers, with a power of 6 μW. Measurements do not show photo-desorption (most likely since measurements were carried out in vacuum).*

Further transient photocurrent measurements for these devices were carried out at high values of gate voltage (V_g = -70 V) with the device in the ON state, with results being shown in Figure 6.19. Photocurrent for both measurements is ~150 nA. A slow decrease in current with time can be seen during these transient measurements over the ~600 second time window investigated, similar to the results in Chapter 4 (Figure 4.3), where the device suffers from transient decay from the emission of holes from trap states. A larger increase in the current is observed in the ON state when compared to the result of Figure 6.18, which is attributed to either the photogating effect or the increase in conductivity of the channel.

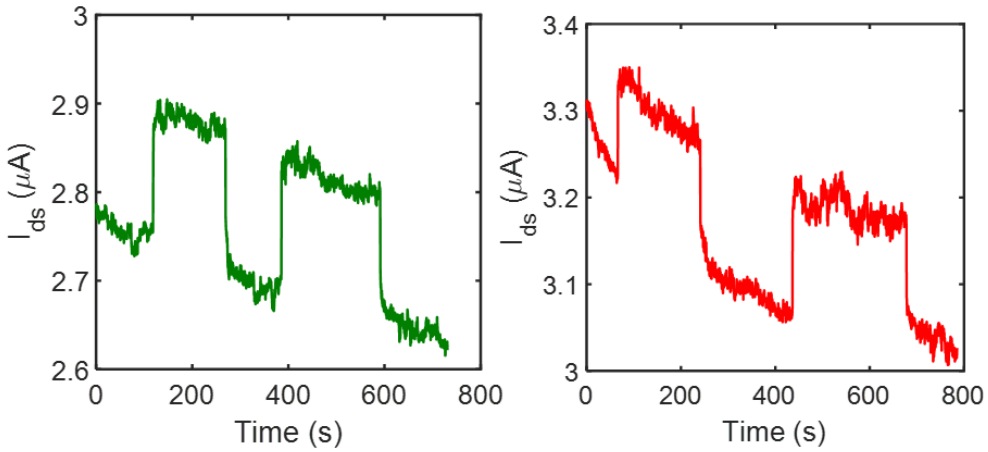

Figure 6.19: *Transient photocurrent measurements for the layer-by layer thinned nine-layer channel device in the ON state, with V_{ds} = 0.5 V and V_g = =70 V for 514 (left) and 685 nm (right) with a power of 6 µW.*

6.5.2.2. Output Characteristic

Output characteristics with the 685 nm laser with powers between 0.8 and 4.8 µW are displayed for the layer-by-layer (9-layer) thinned device in Figure 6.20. A photocurrent is observed with a photoresponsivity of ~0.2 A/W for this range of powers. The photoresponsivity is only slightly less than the photoresponsivity seen during transfer characteristics on $MoTe_2$ in this thesis of 6 A/W in Chapter 3 (Figure 3.3), showing that the vacuum conditions for $MoTe_2$ may improve optoelectronic performance due to the removal of adsorbates in the channel region.

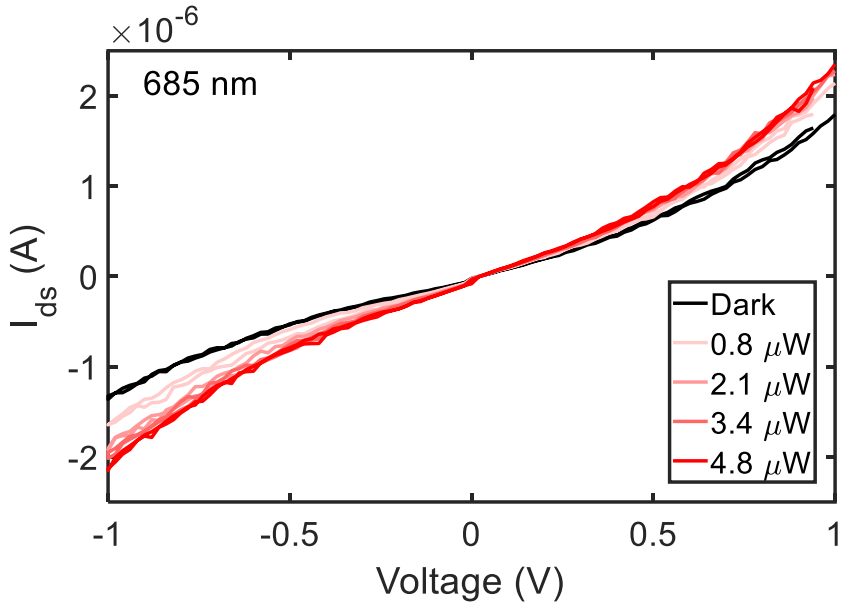

Figure 6.20: *Output characteristics (V_{ds} sweep) for the nine-layer layer-by-layer thinned device in dark (black line) and under 685 nm illumination (coloured lines). Measured in vacuum conditions.*

6.5.2.3. Transfer Characteristics

In Figure 6.21, the transfer characteristic for the 9-layer device in the dark and under 685 nm light is shown. A photoresponsivity of 235 mA/W is recorded in the ON state for this device, a similar result to other photoresponsivities reported for $MoTe_2$ based photodetectors.[101,136,178] The smaller photoresponsivity, compared to result in Chapter 3 of 6 A/W, may come from a lessened photogating effect, as there are no longer any adsorbates on the surface of the material. Additionally, a relatively high power of 6 μW was used for this measurement; using lower laser powers would lead to an increase in photoresponsivity – e.g. a 400 nW power was used for the measurement that producing 6 A/W in Chapter 3.

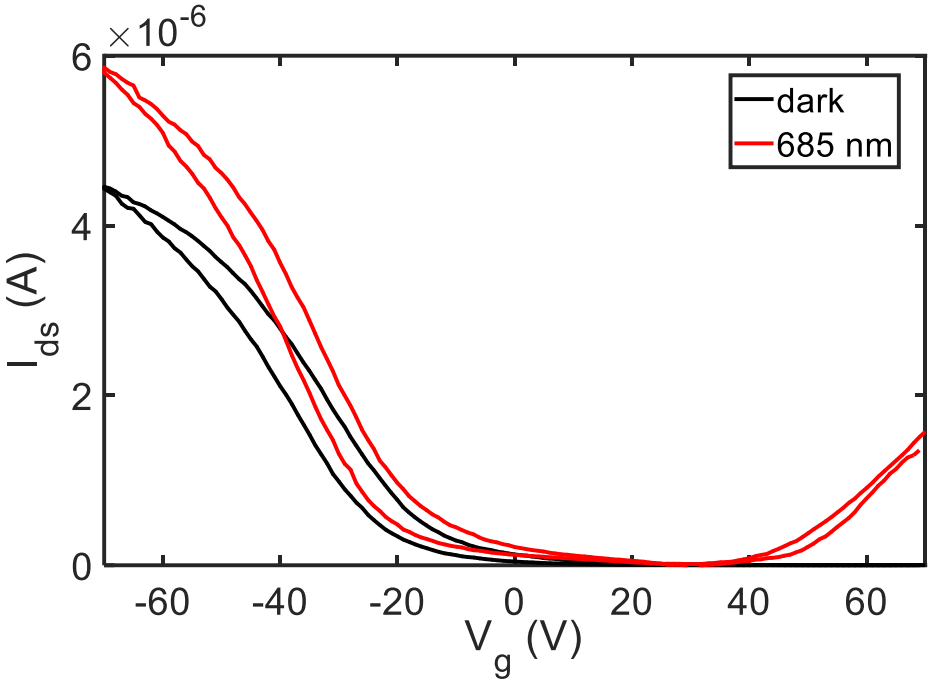

Figure 6.21: *Transfer characteristic of the 9-layer layer-by-layer thinned device first in dark (black lines), and with the 685 nm laser (red lines) at 6 μW power. A large increase in both n-type and p-type doping is observed in this measurement.*

Notable in Figure 6.21 are features seen at large positive gate voltages, where a mobility of 5.88 cm^2/Vs is created for n-type polarity under 685 nm light. This FET goes from strongly p-doped to ambipolar behaviour under illumination. The resulting shift in V_T is displayed in Figure 6.22, which shows the same result as for Figure 6.21 but on a logarithmic current scale. The charge neutrality point is shown to change from +55 V to +30 V when illuminated with the 685 nm laser. This shift in the charge neutrality point changes the V_T, allowing for n-type conduction to be observed as the device enters the ON state for n-type conduction at lower V_g values than before. As this measurement was completed in vacuum (10^{-5} Torr), a greater susceptibility for n-type conduction is possible with the removal of OH^- and O_2^- adsorbates which typically cause p-type doping.[149]

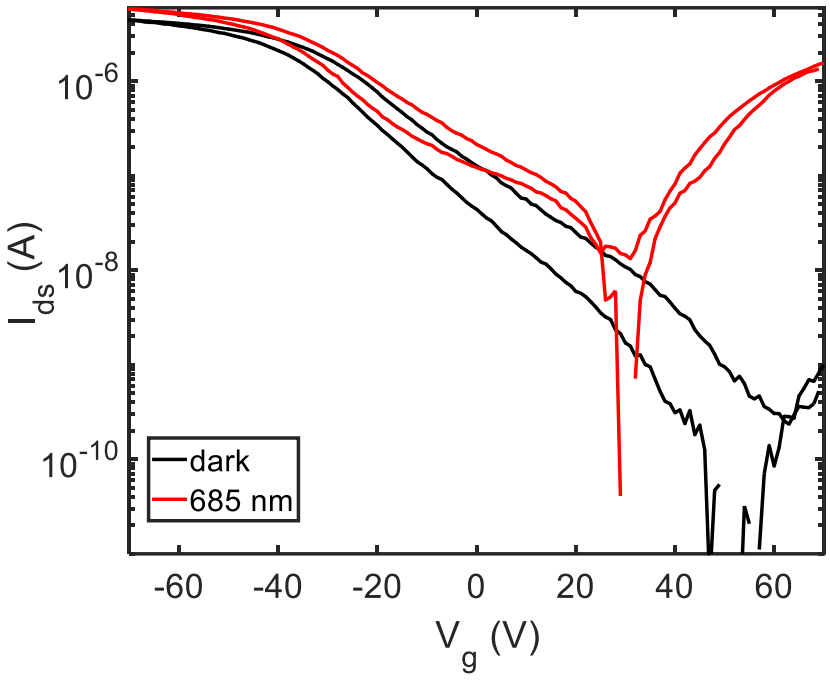

Figure 6.22: *Log scale plot of Figure 6.22, showing more clearly n-type doping under illumination. The charge neutrality point clearly changes, which allows the n-type conductivity to occur at lower V_g values.*

In Figure 6.23 the transfer characteristics with 473, 514 and 685 nm illumination are shown. A clear trend between wavelength of illumination and the photocurrent in for p and n-type doping is observed, with the 685 nm causing the greater increase in mobility in both cases. Higher energy photons from the 514 and 473 nm light may be causing radiative recombination due to energy of these photons (~2.4-2.6 eV) being much greater than the band gap (1.1 eV). By putting a $MoTe_2$ device in the ON state for n-type conduction, laser light could be used to create a 4 orders of magnitude difference in response in photocurrent, between 685 and 473 nm. These FETs could potentially be used for wavelength dependent signalling applications, due to the vastly different response between just small ranges of wavelengths for n-type conduction.

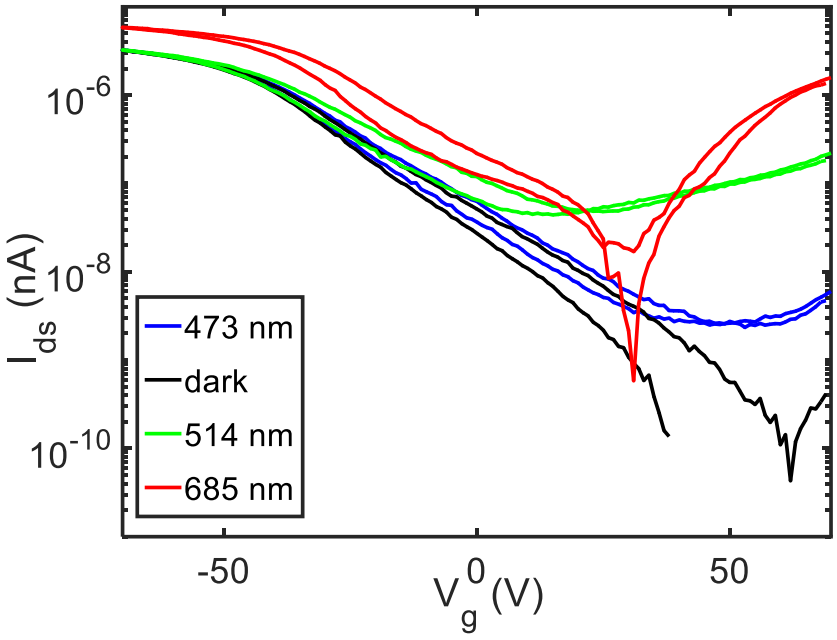

Figure 6.23: *Transfer characteristics in dark (black line) and 3 separate wavelengths (coloured lines), showing a 4 order of magnitude difference in the n-type conductivity.*

6.5.2.4. Photocurrent Mapping

Since the above measurements were carried out in vacuum conditions and not ambient, it is important to check that the photocurrent still originates from the $MoTe_2$/metal contact interface, as was observed previously for devices fabricated with pristine flakes (see Chapter 3, Figure 3.8). A photocurrent map at two different gate voltages is thus used to identify the photocurrent mechanisms in vacuum for the thinned flake. Maps at V_g = 0 V and V_g = -30 V are shown in Figure 6.24, which identify that the source electrode is the again the area where the largest photocurrent is generated, even with an applied gate voltage. No significant change in the position of largest generated photocurrent was observed with the device in the ON state and with no applied gate voltage. The result in Figure 6.24 concurs with those on pristine flakes, showing the photocurrent mechanism is unchanged from the pristine flake devices shown in chapter 3. This result continues to be in agreement with work reported by Howell et al.,[128] where an increase in number of excited carriers shifts the Fermi energy, in turn reducing the Schottky barrier height, making the $MoTe_2$/metal contact interface the most important area for photocurrent generation.

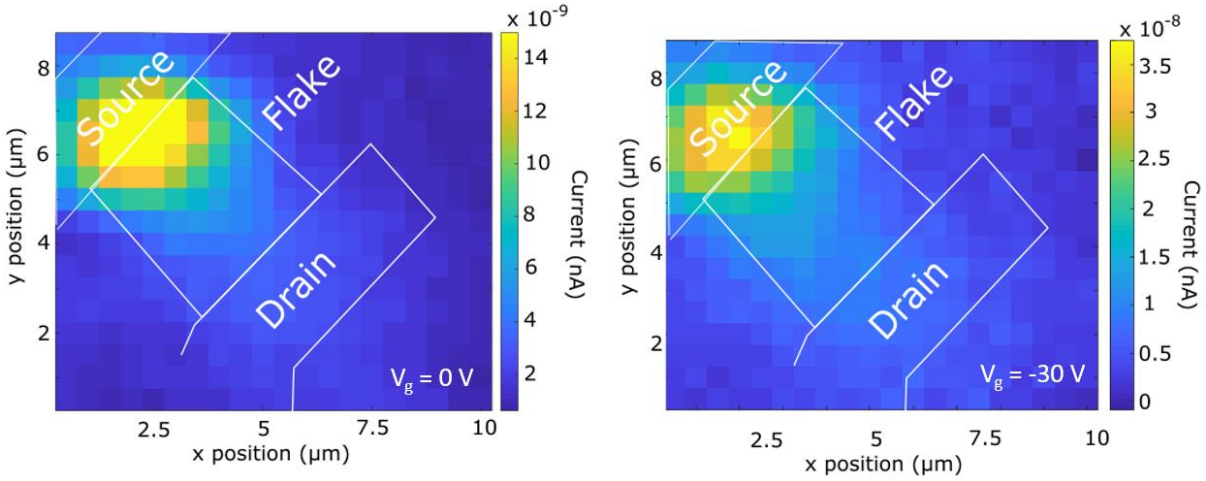

Figure 6.24: *Photocurrent maps of the 9-layer layer-by-layer thinned device at V_g = 0 and -30 V respectively at V_{ds} = 0.5 V and with 6 μW, 685 nm laser.*

6.5.2.5. Response Time Measurement

The photocurrent response using a signal generator and lock-in amplifier, recorded under 685 nm laser illumination is shown in Figure 6.25. Response times of 45 and 35 μs for the rise and fall times of the device respectively are found when modulating the laser at 2018 Hz. These times are taken from the 90%/10% modulation of the photocurrent signal. This response time is one order of magnitude faster than the (pristine) four-layer device reported on in the previous Chapter 3. By using an exponential fit, a similar response time of 25 and 20 μs are found for the rise and fall times respectively. The improvements to the response time may be due to the laser-thinning process cleaning the $MoTe_2$ flake through laser assisted ablation of the top layers of $MoTe_2$, removing trace layers of PMMA residues and surface adsorbates. This measurement was also completed in vacuum instead of ambient conditions, which reduces surface adsorbates, improving the purity of the $MoTe_2$ sample, as shown previously .[65] Crystal quality has also been shown to improve the photocurrent response times in SnS_2.[132]. Note also that the rise/fall time estimates are here still limited by the use of the limited bandwidth/speed of current pre-amplifier, with a response time of >10 μs.

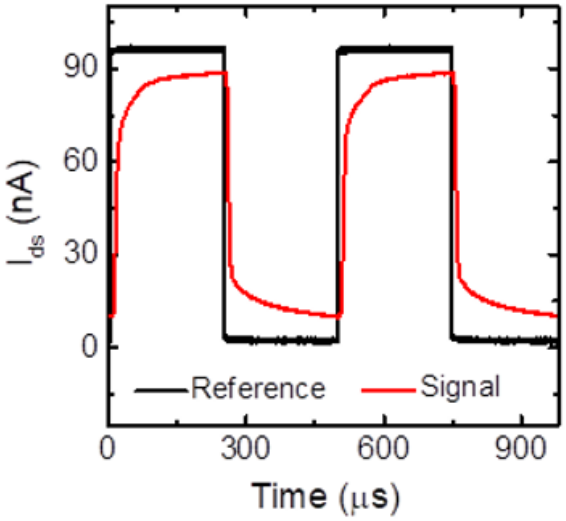

Figure 6.25: *Response time measurement for (9-layer) layer-by-layer thinned $MoTe_2$ device, here measured with a 685 nm laser illumination modulated at 2018 Hz.*

6.6. Conclusion

In this chapter a novel low-power, photochemical method for user-defined layer-by-layer thinning of $MoTe_2$ was developed and presented. The method was shown to be strongly dependent and reliant on humidity. FETs fabricated using $MoTe_2$ flakes thinned in this way showed excellent electrical, and optoelectronic properties, with high mobilities and photoresponsivities for photothermally thinned monolayer $MoTe_2$ channels, and layer-by-layer thinned channels. Layer-by-layer thinned channels have the same mechanisms of photogain as pristine flakes, as well as similar response times than their pristine counterparts.

Further work might concentrate on modifying the layer-by-layer thinning method use under lasers with larger spot sizes, for use on larger areas of $MoTe_2$ such as those grown by CVD or PVD methods. So far, this work on $MoTe_2$ paves the way for a scalable method for the fabrication of homogenous, clean flakes for fabrication into larger more complex device geometries.

7. Final Remarks

7.1. Conclusions

$MoTe_2$ is becoming a material of great interest because of its NIR band gap, potential for phase change and potential as a Weyl semi-metal. In this thesis, the TMDC material $MoTe_2$ has been examined in detail, specifically using electronic and optoelectronic measurements completed at different operating conditions. Trap states present from adsorbates on the surface of $MoTe_2$ are responsible for many of the fascinating properties of $MoTe_2$ FETs, with results in this work noting their importance for large photogain effects, and understanding their effects in electronic measurements. Efforts on the interaction with adsorbates under illumination show promise, with the ability to both remove these adsorbates for gas sensing applications, and even thin $MoTe_2$ through a humidity assisted mechanism to any layer thickness. Work in this thesis indicates that $MoTe_2$ may be used in flexible, transparent optoelectronics devices in exciting areas such as wearable technology.

In Chapter 3, the optoelectronic properties of four-layer flakes of $MoTe_2$ materials, were examined in FET configuration, providing fast, high photoresponsivity photodetection in the visible part of the spectrum. Photocurrent generation was shown via two main mechanisms facilitated by the photovoltaic effect. The first of these mechanisms is responsible for high photocurrent gain by the photogating mechanism, prevalent in low-dimensional materials, leading to a high photoresponsivity of 6 A/W when the FET is in the ON state. Fast photocurrent response times of 20 μs were made possible by the second mechanism, Schottky barrier lowering through band-bending at the $MoTe_2$/metal contact interface, which dominates photocurrent generation without an applied gate. Preliminary measurements attempting to decrease the response time through encapsulation with h-BN showed no significant effect, with future work recommended to examine the role of encapsulation for optoelectronic properties.

Electronic transient properties of $MoTe_2$ were examined in Chapter 4, to better understand how adsorbates affect the workings of $MoTe_2$ in FETs in ambient conditions, through mid-gap trap states. This work fits trap states into two different levels, shallow and deeper traps, while a theoretical study shows how the trap states rely on the applied

bias, not just for $MoTe_2$ but all TMDCs, with shallow traps having no dependence and deeper traps showing linear dependence to applied bias. This study was experimentally verified by changing $\mathbf{V_{ds}}$ values in transient current measurements. Since trap states are particularly important in $MoTe_2$, due to Te deficiencies leading to a higher proportion of dangling bonds, understanding how these trapped charges are emitted and captured provides important knowledge for how to best use TMDCs in defect-based applications such as photodetectors and memory devices.

Higher energy visible light was used to further examine the optoelectronic properties of $MoTe_2$ using the same FET configuration. Interestingly, negative photocurrent effects were observed during transient measurements and transfer characteristics. This work, performed in Chapter 5, shows that it is possible to use light to promote the photo-desorption of adsorbates from the $MoTe_2$ surface, owing to its high surface area and Te vacancies which strongly attract O_2 to form relatively strong Te-O bonds. Negative photoconductivity in transient photocurrent measurements showed energy dependence, with the highest used energies performing the fastest photo-desorption. The dependence of layer thickness for this mechanism was also observed, with the thinnest sample used, a bi-layer, showing the fastest generated negative photocurrents. Using photo-desorption for adsorbates can radically change the electrical properties of $MoTe_2$, with applications in creating a defect free surface of $MoTe_2$ for sensing a possibility for the future.

While previous chapters already showed the strong effects between $MoTe_2$ and incident light, in Chapter 6 a humidity assisted, layer-by-layer, targeted photochemical etching method was devised, also through light interaction. The thinning mechanism is enabled by the presence of high humidity and is achieved at much lower power than any thinning mechanism shown before for TMDCs. FETs fabricated using the layer-by-layer thinned flakes, showed superb electrical and optoelectronic properties, with high mobilities and photoresponsivities obtained for monolayer thinned channels, and layer-by-layer thinned channels. FETs with only the channel thinned to monolayer, while retaining thicker $MoTe_2$ below the metal contacts, showed considerable improvements as compared to monolayer-only devices (monolayer $MoTe_2$ is well-known for its poor electrical properties). By generating any thickness of flake easily through this method,

and with its exciting optoelectronic properties, $MoTe_2$ shows promise as a material with prospective use in industry as a flexible, atomically thin, transparent photodetector.

7.2. Future Work

Work in Chapter 5 revealed the possibility of removing adsorbates in $MoTe_2$ using high energy, visible wavelength photons. By cleaning the surface of $MoTe_2$, it may be possible to use $MoTe_2$ in different environments, for example in the presence of low concentrations of harmful gases to observe the chemical sensing capabilities of $MoTe_2$. Electrical measurements in a humidity controlled system should be completed to show the possibility of using $MoTe_2$ as a humidity sensor, as we have shown already in Chapter 5 that $MoTe_2$ can even be controllably thinned in high humidity environments. It may also be of interest to use the adsorbate removing technique to examine the charge trapping dynamics without adsorbates, to see if the mid-gap trap state populations can be interacted with using high energy visible wavelength photons.

It may be of interest to see if the humidity thinning technique is truly unique to $MoTe_2$. This could be accomplished by better understanding the humidity assisted thinning mechanism in the material by modelling methods such as density functional theory to propose a chemical reaction responsible for the low power thinning technique. Using the thinning technique it is possible to create nano-patterns at 200 nm scale feature sizes, using these nanoscale features it may be possible to enhance the interaction of $MoTe_2$ with light by utilising different thicknesses of $MoTe_2$ in the same device.

Further work on understanding why monolayer $MoTe_2$ is unsuitable for the formation of interfaces with metal contacts in electrical transport should also be undertaken, perhaps by measuring $MoTe_2$ FETs at different layer thicknesses at low temperatures. Low temperature measurements make it possible to extract the Schottky barrier height of semiconductors, investigations on the barrier height may elucidate problems with monolayer $MoTe_2$ in FETs.

8. References

1. Akinwande, D., Petrone, N. & Hone, J. Two-dimensional flexible nanoelectronics. *Nat. Commun.* **5,** 1–12 (2014).

2. Das, S., Gulotty, R., Sumant, A. V. & Roelofs, A. All two-dimensional, flexible, transparent, and thinnest thin film transistor. *Nano Lett.* **14,** 2861–2866 (2014).

3. Lee, G.-H. *et al.* Flexible and Transparent MoS 2 Field-Effect Transistors on Hexagonal Boron Nitride-Graphene Heterostructures. *ACS Nano* **7,** 7931–7936 (2013).

4. Wang, Q. H., Kalantar-Zadeh, K., Kis, A., Coleman, J. N. & Strano, M. S. Electronics and optoelectronics of two-dimensional transition metal dichalcogenides. *Nat. Nanotechnol.* **7,** 699–712 (2012).

5. Mak, K. F. & Shan, J. Photonics and optoelectronics of 2D semiconductor transition metal dichalcogenides. *Nature Photonics* **10,** 216–226 (2016).

6. Wang, F. *et al.* Synthesis, properties and applications of 2D non-graphene materials. *Nanotechnology* **26,** 1–26 (2015).

7. Koppens, F. H. L. *et al.* Photodetectors based on graphene, other two-dimensional materials and hybrid systems. *Nat. Nanotechnol.* **9,** 780–793 (2014).

8. Novoselov, K.S., Geim, A.K., Morozov, S.V., Jiang, D.A., Zhang, Y., Dubonos, S.V., Grigorieva, I.V. and Firsov, A. A. Electric field effect in atomically thin carbon films. *Science (80-.).* **306,** 666–669 (2004).

9. Lee, C., Wei, X., Kysar, J. W. & Hone, J. Measurement of the elastic properties and intrinsic strength of monolayer graphene. *Science (80-.).* **321,** 385–8 (2008).

10. Nair, R. R. *et al.* Fine structure constant defines visual transparency of graphene. *Science (80-.).* **320,** 1308 (2008).

11. Han, T. *et al.* Extremely efficient flexible organic light-emitting diodes with modified graphene anode. *Nat. Photonics* **6,** 105–110 (2012).

12. Liu, Z., Robinson, J. T., Sun, X. & Dai, H. PEGylated Nano-Graphene Oxide for Delivery

of Water Insoluble Cancer Drugs. *J. Am. Chem. Soc.* **130,** 10876–10877 (2008).

13. Pumera, M. Graphene-based nanomaterials for energy storage. *Energy Environ. Sci.* **4,** 668–674 (2011).

14. Withers, F., Bointon, T. H., Craciun, M. F. & Russo, S. All-graphene photodetectors. *ACS Nano* **7,** 5052–7 (2013).

15. Xia, F., Wang, H., Xiao, D., Dubey, M. & Ramasubramaniam, A. Two-dimensional material nanophotonics. *Nat. Photonics* **8,** 899–907 (2014).

16. Lee, J., Shin, J., Lee, G.-H. & Lee, C. Two-Dimensional Semiconductor Optoelectronics Based on van der Waals Heterostructures. *Nanomaterials* **6,** 1–18 (2016).

17. Chhowalla, M. *et al.* The chemistry of two-dimensional layered transition metal dichalcogenide nanosheets. *Nat. Chem.* **5,** 263–75 (2013).

18. Tong, X., Ashalley, E., Lin, F., Li, H. & Wang, Z. M. Advances in MoS2-Based Field Effect Transistors (FETs). *Nano-Micro Lett.* **7,** 203–218 (2015).

19. Radisavljevic, B., Radenovic, A., Brivio, J., Giacometti, V. & Kis, A. Single-layer MoS2 transistors. *Nat. Nanotechnol.* **6,** 147–50 (2011).

20. Kim, Y., Huang, J. L. & Lieber, C. M. Characterization of nanometer scale wear and oxidation of transition metal dichalcogenide lubricants by atomic force microscopy. *Appl. Phys. Lett.* **59,** 3404–3406 (1991).

21. Song, S. *et al.* Room Temperature Semiconductor-Metal Transition of MoTe2 Thin Films Engineered by Strain. *Nano Lett.* **16,** 188–193 (2016).

22. Keum, D. H. *et al.* Bandgap opening in few-layered monoclinic MoTe2. *Nat. Phys.* **11,** 482–487 (2015).

23. Fan, X. *et al.* Fast and Efficient Preparation of Exfoliated 2H MoS2 Nanosheets by Sonication-Assisted Lithium Intercalation and Infrared Laser-Induced 1T to 2H Phase Reversion. *Nano Lett.* **15,** 5956–5960 (2015).

24. Mak, K. F., Lee, C., Hone, J., Shan, J. & Heinz, T. F. Atomically Thin MoS2: A New Direct-Gap Semiconductor. *Phys. Rev. Lett.* **105,** 136805 (2010).

25. Liu, H. L. *et al.* Optical properties of monolayer transition metal dichalcogenides probed by spectroscopic ellipsometry. *Appl. Phys. Lett.* **105,** (2014).

26. Yoffe, A. D. Low-dimensional systems: quantum size effects and electronic properties of semiconductor microcrystallites (zero-dimensional systems) and some quasi-two-dimensional systems. *Adv. Phys.* **51,** 799–890 (2002).

27. Cho, S. *et al.* Phase patterning for ohmic homojunction contact in MoTe2. *Science (80-.).* **349,** 625–628 (2015).

28. Wang, Z. *et al.* MoTe2: A Type-II Weyl Topological Metal. *Phys. Rev. Lett.* **117,** 056805 (2016).

29. Liu, Z. K. *et al.* A stable three-dimensional topological Dirac semimetal Cd3As2. *Nat. Mater.* **13,** 677–681 (2014).

30. Gusmão, R., Sofer, Z. & Pumera, M. Black Phosphorus Rediscovered: From Bulk Material to Monolayers. *Angewandte Chemie - International Edition* **56,** 8052–8072 (2017).

31. Avsar, A. *et al.* Air-stable transport in graphene-contacted, fully encapsulated ultrathin black phosphorus-based field-effect transistors. *ACS Nano* **9,** 4138–4145 (2015).

32. Zhang, K., Feng, Y., Wang, F., Yang, Z. & Wang, J. Two dimensional hexagonal boron nitride (2D-hBN): Synthesis, properties and applications. *Journal of Materials Chemistry C* **5,** 11992–12022 (2017).

33. Wang, J. I. J. *et al.* Electronic transport of encapsulated graphene and WSe2 devices fabricated by pick-up of prepatterned hBN. *Nano Lett.* **15,** 1898–1903 (2015).

34. Withers, F., Bointon, T. H., Hudson, D. C., Craciun, M. F. & Russo, S. Electron transport of WS2 transistors in a hexagonal boron nitride dielectric environment. *Sci. Rep.* **4,** 1–5 (2014).

35. Shi, Y., Li, H. & Li, L. J. Recent advances in controlled synthesis of two-dimensional transition metal dichalcogenides via vapour deposition techniques. *Chemical Society Reviews* **44,** 2744–2756 (2015).

36. Zaidy, G. Al *et al.* Phase Engineering of Tin Sulphide Grown by Atmospheric Pressure Chemical Vapour Deposition at Ambient Temperature. *2017 Conf. Lasers Electro-Optics Eur. Eur. Quantum Electron. Conf.* (2017).

37. Orsi Gordo, V. *et al.* Revealing the nature of lowerature photoluminescence peaks by laser treatment in van der Waals epitaxially grown WS2monolayers. *Nanoscale* **10,** 4807–4815 (2018).

38. McDonnell, L. P., Huang, C. C., Cui, Q., Hewak, D. W. & Smith, D. C. Probing Excitons, Trions, and Dark Excitons in Monolayer WS2Using Resonance Raman Spectroscopy. *Nano Lett.* **18,** 1428–1434 (2018).

39. Xia, J. *et al.* CVD synthesis of large-area, highly crystalline MoSe2 atomic layers on diverse substrates and application to photodetectors. *Nanoscale* **6,** 8949–55 (2014).

40. Reina, A. *et al.* Large area, few-layer graphene films on arbitrary substrates by chemical vapor deposition. *Nano Lett.* **9,** 30–5 (2009).

41. Huang, J. H. *et al.* Large-Area 2D Layered MoTe2 by Physical Vapor Deposition and Solid-Phase Crystallization in a Tellurium-Free Atmosphere. *Adv. Mater. Interfaces* **4,** 2–9 (2017).

42. Vishwanath, S. *et al.* MBE growth of few-layer 2H-MoTe2 on 3D substrates. *J. Cryst. Growth* **482,** 61–69 (2018).

43. Yu, Y. *et al.* Molecular beam epitaxy growth of atomically ultrathin MoTe2lateral heterophase homojunctions on graphene substrates. *Carbon N. Y.* **115,** 526–531 (2017).

44. Wang, S., Wang, X. & Warner, J. H. All Chemical Vapor Deposition Growth of MoS 2 :h-BN Vertical van der Waals Heterostructures. *ACS Nano* **9,** 5246–5254 (2015).

45. Zhang, G., Liu, H., Qu, J. & Li, J. Two-dimensional layered MoS 2 : rational design, properties and electrochemical applications. *Energy Environ. Sci.* **9,** 1190–1209 (2016).

46. Ganatra, R. & Zhang, Q. Few-layer MoS2: A promising layered semiconductor. *ACS*

Nano **8,** 4074–4099 (2014).

47. Octon, T. J., Nagareddy, V. K., Russo, S., Craciun, M. F. & Wright, C. D. Fast High-Responsivity Few-Layer MoTe2 Photodetectors. *Adv. Opt. Mater.* **4,** 1750–1754 (2016).

48. Feng, Z. *et al.* Enhanced Sensitivity of MoTe2 Chemical Sensor through Light Illumination. *Micromachines* **8,** 1–8 (2017).

49. Duerloo, K.-A. N., Li, Y. & Reed, E. J. Structural phase transitions in two-dimensional Mo- and W-dichalcogenide monolayers. *Nat. Commun.* **5,** 1–9 (2014).

50. Lopez-Sanchez, O., Lembke, D., Kayci, M., Radenovic, A. & Kis, A. Ultrasensitive photodetectors based on monolayer MoS2. *Nat. Nanotechnol.* **8,** 497–501 (2013).

51. Chen, M. *et al.* Multibit data storage states formed in plasma-treated MoS2 transistors. *ACS Nano* **8,** 4023–4032 (2014).

52. Perea-López, N. *et al.* CVD-grown monolayered MoS2 as an effective photosensor operating at low-voltage. *2D Mater.* **1,** 1–11 (2014).

53. Zhou, L. *et al.* Large-Area Synthesis of High-Quality Uniform Few-Layer MoTe2. *J. Am. Chem. Soc.* **137,** 11892–11895 (2015).

54. Voiry, D. *et al.* Covalent functionalization of monolayered transition metal dichalcogenides by phase engineering. *Nat. Chem.* **7,** 45–49 (2015).

55. Park, J. C. *et al.* Phase-Engineered Synthesis of Centimeter-Scale 1T′- and 2H-Molybdenum Ditelluride Thin Films. *ACS Nano* **9,** 6548–6554 (2015).

56. Empante, T. A. *et al.* Chemical Vapor Deposition Growth of Few-Layer MoTe2 in the 2H, 1T′, and 1T Phases: Tunable Properties of MoTe2 Films. *ACS Nano* **11,** 900–905 (2017).

57. Han, G. H. *et al.* Absorption dichroism of monolayer 1T′-MoTe 2 in visible range. *2D Mater.* **3,** 1–6 (2016).

58. Yan, B. & Felser, C. Topological Materials: Weyl Semimetals. *Annu. Rev. Condens. Matter Phys.* **8,** 337–354 (2017).

59. Splendiani, A. *et al.* Emerging photoluminescence in monolayer MoS2. *Nano Lett.* **10,** 1271–5 (2010).

60. Zhou, B. *et al.* Evolution of electronic structure in atomically thin sheets of WS2 and WSe2. *ACS Nano* **7,** 791–797 (2013).

61. Kumar, A. & Ahluwalia, P. K. Electronic structure of transition metal dichalcogenides monolayers 1H-MX2 (M = Mo, W; X = S, Se, Te) from ab-initio theory: new direct band gap semiconductors. *Eur. Phys. J. B* **85,** 1–7 (2012).

62. Ruppert, C., Aslan, O. B. & Heinz, T. F. Optical properties and band gap of single- and few-layer MoTe2 crystals. *Nano Lett.* **14,** 6231–6236 (2014).

63. Lezama, I. G. *et al.* Indirect-to-Direct Band Gap Crossover in Few-Layer MoTe2. *Nano Lett.* **15,** 2336–2342 (2015).

64. Yamamoto, M. *et al.* Strong enhancement of Raman scattering from a bulk-inactive vibrational mode in few-layer MoTe2. *ACS Nano* **8,** 3895–3903 (2014).

65. Chang, Y. M. *et al.* Reversible and Precisely Controllable p/n-Type Doping of MoTe2 Transistors through Electrothermal Doping. *Adv. Mater.* **30,** 1–7 (2018).

66. Ma, P. *et al.* Fast MoTe2Waveguide Photodetector with High Sensitivity at Telecommunication Wavelengths. *ACS Photonics* **5,** 1846–1852 (2018).

67. Kim, C. *et al.* Fermi Level Pinning at Electrical Metal Contacts of Monolayer Molybdenum Dichalcogenides. *ACS Nano* **11,** 1588–1596 (2017).

68. Pradhan, N. R. *et al.* Field-Effect Transistors Based on few-layered MoTe2. *ACS Nano* **8,** 5911–5920 (2014).

69. Pezeshki, A., Shokouh, S. H. H., Nazari, T., Oh, K. & Im, S. Electric and Photovoltaic Behavior of a Few-Layer α-MoTe2 /MoS2 Dichalcogenide Heterojunction. *Adv. Mater.* **28,** 3216–3222 (2016).

70. Lin, Y.-F. *et al.* Ambipolar MoTe2 transistors and their applications in logic circuits. *Adv. Mater.* **26,** 3263–9 (2014).

71. Fathipour, S. *et al.* Exfoliated multilayer MoTe2 field-effect transistors. *Appl. Phys. Lett.* **105,** 1–4 (2014).

72. Ji, H. *et al.* Tunable Mobility in Double-Gated MoTe2Field-Effect Transistor: Effect of Coulomb Screening and Trap Sites. *ACS Appl. Mater. Interfaces* **9,** 29185–29192 (2017).

73. Lezama, I. G. *et al.* Surface transport and band gap structure of exfoliated 2H-MoTe 2 crystals. *2D Mater.* **1,** 1–13 (2014).

74. Lin, Y.-F. *et al.* Origin of Noise in Layered MoTe2 Transistors and its Possible Use for Environmental Sensors. *Adv. Mater.* **27,** 6612–6619 (2015).

75. Xu, H., Fathipour, S., Kinder, E. W., Seabaugh, A. C. & Fullerton-Shirey, S. K. Reconfigurable Ion Gating of 2H-MoTe 2 Field-Effect Transistors Using Poly(ethylene oxide)-CsClO 4 Solid Polymer Electrolyte. *ACS Nano* **9,** 4900–4910 (2015).

76. Nakaharai, S. *et al.* Electrostatically Reversible Polarity of Ambipolar a-MoTe2 Transistors. *ACS Nano* **9,** 5976–5983 (2015).

77. Heo, J. *et al.* Reconfigurable van der Waals Heterostructured Devices with Metal-Insulator Transition. *Nano Lett.* **16,** 6746–6754 (2016).

78. Choi, K. *et al.* Non-Lithographic Fabrication of All-2D α-MoTe2Dual Gate Transistors. *Adv. Funct. Mater.* **26,** 3146–3153 (2016).

79. Yin, L. *et al.* Ultrahigh sensitive MoTe2 phototransistors driven by carrier tunneling. *Appl. Phys. Lett.* **108,** 1–6 (2016).

80. Nakaharai, S., Yamamoto, M., Ueno, K. & Tsukagoshi, K. Carrier Polarity Control in α-MoTe2 Schottky Junctions Based on Weak Fermi-Level Pinning. *ACS Appl. Mater. Interfaces* **8,** 14732–14739 (2016).

81. Ji, H. *et al.* Suppression of Interfacial Current Fluctuation in MoTe 2 Transistors with Different Dielectrics. *ACS Appl. Mater. Interfaces* **8,** 19092–19099 (2016).

82. Wang, Z. *et al.* Electrostatically tunable lateral MoTe2p-n junction for use in high-performance optoelectronics. *Nanoscale* **8,** 13245–13250 (2016).

83. Larentis, S. *et al.* Reconfigurable Complementary Monolayer MoTe2Field-Effect Transistors for Integrated Circuits. *ACS Nano* **11,** 4832–4839 (2017).

84. Qi, D. *et al.* Reducing the Schottky barrier between few-layer MoTe 2 and gold. *2D Mater.* **4,** (2017).

85. Qu, D. *et al.* Carrier-Type Modulation and Mobility Improvement of Thin MoTe2. *Adv. Mater.* **29,** 1–11 (2017).

86. Amit, I. *et al.* Role of Charge Traps in the Performance of Atomically Thin Transistors. *Adv. Mater.* **29,** (2017).

87. Chen, J. *et al.* Contact Engineering of Molybdenum Ditelluride Field Effect Transistors through Rapid Thermal Annealing. *ACS Appl. Mater. Interfaces* **9,** 30107–30114 (2017).

88. Sung, J. H. *et al.* Coplanar semiconductor-metal circuitry defined on few-layer MoTe2via polymorphic heteroepitaxy. *Nat. Nanotechnol.* **12,** 1064–1070 (2017).

89. Ji, H. *et al.* Thickness-dependent carrier mobility of ambipolar MoTe2: Interplay between interface trap and Coulomb scattering. *Appl. Phys. Lett.* **110,** 1–6 (2017).

90. Feng, Z. *et al.* Highly sensitive MoTe2 chemical sensor with fast recovery rate through gate biasing. *2D Mater.* **4,** 1–6 (2017).

91. Townsend, N. J., Amit, I., Craciun, M. F. & Russo, S. Sub 20 meV Schottky barriers in metal/MoTe 2 junctions. *2D Mater.* **5,** 1–8 (2018).

92. Shackery, I. Few-Layered α-MoTe2 Schottky Junction for High Sensitive Chemical-Vapour Sensor. *J. Mater. Chem. C* (2018).

93. Luo, W. *et al.* Carrier Modulation of Ambipolar Few-Layer MoTe2Transistors by MgO Surface Charge Transfer Doping. *Adv. Funct. Mater.* **28,** 1–7 (2018).

94. Sze, S. M. & Kwok, K. N. *Physics of Semiconductor Devices (3rd ed.)*. (2007).

95. Late, D. J., Liu, B., Matte, H. S. S. R., Dravid, V. P. & Rao, C. N. R. Hysteresis in Single-Layer MoS 2 Field Effect Transistors. *ACS Nano* **6,** 5635–5641 (2012).

96. Sirota, B., Glavin, N., Krylyuk, S., Davydov, A. V & Voevodin, A. A. Hexagonal MoTe2 with Amorphous BN Passivation Layer for Improved Oxidation Resistance and Endurance of 2D Field Effect Transistors. *Sci. Rep.* **8,** 1–8 (2018).

97. Castellanos-Gomez, A. *et al.* Deterministic transfer of two-dimensional materials by all-dry viscoelastic stamping. *2D Mater.* **1,** 1–8 (2014).

98. Liu, J. *et al.* Pronounced Photovoltaic Response from Multi-layered MoTe2 Phototransistor with Asymmetric Contact Form. *Nanoscale Res. Lett.* **12,** 4–11 (2017).

99. Chen, W., Liang, R., Wang, J., Zhang, S. & Xu, J. Enhanced photoresponsivity and hole mobility of MoTe2 phototransistors by using an Al2O3 high-κ gate dielectric. *Sci. Bull.* **63,** 997–1005 (2018).

100. Zhang, K. *et al.* Interlayer Transition and Infrared Photodetection in Atomically Thin Type-II MoTe2/MoS2van der Waals Heterostructures. *ACS Nano* **10,** 3852–3858 (2016).

101. Huang, H. *et al.* Highly sensitive visible to infrared MoTe 2 photodetectors enhanced by the photogating effect. *Nanotechnology* **27,** 1–7 (2016).

102. Ghatak, S., Pal, A. N. & Ghosh, A. Nature of Electronic States in Atomically Thin MoS2 Field-Effect Transistors. *ACS Nano* **5,** 7707–7712 (2011).

103. Miller, B., Parzinger, E., Vernickel, A., Holleitner, A. W. & Wurstbauer, U. Photogating of mono- and few-layer MoS2. *Appl. Phys. Lett.* **106,** 122103 (2015).

104. Furchi, M. M., Polyushkin, D. K., Pospischil, A. & Mueller, T. Mechanisms of photoconductivity in atomically thin MoS2. *Nano Lett.* **14,** 6165–6170 (2014).

105. Wang, F. *et al.* Strong electrically tunable MoTe2/graphene van der Waals heterostructures for high-performance electronic and optoelectronic devices. *Appl. Phys. Lett.* **109,** 1–5 (2016).

106. Zhang, K. *et al.* Ultrasensitive Near-Infrared Photodetectors Based on a Graphene-MoTe2-Graphene Vertical van der Waals Heterostructure. *ACS Appl. Mater. Interfaces* **9,** 5392–5398 (2017).

107. Wang, F. *et al.* Configuration-Dependent Electrically Tunable Van der Waals Heterostructures Based on MoTe2/MoS2. *Adv. Funct. Mater.* **26,** 5499–5506 (2016).

108. Li, S.-L., Komatsu, K. & Nakaharai, S. Thickness Scaling Effect on Interfacial Barrier and Electrical Contact to Two-Dimensional MoS2 Layers. *ACS Nano* **8,** 12836–12842 (2014).

109. Wang, F., Stepanov, P., Gray, M. & Ning Lau, C. Annealing and transport studies of suspended molybdenum disulfide devices. *Nanotechnology* **26,** 1–5 (2015).

110. Zhu, H. *et al.* Defects and Surface Structural Stability of MoTe 2 Under Vacuum Annealing. *ACS Nano* **11,** 11005–11014 (2017).

111. Meitl, M. A. *et al.* Transfer printing by kinetic control of adhesion to an elastomeric stamp. *Nat. Mater.* **5,** 33–38 (2006).

112. Ferrari, A. C. *et al.* Raman Spectrum of Graphene and Graphene Layers. *Phys. Rev. Lett.* **97,** 1–4 (2006).

113. Spevack, P. A. & McIntyre, N. S. Thermal reduction of molybdenum trioxide. *J. Phys. Chem.* **96,** 9029–9035 (1992).

114. Chen, S. Y., Naylor, C. H., Goldstein, T., Johnson, A. T. C. & Yan, J. Intrinsic Phonon Bands in High-Quality Monolayer T' Molybdenum Ditelluride. *ACS Nano* **11,** 814–820 (2017).

115. Blake, P. *et al.* Making graphene visible. *Appl. Phys. Lett.* **91,** 1–3 (2007).

116. De Sanctis, A., Jones, G. F., Townsend, N. J., Craciun, M. F. & Russo, S. An integrated and multi-purpose microscope for the characterization of atomically thin optoelectronic devices. *Rev. Sci. Instrum.* **88,** 1–11 (2017).

117. Fiori, G. *et al.* Electronics based on two-dimensional materials. *Nat. Nanotechnol.* **9,** 768–779 (2014).

118. Pradhan, N. *et al.* High Photoresponsivity and Short Photo Response Times in Few-Layered WSe2 Transistors. *ACS Appl. Mater. Interfaces* **7,** 12080–12088 (2015).

119. Zhang, Y. *et al.* Photothermoelectric and photovoltaic effects both present in MoS2. *Sci. Rep.* **5,** 1–7 (2015).

120. Buscema, M. *et al.* Large and Tunable Photothermoelectric E ff ect in Single-Layer MoS 2. *Nano Lett.* **13,** 1–18 (2013).

121. Fang, H. & Hu, W. Photogating in Low Dimensional Photodetectors. *Advanced Science* **4,** 1–17 (2017).

122. Echtermeyer, T. J. *et al.* Photothermoelectric and photoelectric contributions to light detection in metal-graphene-metal photodetectors. *Nano Lett.* **14,** 3733–3742 (2014).

123. Groenendijk, D. J. *et al.* Photovoltaic and Photothermoelectric Effect in a Double-Gated WSe 2 Device. *Nano Lett.* **14,** 5846–5852 (2014).

124. Fontana, M. *et al.* Electron-hole transport and photovoltaic effect in gated MoS2 Schottky junctions. *Sci. Rep.* **3,** 1–5 (2013).

125. Patil, V., Capone, A., Strauf, S. & Yang, E.-H. Improved photoresponse with enhanced photoelectric contribution in fully suspended graphene photodetectors. *Sci. Rep.* **3,** 1–5 (2013).

126. Buscema, M. *et al.* Photocurrent generation with two-dimensional van der Waals semiconductors. *Chem Soc Rev* **44,** 3691–3718 (2015).

127. Wu, C. C. *et al.* Elucidating the photoresponse of ultrathin MoS2 field-effect transistors by scanning photocurrent microscopy. *J. Phys. Chem. Lett.* **4,** 2508–2513 (2013).

128. Howell, S. L. *et al.* Investigation of Band-Offsets at Monolayer–Multilayer MoS2 Junctions by Scanning Photocurrent Microscopy. *Nano Lett.* **15,** 2278–2284 (2015).

129. Yin, Z. *et al.* Single-layer MoS2 phototransistors. *ACS Nano* **6,** 74–80 (2012).

130. Zhang, W. *et al.* High-gain phototransistors based on a CVD MoS_2 monolayer. *Adv. Mater.* **25,** 3456–61 (2013).

131. Chang, Y. *et al.* Monolayer MoSe2 Grown by Chemical Vapor Deposition for Fast Photodetection. *ACS Nano* **8,** 8582–8590 (2014).

132. Su, G. *et al.* Chemical vapor deposition of thin crystals of layered semiconductor sns2 for fast photodetection application. *Nano Lett.* **15,** 506–513 (2015).

133. Tsai, D. S. *et al.* Few-layer MoS2 with high broadband photogain and fast optical switching for use in harsh environments. *ACS Nano* **7,** 3905–3911 (2013).

134. Choi, W. *et al.* High-detectivity multilayer MoS2 phototransistors with spectral response from ultraviolet to infrared. *Adv. Mater.* **24,** 5832–6 (2012).

135. Abderrahmane, A. *et al.* High photosensitivity few-layered MoSe2 back-gated field-effect phototransistors. *Nanotechnology* **25,** 1–5 (2014).

136. Kuiri, M. *et al.* Enhancing photoresponsivity using MoTe2-graphene vertical heterostructures. *Appl. Phys. Lett.* **108,** 1–5 (2016).

137. Zhang, E. *et al.* ReS2 -Based Field-Effect Transistors and Photodetectors. *Adv. Funct. Mater.* **25,** 4076–4082 (2015).

138. Perea-Lopez, N. *et al.* Photosensor device based on few-layered WS2 films. *Adv. Funct. Mater.* **23,** 5511–5517 (2013).

139. Huo, N. *et al.* Photoresponsive and Gas Sensing Field-Effect Transistors based on Multilayer WS2 Nanoflakes. *Sci. Rep.* **4,** 1–9 (2014).

140. Zhang, W. *et al.* Role of Metal Contacts in High-Performance Phototransistors Based on WSe2 Monolayers. *ACS Nano* **8,** 8653–8661 (2014).

141. Kufer, D. & Konstantatos, G. Highly Sensitive, Encapsulated MoS2 Photodetector with Gate Controllable Gain and Speed. *Nano Lett.* **15,** 7307–7313 (2015).

142. Mattmann, M. *et al.* Pulsed gate sweep strategies for hysteresis reduction in carbon nanotube transistors for low concentration NO2 gas detection. *Nanotechnology* **21,** 1–9 (2010).

143. Chaves, F. A. & Jim, D. The role of the Fermi level pinning in gate tunable graphene-semiconductor junctions. *IEEE Trans. Electron Devices* **63,** 4521–4526 (2016).

144. Lee, H. S. *et al.* MoS2 nanosheets for top-gate nonvolatile memory transistor channel. *Small* **8,** 3111–3115 (2012).

145. Khan, M. F. *et al.* Stable and reversible doping of graphene by using KNO3 solution and photo-desorption current response. *RSC Adv.* **5,** 50040–50046 (2015).

146. Zhou, P., Chen, C., Wang, X., Hu, B. & San, H. 2-Dimentional photoconductive MoS2 nanosheets using in surface acoustic wave resonators for ultraviolet light sensing. *Sensors Actuators, A Phys.* **271,** 389–397 (2018).

147. Lei, S. *et al.* Optoelectronic Memory Using Two-Dimensional Materials. *Nano Lett.* **15,** 259–265 (2015).

148. Choi, M. S. *et al.* Controlled charge trapping by molybdenum disulphide and graphene in ultrathin heterostructured memory devices. *Nat. Commun.* **4,** 1–7 (2013).

149. Wu, E. *et al.* Ultra-sensitive and Fully Reversible NO2 Gas Sensing based on p-type MoTe2 Under ultra-violet Illumination. *ACS Sensors* (2018).

150. Serpi, A. Negative Photoconductivity in MoS2. *Phys. Status Solidi* **133,** 73–77 (1992).

151. Khan, M. F., Nazir, G., Lermolenko, V. M. & Eom, J. Electrical and photo-electrical properties of MoS2 nanosheets with and without an Al2O3 capping layer under various environmental conditions. *Sci. Technol. Adv. Mater.* **17,** 166–176 (2016).

152. Brongersma, M. L., Halas, N. J. & Nordlander, P. Plasmon-induced hot carrier science and technology. *Nat. Nanotechnol.* **10,** 25–34 (2015).

153. Fu, X. Q., Wang, C., Feng, P. & Wang, T. H. Anomalous photoconductivity of CeO2 nanowires in air. *Appl. Phys. Lett.* **91,** 1–3 (2007).

154. Peng, L. *et al.* Anomalous photoconductivity of cobalt-doped zinc oxide nanobelts in air. *Chem. Phys. Lett.* **456,** 231–235 (2008).

155. Nowak, M. *et al.* Transient characteristics and negative photoconductivity of SbSI humidity sensor. *Sensors Actuators, A Phys.* **210,** 32–40 (2014).

156. Zhang, X. *et al.* Surface induced negative photoconductivity in p-type ZnSe:Bi nanowires and their nano-optoelectronic applications. *J. Mater. Chem.* **21,** 6736–6741 (2011).

157. Chen, R. J. *et al.* Molecular photodesorption from single-walled carbon nanotubes. *Appl. Phys. Lett.* **79,** 2258–2260 (2001).

158. Rusu, C. N. & Yates, J. T. J. Defect Sites on TiO2(110). Detection by O2 Photodesorption. *Langmuir* **13,** 4311–4316 (1997).

159. Chen, B. Environmental Changes in MoTe2 Excitonic Dynamics by Defects-

Activated Molecular Interaction. *ACS Nano* **9,** 5326–5332 (2015).

160. Cho, K. *et al.* Electric stress-induced threshold voltage instability of multilayer MoS2 field effect transistors. *ACS Nano* **7,** 7751–7758 (2013).

161. Zhan, Y., Liu, Z., Najmaei, S., Ajayan, P. M. & Lou, J. Large-area vapor-phase growth and characterization of MoS2 atomic layers on a SiO2 substrate. *Small* **8,** 966–71 (2012).

162. Butun, S., Tongay, S. & Aydin, K. Enhanced Light Emission from Large-Area Monolayer MoS2 Using Plasmonic Nanodisc Arrays. *Nano Lett.* **15,** 2700–2704 (2015).

163. Hu, L., Shan, X., Wu, Y., Zhao, J. & Lu, X. Laser thinning and patterning of MoS2with layer-by-layer precision. *Sci. Rep.* **7,** 1–9 (2017).

164. Lu, J. *et al.* Improved photoelectrical properties of MoS2 films after laser micromachining. *ACS Nano* **8,** 6334–6343 (2014).

165. Barkelid, M., Goossens, A. M., Calado, V. E., Zant, H. S. J. Van Der & Steele, G. A. Laser-Thinning of MoS 2 : On Demand Generation of a Single-Layer Semiconductor. 1–6 (2012). doi:10.1021/nl301164v

166. Amara, K. K., Chu, L., Kumar, R., Toh, M. & Eda, G. Wet chemical thinning of molybdenum disulfide down to its monolayer. *APL Mater.* **2,** (2014).

167. Lu, X., Utama, M. I. B., Zhang, J., Zhao, Y. & Xiong, Q. Layer-by-layer thinning of MoS_2 by thermal annealing. *Nanoscale* **5,** 8904–8 (2013).

168. Liu, Y. *et al.* Layer-by-Layer Thinning of MoS2 by Plasma. *ACS Nano* **7,** 4202–4209 (2013).

169. Bobrinetskiy, I., Emelianov, A. & Nasibulin, A. Photophysical and photochemical effects in ultrafast laser patterning of CVD graphene. *J. Phys. D. Appl. Phys.* **49,** (2016).

170. Oh, H. M. *et al.* Photochemical Reaction in Monolayer MoS 2 via Correlated Photoluminescence, Raman Spectroscopy, and Atomic Force Microscopy. *ACS Nano* **10,** 5230–5236 (2016).

171. Ashby, C. I. H. & Ashby, C. H. Doping level selective photochemical dry etching of GaAs selective photochemical dry etching of GaAs. **752,** 1–4 (1989).

172. Wang, K. *et al.* nonlinear refraction of layered molybdenum dichalcogenide semiconductors †. *Nanoscale* **6,** 10530–10535 (2014).

173. Sanctis, A. De, Amit, I., Hepplestone, S. P. & Craciun, M. F. Strain-engineered inverse charge-funnelling in layered semiconductors. *Nat. Commun.* **9,** (2018).

174. Mirabelli, G. *et al.* Air sensitivity of MoS2, MoSe2, MoTe2, HfS2, and HfSe2. *J. Appl. Phys.* **120,** (2016).

175. Yan, R. *et al.* Thermal conductivity of monolayer molybdenum disulfide obtained from temperature-dependent Raman spectroscopy. *ACS Nano* **8,** 986–993 (2014).

176. Park, J., Kim, Y., Jhon, Y. I. & Jhon, Y. M. Temperature dependent Raman spectroscopic study of mono-, bi-, and tri-layer molybdenum ditelluride. *Appl. Phys. Lett.* **107,** (2015).

177. Wei, X. *et al.* Mo-O bond doping and related-defect assisted enhancement of photoluminescence in monolayer MoS2. *AIP Adv.* **4,** (2014).

178. Bie, Y. *et al.* A MoTe2-based light-emitting diode and photodetector for silicon photonic integrated circuits. *Nat. Nanotechnol.* **12,** 1124–1129 (2017).

179. Nan, M. & Jena, D. Interband tunneling in two-dimensional crystal semiconductors. *Appl. Phys. Lett.* **102,** 1–5 (2013).